

KfK 5360  
Oktober 1994

# **An Analysis of Electron Beam Welds in a Dual Coolant Liquid Metal Breeder Blanket**

L. Cizelj, H. Riesch-Oppermann  
Institut für Materialforschung  
Projekt Kernfusion

**Kernforschungszentrum Karlsruhe**



**Kernforschungszentrum Karlsruhe**  
Institut für Materialforschung  
Projekt Kernfusion

**KfK 5360**

**An Analysis of Electron Beam Welds in a Dual Coolant Liquid  
Metal Breeder Blanket**

L.Cizelj\*, H.Riesch-Oppermann

\*"Jožef Stefan" Institute, Reactor Engineering Division  
Ljubljana, Slovenia

Kernforschungszentrum Karlsruhe GmbH, Karlsruhe

Als Manuskript gedruckt  
Für diesen Bericht behalten wir uns alle Rechte vor

Kernforschungszentrum Karlsruhe GmbH  
Postfach 3640, 76021 Karlsruhe

ISSN 0303-4003

## **ABSTRACT**

Numerical simulation of electron beam welding of blanket segments was performed using non-linear finite element code ABAQUS. The thermal and stress fields were assumed uncoupled, while preserving the temperature dependency of all material parameters. The martensite-austenite and austenite-martensite transformations were taken into account through volume shrinking/expansion effects, which is consistent with available data. The distributions of post welding residual stresses in a complex geometry of the first wall are obtained. Also, the effects of preheating and post-welding heat treatment were addressed.

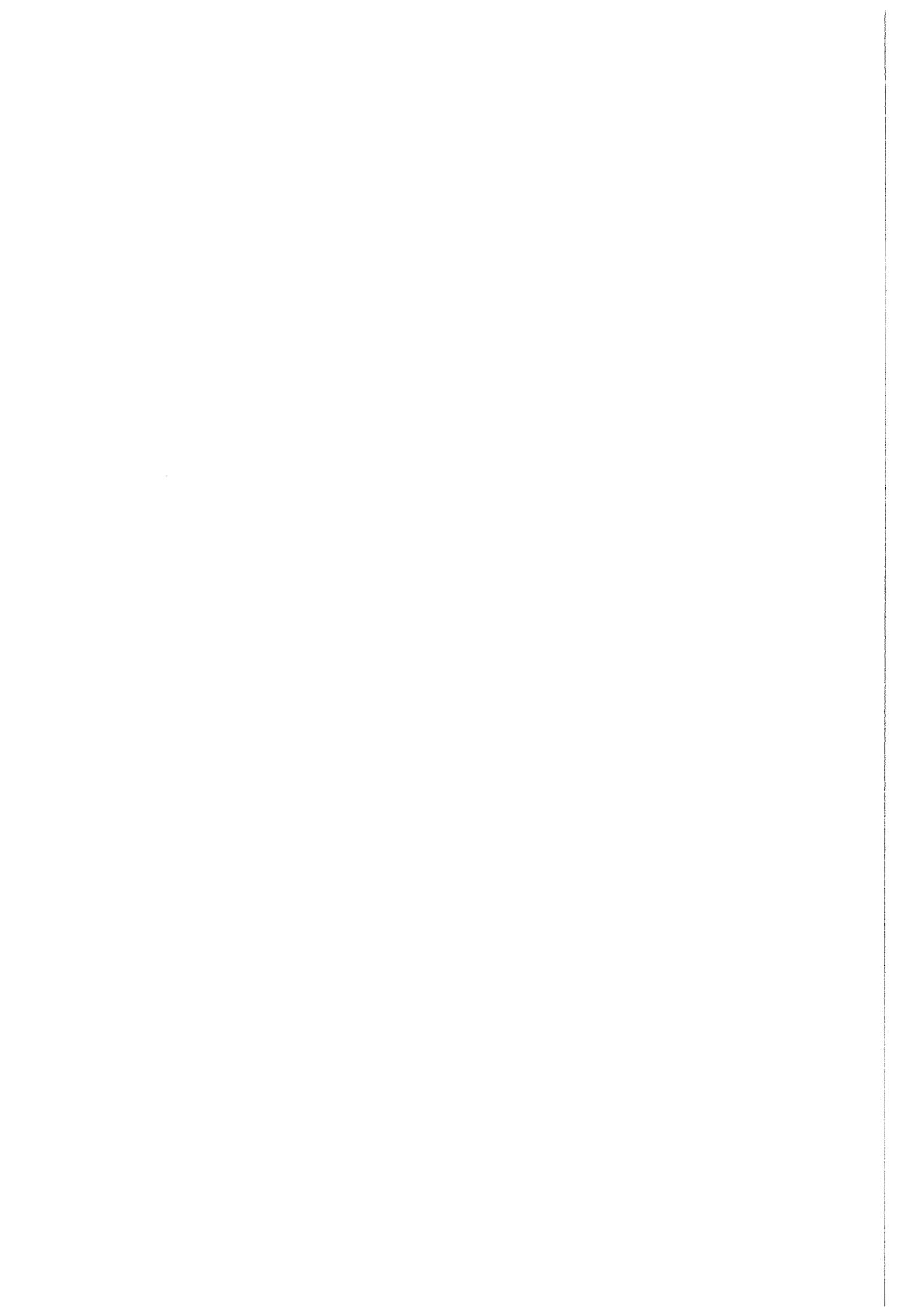
Time dependent temperature and stress-strain fields obtained provide good insight into the welding process. They may be used directly to support reliability and life-time studies of blanket structures. On the other hand, they provide useful hints about the feasibility of the geometrical configurations as proposed by different design concepts.

## **ANALYSE VON ELEKTRONENSTRAHLSCHWEISSNÄHTEN EINES FLÜSSIGMETALLBLANKETS MIT DUAL-COOLANT KONZEPT**

### **ZUSAMMENFASSUNG**

Der vorliegende Report stellt die Ergebnisse nichtlinearer Finite-Elemente-Rechnungen zur numerischen Simulation von Elektronenstrahlschweißungen vor. Mit Hilfe des FE-Programms ABAQUS wurde eine ausgewählte EB-Naht eines Blanketsegments modelliert. Temperatur- und Spannungsfelder wurden als entkoppelt betrachtet; die Temperaturabhängigkeit der verwendeten Materialparameter wurde berücksichtigt. Die Martensit-Austenit und Austenit-Martensit-Umwandlungen wurden im Übereinstimmung mit vorhandenen Daten als Volumenab- bzw. -zunahme berücksichtigt. Man erhält schließlich Schweißzugspannungen in der betrachteten komplexen Schweißnaht. Zusätzlich wurden Einflüsse einer Vorwärmung des Materials sowie einer Nachwärmebehandlung der Schweißnaht untersucht.

Die erhaltenen zeitabhängigen Temperatur- und Spannungsfelder vermitteln einen guten Einblick in den Verlauf des Schweißprozesses. Die Ergebnisse können einerseits bei Zuverlässigkeits- und Lebensdaueruntersuchungen für Blanketstrukturen Anwendung finden. Andererseits ergeben sich wertvolle Hinweise zur Machbarkeit verschiedener Designvorschläge in Hinblick auf geometrische Randbedingungen.



## **ACKNOWLEDGEMENTS**

The research presented in this report was performed during the time between 01.11.1993 and 30.04.1994 when L.Cizelj was active as guest scientist with the Institut für Materialforschung II. The research was supported by Projekt Kernfusion.

Valuable discussions and comments by Mr.E.Diegele are gratefully acknowledged.

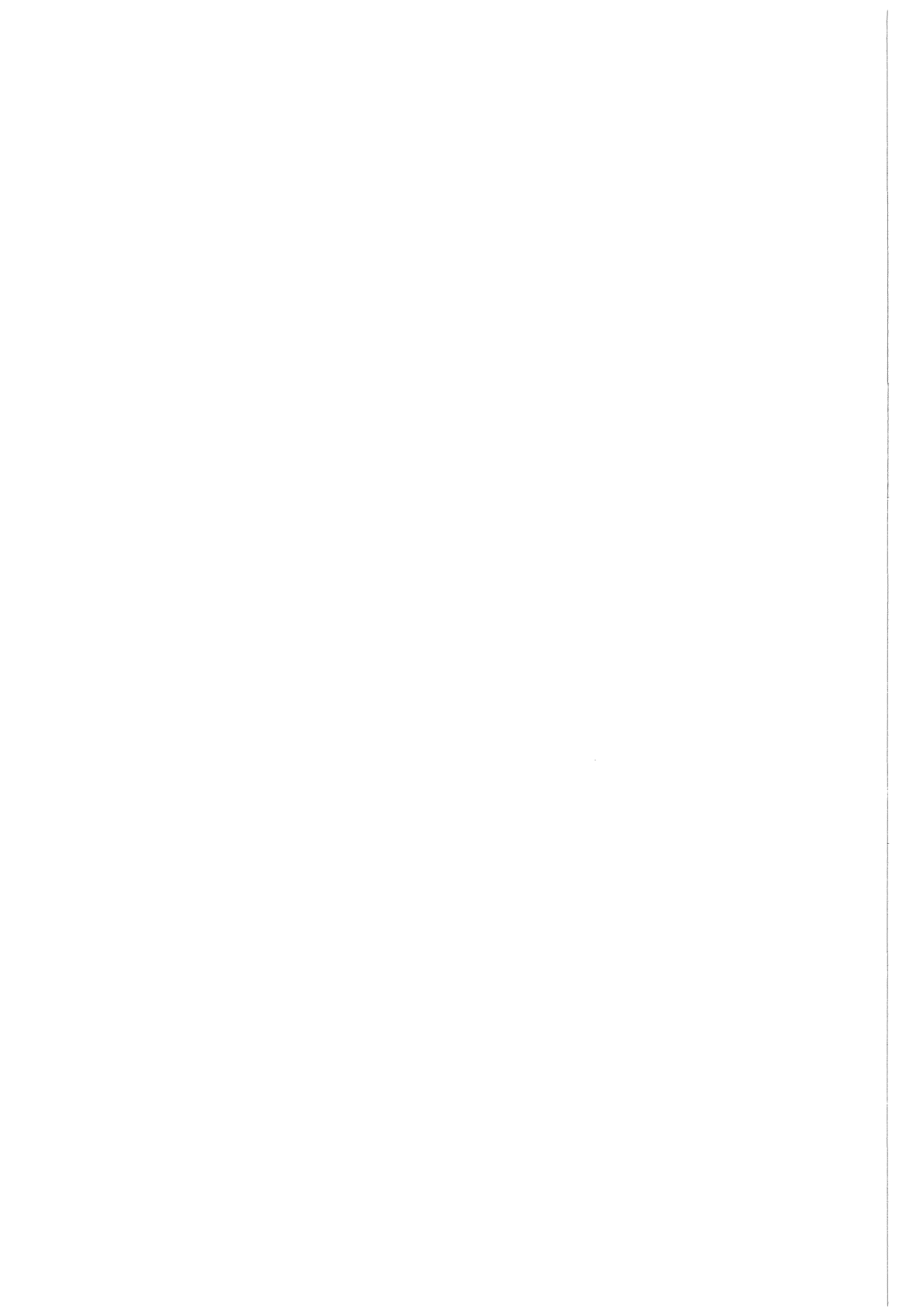


# TABLE OF CONTENTS

LIST OF FIGURES . . . . .	vii
LIST OF TABLES . . . . .	ix
1 INTRODUCTION . . . . .	1
1.1 Dual coolant liquid metal breeder blanket . . . . .	1
1.2 Electron beam welding . . . . .	1
1.2.1 Basic facts . . . . .	1
1.2.2 Known deficiencies . . . . .	4
1.3 Scope of the analysis . . . . .	4
1.4 Organization of this report . . . . .	4
2 SURVEY OF COMPUTATIONAL WELD MECHANICS . . . . .	7
2.1 Development of welding stresses . . . . .	7
2.1.1 Heating . . . . .	8
2.1.2 Cooling . . . . .	8
2.1.3 Residual stresses . . . . .	8
2.2 Heat transfer analysis . . . . .	9
2.2.1 Closed form solutions . . . . .	9
2.2.2 Numerical solutions . . . . .	11
2.3 Microstructural considerations . . . . .	13
2.3.1 Solid state phase transformations . . . . .	13
2.3.2 Transformation plasticity . . . . .	14
2.3.3 Hot cracking . . . . .	14
2.4 Thermal stress analysis . . . . .	15
2.4.1 Constitutive models . . . . .	15
2.4.2 Simplifications of geometry . . . . .	16
2.5 Application to electron beam welding . . . . .	16
3 DOUBLE WELD BETWEEN BLANKET SEGMENTS . . . . .	17
3.1 Summary of basic assumptions and limitations . . . . .	17
3.2 Geometry . . . . .	17
3.2.1 Finite element mesh . . . . .	17
3.2.2 Loading . . . . .	18
3.3 Material model . . . . .	19
3.3.1 Thermal analysis . . . . .	20
3.3.2 Stress analysis . . . . .	20
3.4 Results of thermal analysis . . . . .	22
3.5 Results of stress analysis . . . . .	28
3.5.1 Effects of preheating . . . . .	28
3.6 Residual stresses . . . . .	35
3.6.1 Effect of phase transformations . . . . .	36
3.7 Heat treatment after welding . . . . .	42
3.8 Austenitic stainless steel . . . . .	42
3.9 Summary and possible applications of results . . . . .	43
3.9.1 Thermal analysis . . . . .	43
3.9.2 Stress analysis . . . . .	43
3.9.3 Computational efforts . . . . .	43

4	CONCLUSIONS	44
5	REFERENCES	45
A	MATERIAL PROPERTIES	A-3
A.1	General remarks	A-3
A.1.1	Dependence on temperature	A-3
A.1.2	Dependence on microstructure	A-3
A.2	Summary of basic constitutive assumptions	A-3
A.2.1	Welding	A-3
A.2.2	Heat treatment (annealing)	A-4
A.3	Mechanical properties	A-4
A.3.1	Chemical composition	A-4
A.3.2	Youngs modulus	A-4
A.3.3	Poisson ratio	A-6
A.3.4	Yield strength	A-6
A.3.5	Strain hardening coefficient	A-7
A.4	Physical properties	A-8
A.4.1	Density	A-8
A.4.2	Phase transformations	A-8
A.4.3	Thermal conductivity	A-9
A.4.4	Specific heat	A-9
A.4.5	Thermal expansion	A-10
A.5	Creep properties	A-12
B	TEST WELDS IN PLATES	B-3
B.1	Test procedure	B-3
B.2	Modelling	B-5
B.2.1	Basic assumptions	B-5
B.2.2	Finite element meshes	B-5
B.2.3	Thermal loading	B-5
B.2.4	Material model	B-7
B.3	Results of thermal analysis	B-7
B.3.1	Comparison with measured temperatures	B-7
B.4	Results of stress analysis	B-9
B.4.1	Residual stresses	B-12
B.4.2	Effects of heat treatment	B-19

## LIST OF FIGURES

Fig. 1-1	Cross-section of a blanket segment . . . . .	2
Fig. 1-2	Layout of a blanket segment and detail of a double weld in the first wall .	2
Fig. 1-3	Keyhole weld geometry (after [31]) . . . . .	3
Fig. 2-1	Coupling between thermal, mechanical and microstructural effects (after [13]) . . . . .	7
Fig. 2-2	Typical distributions of longitudinal residual stress at the surface of a butt-welded plate . . . . .	9
Fig. 2-3	A plate to be welded . . . . .	12
Fig. 3-1	Layout of the finite element mesh . . . . .	18
Fig. 3-2	Thermal strain as a function of temperature . . . . .	19
Fig. 3-3	Temperature dependence of conductivity and specific heat . . . . .	20
Fig. 3-4	Temperature dependence of Young modulus and Poisson ratio . . . . .	21
Fig. 3-5	Temperature dependence of yield strength and hardening modulus . . . . .	21
Fig. 3-6	Time history of temperatures in the vicinity of weld . . . . .	22
Fig. 3-7	Distribution of temperatures at 0.04 sec (plasma side weld) . . . . .	24
Fig. 3-8	Distribution of temperatures at 0.04 sec (liquid metal side weld) . . . . .	24
Fig. 3-9	Distribution of temperatures at 0.25 sec (plasma side weld) . . . . .	25
Fig. 3-10	Distribution of temperatures at 0.25 sec (liquid metal side weld) . . . . .	25
Fig. 3-11	Distribution of temperatures at 0.267 sec (plasma side weld) . . . . .	26
Fig. 3-12	Distribution of temperatures at 0.267 sec (liquid metal side weld) . . . . .	26
Fig. 3-13	Distribution of temperatures at 1.75 sec . . . . .	27
Fig. 3-14	Distribution of temperatures at 3.04 sec . . . . .	27
Fig. 3-15	Distribution of temperatures at 11.2 sec . . . . .	28
Fig. 3-16	Equivalent (von Mises) stresses during heating (plasma side weld) . . . . .	29
Fig. 3-17	Equivalent (von Mises) stresses during heating (liquid metal side weld) . .	29
Fig. 3-18	Longitudinal stresses during heating (plasma side weld) . . . . .	30
Fig. 3-19	Longitudinal stresses during heating (liquid metal side weld) . . . . .	30
Fig. 3-20	Stresses in y direction during heating (plasma side weld) . . . . .	31
Fig. 3-21	Stresses in y direction during heating (liquid metal side weld) . . . . .	31
Fig. 3-22	Equivalent stresses (von Mises) during cooling (liquid metal side weld) . .	32
Fig. 3-23	Longitudinal stresses during cooling (plasma side weld) . . . . .	32
Fig. 3-24	Longitudinal stresses during cooling (liquid metal side weld) . . . . .	33
Fig. 3-25	Stresses in y direction during cooling (plasma side weld) . . . . .	33
Fig. 3-26	Stresses in y direction during cooling (liquid metal side weld) . . . . .	34
Fig. 3-27	Transverse strains in plasma side weld without preheating . . . . .	34
Fig. 3-28	Transverse strains in plasma side weld with preheating (100°C) . . . . .	35
Fig. 3-29	Longitudinal (z) residual stress (plasma side weld) . . . . .	37
Fig. 3-30	Longitudinal (z) residual stress (liquid metal side weld) . . . . .	37
Fig. 3-31	Transverse (x) residual stress (plasma side weld) . . . . .	38
Fig. 3-32	Transverse (x) residual stress (liquid metal side weld) . . . . .	38
Fig. 3-33	Residual stress in y direction (plasma side weld) . . . . .	39
Fig. 3-34	Residual stress in y direction (liquid metal side weld) . . . . .	39
Fig. 3-35	Equivalent (von Mises) residual stress (plasma side weld) . . . . .	40
Fig. 3-36	Equivalent (von Mises) residual stress (liquid metal side weld) . . . . .	40
Fig. 3-37	Transverse (x) residual stress without phase transformation (plasma side weld) . . . . .	41

<b>Fig. 3-38</b>	Transverse ( $x$ ) residual stress without phase transformation (liquid metal side weld) . . . . .	41
<b>Fig. 3-39</b>	Relaxation of residual stresses by heat treatment . . . . .	42

**Appendix B**

<b>Fig. B-1</b>	Layout of test welds . . . . .	B-3
<b>Fig. B-2</b>	Temperatures during welding and heat treatment as recorded by the thermocouple . . . . .	B-4
<b>Fig. B-3</b>	Coarse finite element model of the test weld in a plate . . . . .	B-5
<b>Fig. B-4</b>	Fine finite element model of the test weld in a plate . . . . .	B-6
<b>Fig. B-5</b>	Time history of temperatures in the vicinity of weld (martensitic, coarse mesh) . . . . .	B-8
<b>Fig. B-6</b>	Time history of temperatures in the vicinity of weld (martensitic, fine mesh) . . . . .	B-8
<b>Fig. B-7</b>	Time history of temperatures in the vicinity of weld (austenitic, coarse mesh) . . . . .	B-9
<b>Fig. B-8</b>	Development of equivalent (von Mises) stress (martensitic material, middle plane) . . . . .	B-10
<b>Fig. B-9</b>	Development of equivalent (von Mises) stress (martensitic material, surface) . . . . .	B-10
<b>Fig. B-10</b>	Development of equivalent (von Mises) stress (austenitic material, middle plane) . . . . .	B-11
<b>Fig. B-11</b>	Development of equivalent (von Mises) stress (austenitic material, surface) . . . . .	B-11
<b>Fig. B-12</b>	Transverse residual stresses ( $\sigma_{xx}$ ) in austenitic plate (middle plane) . . . . .	B-13
<b>Fig. B-13</b>	Transverse residual stresses ( $\sigma_{xx}$ ) in austenitic plate (surface) . . . . .	B-13
<b>Fig. B-14</b>	Longitudinal residual stresses ( $\sigma_{zz}$ ) in austenitic plate (middle plane) . . . . .	B-14
<b>Fig. B-15</b>	Longitudinal residual stresses ( $\sigma_{zz}$ ) in austenitic plate (surface) . . . . .	B-14
<b>Fig. B-16</b>	Transverse residual stresses ( $\sigma_{xx}$ ) in martensitic plate (middle plane, without phase transformations) . . . . .	B-15
<b>Fig. B-17</b>	Transverse residual stresses ( $\sigma_{xx}$ ) in martensitic plate (surface, without phase transformations) . . . . .	B-15
<b>Fig. B-18</b>	Longitudinal residual stresses ( $\sigma_{zz}$ ) in martensitic plate (middle plane, without phase transformations) . . . . .	B-16
<b>Fig. B-19</b>	Longitudinal residual stresses ( $\sigma_{zz}$ ) in martensitic plate (surface, without phase transformations) . . . . .	B-16
<b>Fig. B-20</b>	Transverse residual stresses ( $\sigma_{xx}$ ) in martensitic plate (middle plane, with phase transformations) . . . . .	B-17
<b>Fig. B-21</b>	Transverse residual stresses ( $\sigma_{xx}$ ) in martensitic plate (surface, with phase transformations) . . . . .	B-17
<b>Fig. B-22</b>	Longitudinal residual stresses ( $\sigma_{zz}$ ) in martensitic plate (middle plane, with phase transformations) . . . . .	B-18
<b>Fig. B-23</b>	Longitudinal residual stresses ( $\sigma_{zz}$ ) in martensitic plate (surface, with phase transformations) . . . . .	B-18

## LIST OF TABLES

<b>Table A.I</b>	Chemical composition of steels analyzed . . . . .	A-5
<b>Table A.II</b>	Equivalent Ni and Cr contents of steels analyzed . . . . .	A-5
<b>Table A.III</b>	Youngs modulus and Poisson ratio . . . . .	A-6
<b>Table A.IV</b>	Yield strength and hardening coefficient . . . . .	A-7
<b>Table A.V</b>	Ultimate tensile strength and strain . . . . .	A-8
<b>Table A.VI</b>	Thermal conductivity and specific heat . . . . .	A-10
<b>Table A.VII</b>	Thermal expansion coefficient and thermal strain . . . . .	A-11
<b>Table A.VIII</b>	Creep properties . . . . .	A-13

# 1 INTRODUCTION

The plasma in the future fusion reactors will be surrounded by a toroidal structure named blanket. The main functions of the blanket will be to provide facilities for heat extraction, shielding for neutrons produced in the fusion reaction and production of tritium which is needed in the fusion reaction. The heat extraction and tritium production can be provided by a suitable choice of a liquid metal coolant.

One of the major problems arising with the use of liquid metal coolants are relative large velocities needed for efficient cooling of first blanket wall. This may cause unacceptably high pressure drops due to the interaction with a strong magnetic field. Some designs therefore propose to cool the first wall by helium or water, which reduces the velocities of the liquid metal coolant and the problem of magneto-hydrodynamic pressure drops. A review of concepts and related analyses of the DEMO-relevant test blankets for NET/ITER is given in [17] and [22].

Adequate structural reliability of blanket structure is required to minimize the possibility of contact between the plasma and coolants. One of the requirements which were defined to achieve high reliability of the blanket structure was that at least two welds should be placed between the liquid metal and plasma. One of the recently proposed blanket designs satisfying this requirement is dual coolant liquid metal breeder blanket [23].

## 1.1 Dual coolant liquid metal breeder blanket

A cross-section of a blanket segment is shown in Fig. 1-1. The first wall of the U-shaped box is cooled with helium which flows through channels in the toroidal direction. Inside the box, a grid of steel plates forms poloidal ducts for the liquid metal breeder.

The blanket is composed of a series of curved segments. One of them is shown in Fig. 1-2. The segments are assembled from boxes of approx. 1 m in height. The boxes are welded together utilizing the electron beam welding technique, which enables the one-pass welding of the double weld as shown in Fig. 1-2.

The double weld in the first wall is foreseen for the safety reasons. It reduces the possibility of contact between plasma and liquid metal, which is of great importance for the reliability and availability of the reactor. The channel between the welds can be used for leak detection monitoring.

Detailed description of the dual coolant liquid metal breeder blanket and its operational and safety features is given in [23].

## 1.2 Electron beam welding

### 1.2.1 Basic facts

The energy to melt the workpiece is derived from a high velocity stream of electrons, usually in vacuum conditions. The characteristic power densities are in the range of  $10^{10}$ - $10^{13}$  W/m<sup>2</sup>. At such power densities, the conduction in the welded structure and the vaporization are both present to a considerable extent. Increasing power density over  $10^{13}$  W/m<sup>2</sup> causes the vaporization front propagation to be faster than the heat conduction in the material, allowing

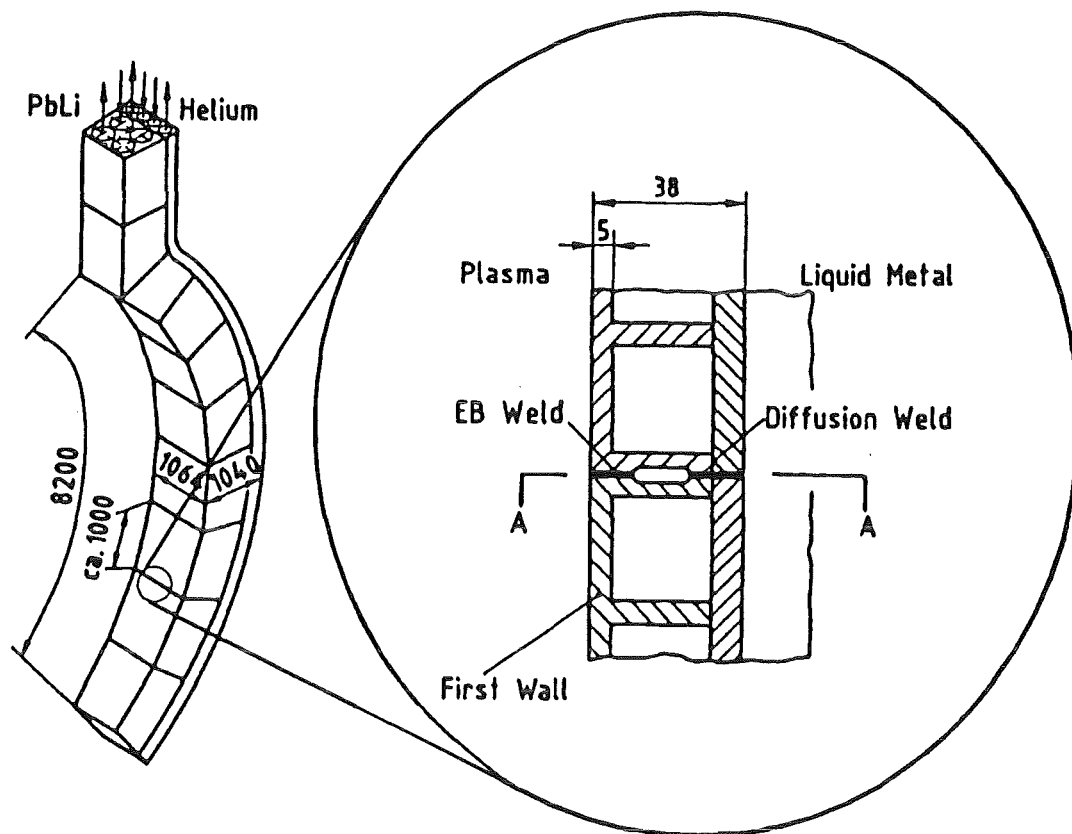


Fig. 1-1 Cross-section of a blanket segment

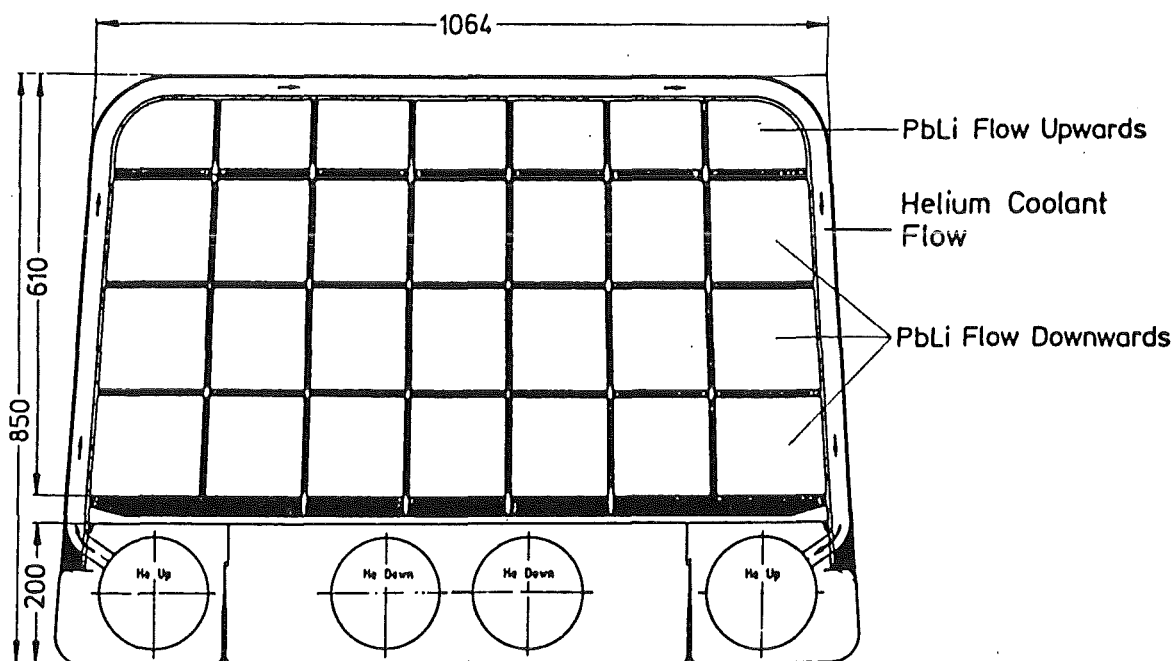


Fig. 1-2 Layout of a blanket segment and detail of a double weld in the first wall

for example for producing a hole without depositing significant amount of heat in the workpiece. Lower power densities however mean that conduction starts to dominate the

process like in conventional arc welding processes ( $10^6$ - $10^8$  W/m<sup>2</sup>). At power densities below  $10^6$  W/m<sup>2</sup> no melting is possible [31].

Large power densities employed cause the vaporization of the molten material. Vaporized part of the metal (*keyhole*, see Fig. 1-3) may extend through the entire thickness of the workpiece. A typical keyhole diameter is in the order of 0.5 mm [31].

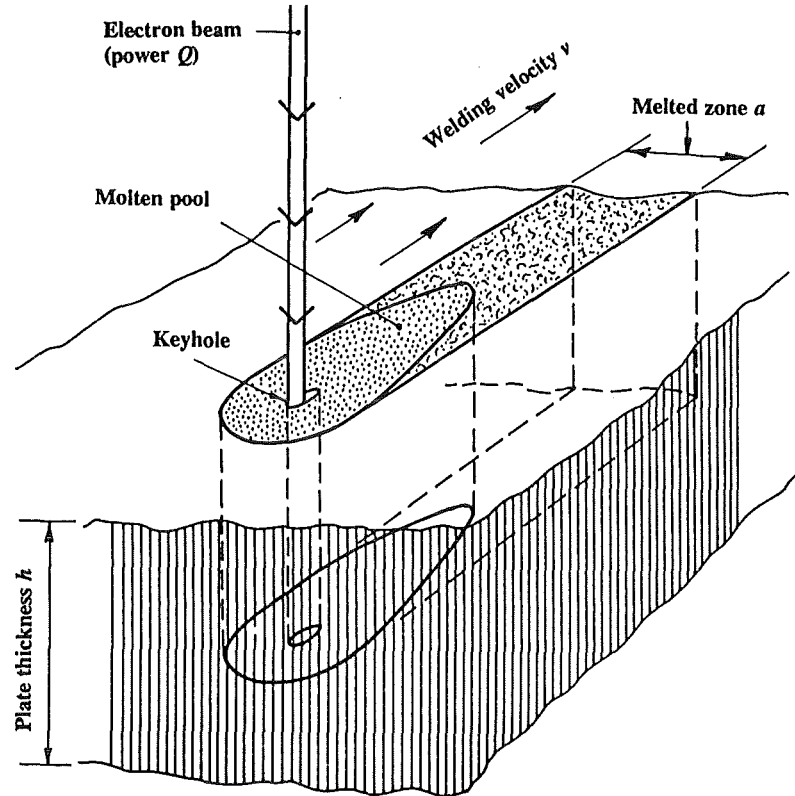


Fig. 1-3 Keyhole weld geometry (after [31])

Some general features of the electron beam welding are:

- The weld depth is generally at least one order of magnitude larger than its width. Tomita [40] reports successful one-pass welding of 100 mm thick steel plates with target welding bead of 4 mm.
- Significantly lower thermal distortion is produced than by conventional arc techniques. For example, distortion produced by up to 50 E-beam welds side by side on a plate is less than that obtained by one submerged arc weld on the plate of similar properties [31].
- Comparably high welding speeds can be used in addition to one-pass welding.

A theoretical limit for the amount of power used for the metal melting exists [38]. With large input powers, a maximum of 48% of the incident beam power can be used to melt the material. The rest is being conducted thermally into material. This efficiency decreases rapidly with decreasing input power.

For more detailed description of the process, see Quigley [31] and references therein.

### 1.2.2 Known deficiencies

Generally, electron beam welding has certain deficiencies, which have to be accounted for while designing the structure:

- Efficient welding is for the time being only possible in vacuum.
- It was found to cause solidification and intergranular segregation irrespective of the steel grades [40]. Beside metallurgical reasons (see Section 2.3.3), strains caused by high energy welding processes are known to enhance those processes [18].

Experimental analysis of residual stresses in electron beam welded plates [30] showed presence of considerable residual stresses. The reported values are compared to those obtained by classical arc welding showing rather high residual stresses caused by electron beam welding, although they are consistently smaller than those obtained by arc welding.

### 1.3 Scope of the analysis

The main motivation for this analysis is the fact that welds actually govern the fatigue life time of the structure. The reasons for faster fatigue in the welds are twofold. First, significant residual stresses may be induced during the welding. Second, the metallurgical processes which take place during the weld solidification and cooling may both reduce the material toughness (changes in microstructure) and increase the fatigue crack growth rates (for example, by a larger density of microcracks) in the vicinity of the weld.

An analysis of stresses was therefore initiated to estimate the temperatures and stresses during and after the welding. The estimation of welding residual stresses in a complex geometrical shape of the blanket first wall is considered to be a primary objective.

The accuracy of such estimates is known to depend heavily on the material models and data available. Defining the available and missing set of data is therefore another important goal.

Also, analyses of such kind are expected to support the optimization of the welding procedure as they can give good insight in the complex processes involved.

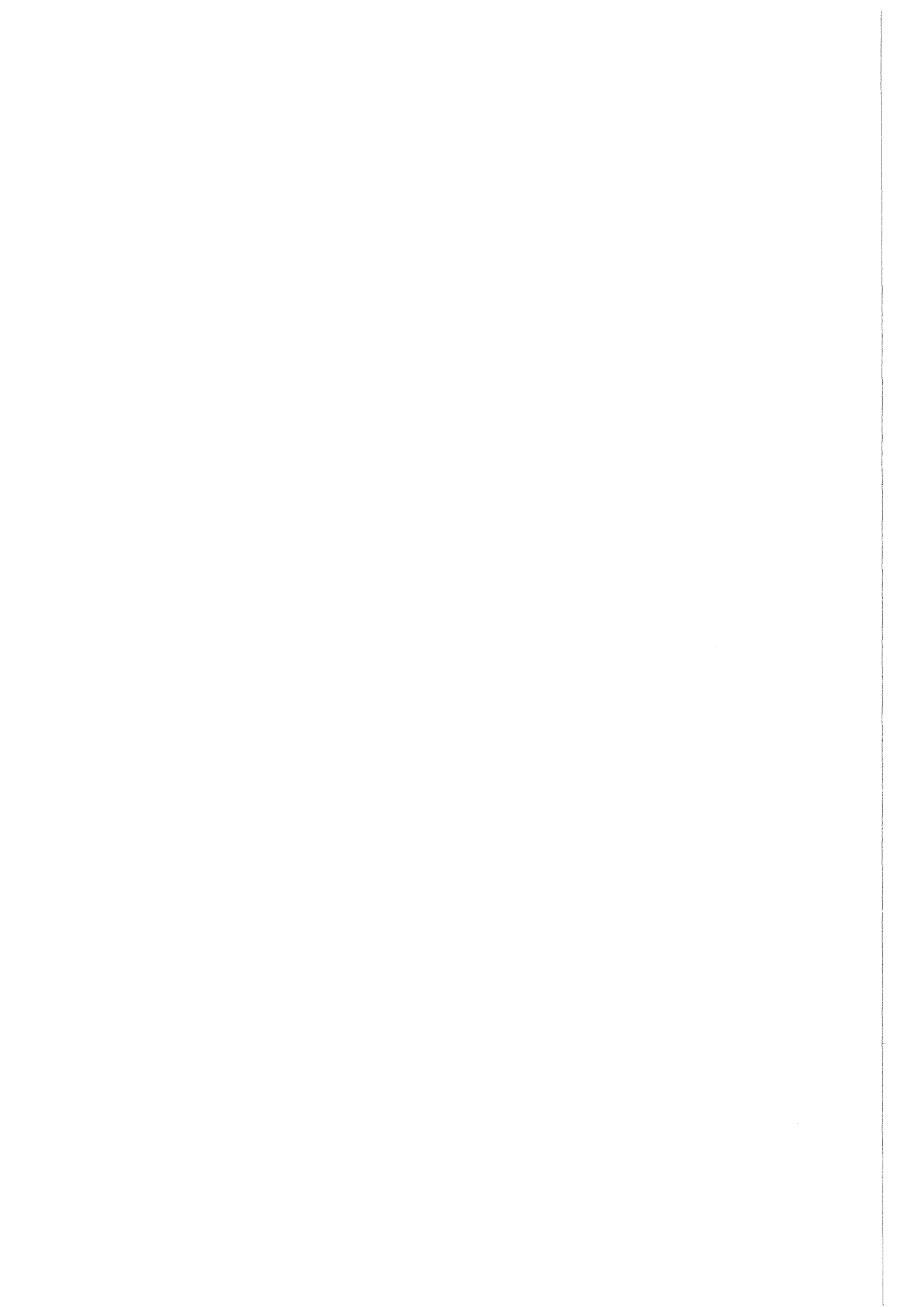
### 1.4 Organization of this report

Section 2 gives a brief review of the state-of-the-art achieved in the simulation of welding processes aimed at explaining the temperature and stress states during and after welding. Also, some possible consequences of high strains during welding such as hot cracking are indicated, together with the predictive methods used. As no computer simulation of the electron beam welding process appears to be available, some comments of the applicability of techniques used in analyses of arc welding are given.

Section 3 represents the main body of this report and discusses in some detail the modelling approach and data base utilized in the simulation. The full description of available and assumed material properties is however given in App. A. Results of simulation which describe the temperature, stress and strain field, are given in Section 3.

For the experimental evidence available when this analysis was performed, reader is referred to App. B. A set of simulations on a simple shape of butt welded plate is described there aimed at comparing the model predictions with the available measured data.

Conclusions (Section 4) summarize the work and underline the important results and weak points of the analysis. Some important topics for further work are suggested.



## 2 SURVEY OF COMPUTATIONAL WELD MECHANICS

The continuum mechanics can and should be directly applied to the analysis of welds [13]. However, there are some aspects peculiar to the weld mechanics. These are the richness of interaction between various phenomena (Fig. 2-1), the range of temperatures and the range of length scales (details on the order of 1 mm or less have to be analyzed in the workpieces of the order of 1-10 m).

A brief description of the processes controlling the stresses during and after welding is therefore given below, followed by an overview of the state-of-the-art of the modelling, as applicable to the arc welding. The applicability of modelling concepts described to electron beam welds is discussed at the end of this section.

Reviews on the welding phenomena and appropriate analysis techniques are in refs. [13, 18, 25, 8, 30].

### 2.1 Development of welding stresses

The magnitude and distribution of stresses in welds depend on coupled effects of thermal, mechanical and microstructural processes, as shown in Fig. 2-1 [13]. The particular processes and appropriate modelling approaches employed are examined in some detail in next sections.

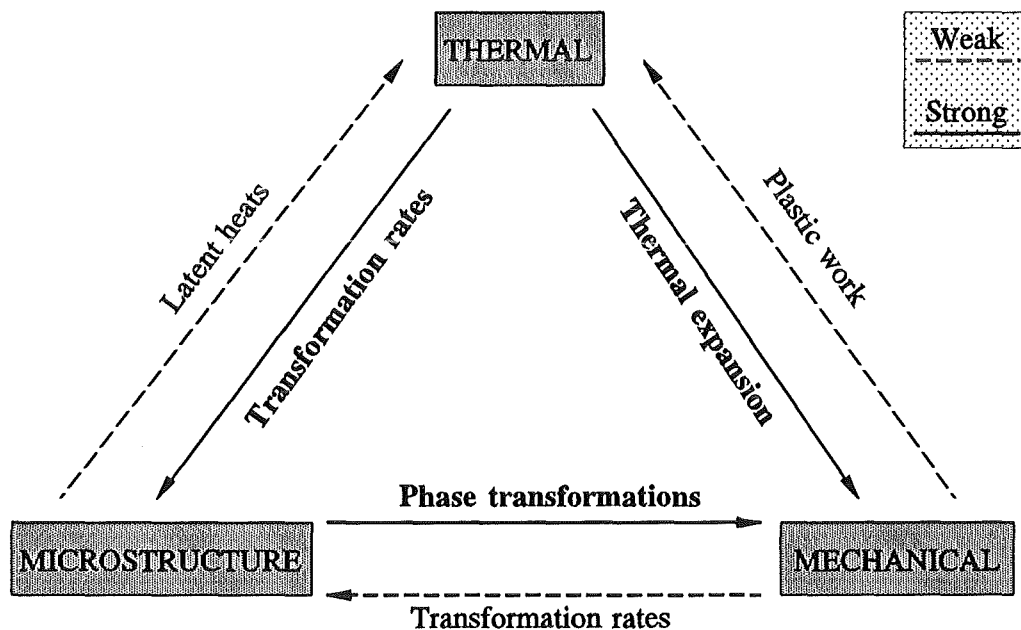


Fig. 2-1 Coupling between thermal, mechanical and microstructural effects (after [13])

### **2.1.1 Heating**

The following discussion is concerned with the stresses, parallel to the welding direction (longitudinal stresses) at the surface of butt-welded plates. The discussion may be also generalized to other geometries, while keeping in mind the important contribution of additional thermal restraints introduced by the shape of the workpiece.

During the welding the workpiece is locally heated over the melting temperature. This is done in a relatively short time which prevents excessive heat losses through conduction (diffusion). Consequently, steep temperature gradients develop causing rather localized thermal expansion of the material in the vicinity of the weld, which is severely restrained by the adjacent cold parts of the workpiece. Consequently, compressive stresses develop in the heated parts while tensile stresses are dominating in the colder parts of the workpiece.

In addition to that, the majority of steels exhibit solid state phase changes while heated over certain temperatures. In the vicinity of weld, in the so-called **Heat Affected Zone (HAZ)**, the microstructural changes like phase transformations and grain growth may take place. Exceeding the austenitization temperature causes solid state phase transformation to austenite, which is on the macroscopic level observed as volume shrinking. High temperature volume changes generally do not significantly contribute to the residual stresses as the yield strength is low at such temperatures. However, they may cause additional straining of (very soft) material in the vicinity of the weld.

The temperature dependence of material mechanical properties such as Young's modulus and yield strength significantly affects the magnitude and distribution of stresses. For example, heating low alloy steels above 700°C causes yield strength to vanish. Large plastic straining may occur in the heated regions while the stresses are mostly transferred to the colder and stiffer parts of the workpiece.

### **2.1.2 Cooling**

During cooling, the most heated and already considerably plastically strained parts of the workpiece shrink, which is obstructed by adjacent colder material. Consequently, tensile stresses build up in the vicinity of the weld while compressive stresses develop far away. This process is enhanced by the increasing value of yield strength.

The solid state transformations (not observed in austenitic stainless steels!) considerably affect the magnitude and distribution of stresses. In particular, the martensitic transformation is known to produce as much as 4% of the volume expansion [30], which is equivalent to the uniaxial strain of approx. 1.4%. As this transformation can only occur in the region heated over the austenitisation temperature, thus close to the weld, it tends to reduce or even change the sign of thermally caused tensile (residual) stresses.

### **2.1.3 Residual stresses**

The stresses which remain in the workpiece after cooling to room temperature are called residual stresses. The distribution and the magnitude of the residual stresses are affected by the effects already mentioned above. Some typical distributions which can be attributed to those effects and their joint action are shown schematically in Fig. 2-2 [8, 30].

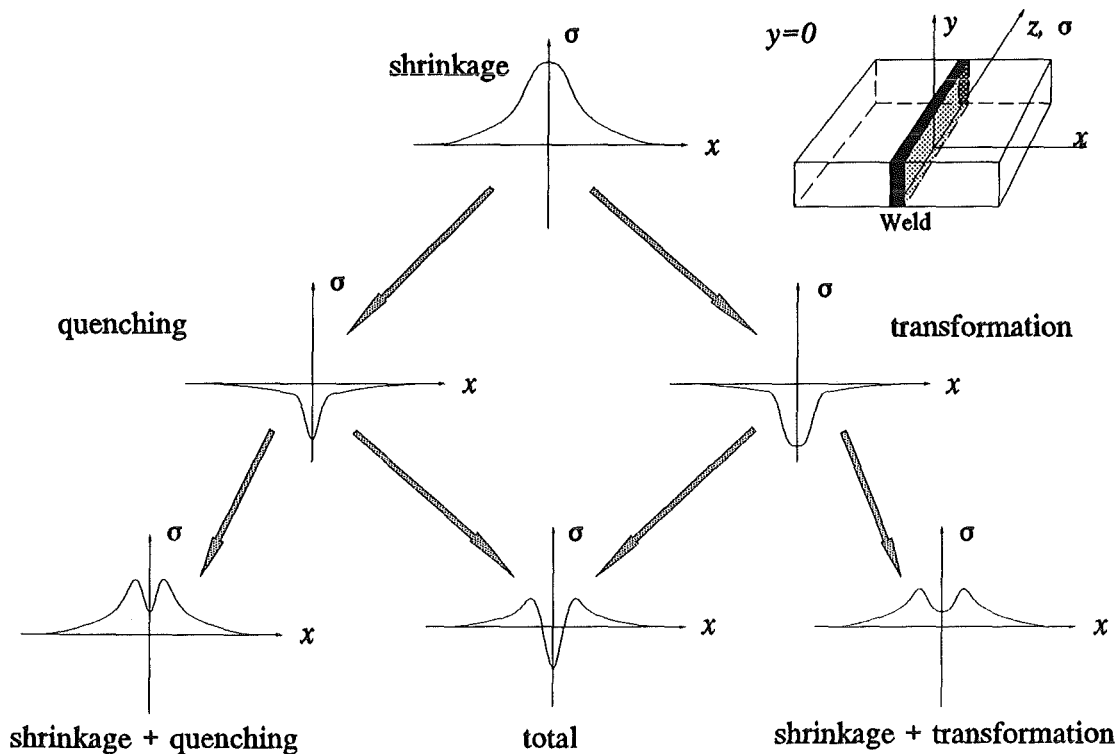


Fig. 2-2 Typical distributions of longitudinal residual stress at the surface of a butt-welded plate

The *shrinkage* residual stresses are pure thermal stresses and develop in a plate with virtually constant through the thickness temperature profile. The *quenching* residual stresses also have pure thermal origin and develop because of different cooling rates at the surface and in the middle of the plate. Therefore, quenching stresses are enhanced as the thickness of the plate increases. Finally, *transformation* residual stresses are caused by the volume expansion effects of the solid state phase transformations during cooling. Combination of all effects mentioned yield the distribution type denoted by *total*.

## 2.2 Heat transfer analysis

The heat transfer analysis in welded structures received due attention among the researchers. It has been recognized relatively early that closed form solutions are feasible for some practically interesting cases (e.g., Rosenthal and Schermbes, 1938 [25]).

### 2.2.1 Closed form solutions

#### Arc welding

The full description of the methods used is given in many textbooks [18, 25] and is not repeated here. The basic ideas and assumptions used are as follows:

- Welding arc (heat source) is moving with a constant velocity  $v$  along the workpiece (in  $z$  direction, Fig. 2-3). Then, a coordinate system  $(x, y, w)$  can be introduced:

$$w = z - v \cdot t \quad (1)$$

where  $t$  represents time. The temperature field in the  $(x, y, w)$  coordinate system does not explicitly depend on time, which allows a quasi-static treatment.

- Welding arc can be approximated as a line source (thin plates) or point source (thick plates). Further, the line source has constant intensity through the entire plate thickness.
- Temperature dependent physical properties are approximated by values averaged over the range of temperatures considered.
- Heat losses apart from heat conduction (diffusion) are considered negligible.
- Latent heats at phase changes are considered negligible.

In a two-dimensional case of an infinite plate of thickness  $h$ , heated by a line heat source of intensity  $q=Q/h$  [W/m] moving with velocity  $v$ , this leads to the following closed form solution of the quasi-static temperature field [25]:

$$\theta - \theta_0 = \frac{q}{2\pi\lambda} \exp\left(\frac{v}{2\kappa} w\right) K_0\left(\frac{v}{2\kappa} r\right) \quad (2)$$

where  $Q$  represents the power of the heat source [W],  $\theta$  and  $\theta_0$  the temperature and initial temperature, respectively.  $\kappa$  is thermal diffusivity [ $m^2/sec$ ],  $\lambda$  thermal conductivity [ $Wm^{-1}K^{-1}$ ] and  $K_0$  represents the modified Bessel function of the second kind and zero order:

$$K_0(z) = \int_{-1}^{\infty} \frac{e^{-zt}}{\sqrt{t^2 - 1}} dt \quad (3)$$

The position within the plate  $r$  is defined by:

$$r = \sqrt{w^2 + x^2} \quad (4)$$

Some closed form solutions are also available for the starting and ending periods of welding (for details see Masubuchi [25]).

### Laser and electron beam welding

Theoretical study of heat transfer during laser or electron beam welding has been published [38]. It was based on the theoretical premises given above. It is recognized that power beam welding techniques fulfil the assumptions about the heat source shape (line source!) better than any of the classical arc techniques. This is also true for thick plates, as the beam can penetrate through the entire plate thickness.

The main conclusions concern theoretical limitations of certain welding parameters. An asymptotic analysis showed the following limiting relationships between the normalized melting width  $va/\kappa$  and normalized input power  $q/(\lambda T)$ :

$$\frac{v a}{\kappa} \approx 0.483 \cdot \frac{q}{\lambda T} \quad (5)$$

at high welding velocities  $v$  and:

$$\frac{v a}{\kappa} = \exp \left[ \ln(8) - \gamma - \frac{2 \pi \lambda T}{q} \right] \quad (6)$$

at low welding velocities. The parameters involved are as follows:

- $v$  welding velocity,
- $a$  the width of the welding bead (molten material),
- $\lambda, \kappa$  thermal conductivity  $\lambda$  and thermal diffusivity  $\kappa$  averaged over the analyzed range of temperatures,
- $T$  range of temperatures analyzed (as a first approximation, the melting temperature may be used directly, since room temperature contributes only about 1%),
- $\gamma$  Euler's constant (0.577...),
- $q$  power density of the line source representing the beam (see also eq. (2)).

Good agreement with experimentally determined values was found. Eqs. (5) and (6) may help in choice of appropriate welding parameters (for example, reduction in welding power  $q$  to achieve comparable welding bead  $a$  in preheated workpiece). Also, eq. (5) defines the proportion of the welding power, which can be used to melt the workpiece. Therefore, at least 52% of input power is dissipated by thermal diffusion.

### 2.2.2 Numerical solutions

The present state-of-the-art of the numerical methods such as finite element method enables routine analyses of highly non-linear temperature fields during welding [13, 18]. The temperature dependent material properties can be easily taken into account. Also, the fully coupled thermal, stress and microstructural analyses could be performed using finite element method [1, 13]. Such analyses are required when the generally weak dependence of temperature field on the strains (see Fig. 2-1) is considered significant.

A general assumption used in the majority of analyses is that the molten material obeys the same heat transfer laws valid for solid bodies. Some attempts to model the molten weld pool separately are also reported [13].

A detailed treatment of finite element methods in computational mechanics is given elsewhere ([13], [18] and references therein) and will not be repeated here. Nevertheless, some specific approaches used in analysis of welds are reviewed below.

### Geometrical simplifications

Full solutions of three-dimensional, transient and non-linear temperature fields are still a challenge in terms of computing resources available. Therefore, a short review of useful simplifications is given below.

The first simplified finite element analyses used a combination of one-dimensional analysis and quasi-static assumptions described in Sect. 2.2.1 [18]. The essential underlying assumption was that the heat flow along the weld direction is negligible. A one-dimensional transient analysis was therefore performed yielding a temperature field in the form  $T(x, t)$ . For the stress analysis, the thermal field was expanded to a two-dimensional form following the rule:

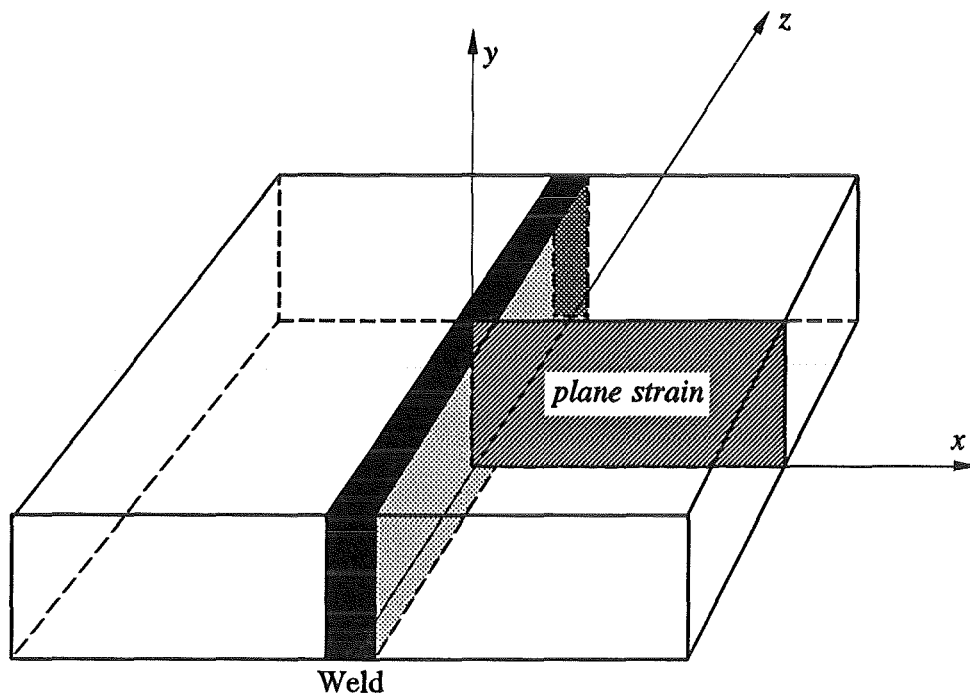


Fig. 2-3 A plate to be welded

$$T(x, y, t) = \begin{cases} T(x, t-y/v), & y - vt \leq 0 \\ 20^\circ\text{C}, & y - vt > 0 \end{cases} \quad (7)$$

A similar expansion based on a two-dimensional analysis was recently used to approximate a three-dimensional transient temperature field [27].

Two dimensional analyses of welded plates were performed in two different reference planes ( $x$ - $y$  and  $x$ - $z$  in Fig. 2-3). Analysis of  $x$ - $y$  plane assumes negligible heat flow along the weld (high welding speed), but also significant heat losses through the surfaces of the plate. Also, such kind of analysis can only be used to solve for temperatures far from discontinuities such as start or end of the weld. On the other hand, when heat losses through the surfaces were considered negligible and heat flow along the weld was important (low welding speed), the  $x$ - $z$  plane was analyzed.

Recently, full three-dimensional transient analyses have been published [6], also considering full coupling with mechanical and microstructural effects [33].

### Heat sources

The energy of the welding arc was consistently modeled as prescribed body or surface heat flux [18 and references therein] of appropriate magnitude. In the case of a  $x$ - $y$  plane analysis, the heat flux was turned on at the beginning of the analysis. After appropriate time, e.g., time needed by molten pool to pass the thickness analyzed, the heat source was turned off. A modelling of a moving heat source is needed in  $x$ - $z$  two-dimensional and three-dimensional analyses.

## Heat losses

During the welding, only the conduction heat transfer is important. Later, during the cooling phase, the surface heat losses begin to dominate, which was not accounted for in the closed form solutions.

Apart from conduction heat losses, radiation and convection can be modelled in a straightforward manner using finite elements. In simplified analyses ( $x$ - $z$  plane, Fig. 2-3), the surface heat losses have to be simulated through effective conductivity or appropriate body heat sinks. Karlsson [18] recommends use of body heat sinks, since use of effective conductivity results in erroneous temperature fields.

In simplified  $x$ - $y$  and full three-dimensional analysis, direct use of appropriate boundary conditions is recommended. Such approach is also required in the underwater welding conditions, where the surface heat losses essentially control the heat transfer [33].

## 2.3 Microstructural considerations

The microstructure depends on the chemical composition of the steel and on its thermal and mechanical history. It may be defined in terms of fraction, composition and grain size of each solid state phase present. In steels, the most common phases are ferrite, perlite, bainite, austenite, martensite and liquid [13].

For a specific steel, the thermal history is the most important factor. For thermal histories with high cooling rates which are typical for the welds and associated heat affected zones, the microstructure might be completely different from that found in virgin material. Some steels however do not exhibit phase transformations while subjected to severe thermal cycles. An example are austenitic (stainless) steels [18].

In this section, the phenomena which influence the stresses during welding are briefly reviewed, together with some of analytical techniques proposed to be used in computational weld mechanics. Detailed information can be found in [2, 7, 13, 8] and references therein.

We should note here that a lot of specific data and dedicated modelling is required for satisfactory simulation of the phenomena reviewed below.

### 2.3.1 Solid state phase transformations

The phase transformations of practical concern in the computational weld mechanics are only those which develop during the cooling phase of the welding thermal cycle. The first necessary condition to observe those transformation is to keep the steel over the austenitisation temperature for the sufficiently long time to allow the development of the austenitic phase to develop. This condition restricts the region of the transformation to the vicinity of the weld. The subsequent development of the possible transformations depends mostly on the cooling rate and the stress state (see Sec. 2.3.2) of the material. Faster cooling rates in general produce phases with higher hardness and yield strength (e.g., martensite). Type of phase and hardness to be obtained by using specific cooling rates are usually given in CCT diagrams, which generally differ with grain size and type of the alloy [13]. As the

cooling rates differ as function of a distance from weld, a distribution of fractions of different phases may be observed in the heat affected zone.

From the viewpoint of strain field, there are two important effects of phase transformations:

- Such transformations are observed on the macroscopic level as a significant volume expansion (austenite-martensite about 4% [24]).
- The mechanical (and physical) properties of each resulting phase may be significantly different.

These effects mainly governed the analytical effort. In the first analyses, only the effects of expansion/shrinking have been taken into account through the appropriate setting of the linear thermal expansion coefficient [18].

Recent analyses are directed towards full description of the transformation kinetics and trace the development of all possible solid state phases. The mechanical and physical properties of the mixture of phases are then given as a weighted average of the properties of specific phases [2, 7]. Beside accurate data on the development of solid state phases, a complete set of temperature dependent material properties for each phase is needed.

### **2.3.2 Transformation plasticity**

If a stressed body undergoes a phase transformation, considerable permanent deformations which are finite in amount, independent of time and proportional to stress, can develop even at stress level which is considerably less than yield strength. A simple explanation is that volume changes caused by the phase transformations of microscopic volumes can induce local plastic deformations. The interaction of these microscopic stresses with the macroscopic stress field than cause an irreversible strain. According to Goldak [13], the contribution of transformation plasticity should be accounted for directly in the strain tensor.

Detailed description of phenomenon and appropriate analytical possibilities is given in [9] and [13].

### **2.3.3 Hot cracking**

Hot cracking is believed to be caused at temperatures of about 1200-1300°C during the cooling of the weld. According to Karlsson [18], four major factors increase influence the risk of formation of hot cracks:

- Chemical composition of materials involved. Presence of elements which tend to segregate (in steels S, O, B, P etc.) and therefore weaken the grain interfaces.
- The geometry of the joint. For example, welding of long plates tend to exhibit large displacements (strains) perpendicular to the weld at plate ends.
- The coarseness of solidification microstructure. Generally, high energy welding produces the largest grain growth.
- Stresses and strains. Overstressing the grain interface weakened by segregation may cause initiation of (micro) cracks.

Electron beam welding is known to produce comparatively high segregation during solidification and intergranular segregation over the dendrite surface irrespective of the steel grades [40]. Appropriate attention should therefore be given to assure acceptable properties of the weld.

Karlsson [18] proposed the change in pure mechanical strain acting perpendicular to the weld between temperatures 1400 and 1000°C ( $\Delta\epsilon_{14/10}$ ) as a measure of the risk of hot cracking. Conclusions are rather general: larger values of  $\Delta\epsilon_{14/10}$  are supposed to cause more hot cracking. Also, another qualitative conclusion is that high energy and low speed welding tends to enhance the probability of hot cracking in butt-welded plates. High input energy is therefore a reason more to analyze electron beam welding.

## 2.4 Thermal stress analysis

Numerical methods such as finite element method which were developed to solve a large class of solid mechanics problems are used in computational weld mechanics [13, 18]. Some special problems of thermal stress analysis of welds are as follows:

- Temperatures at which the behaviour of the workpiece is analyzed range from room temperature to the melting temperature or even higher. Appropriate constitutive modelling and accurate data on material properties is of utmost importance.
- The thermal and microstructural effects causing welding stresses are localized in the 1% or less of the volume to be analyzed. In some cases, this requires implementation of adaptive meshing or substructuring techniques.
- Richness of interactions among various phenomena (Fig. 2-1) requires special attention. The strong interactions denoted by bold lines in Fig. 2-1 should be taken into account to obtain approximate results, while all of them should be considered in an accurate analysis [13].

### 2.4.1 Constitutive models

Elastic-plastic models with temperature dependent material properties are necessary during the welding phase in order to obtain approximate magnitudes and distributions of residual stresses. In the analysis of post-weld heat treatment, the relaxation through creep can dominate the development of stresses and should be modelled adequately [13, 18].

At temperatures exceeding approx. 1000°C, constant value of thermal strain was assumed in many analyses [18]. This may be explained by the rather soft material response in this temperature range which may cause considerable numerical difficulties. At the same time, the contribution of strains at high temperatures to the residual stress distribution is rather small (about 5% in the metal without phase transformations [27]).

Some attempts to use visco-plastic models during the welding phase are also reported [13, 33]. Inoue [16] also proposed a convertible visco-plastic model, which asymptotically describes both Newtonian fluid and Hooke's elastic solid.

The accurate data on temperature dependent material properties are recognized as an imperative factor affecting the accuracy of simulations. In the case that the stress analysis is coupled to the microstructural analysis, the material properties depend directly on the

development of the microstructure. This makes the task of obtaining appropriate values even more demanding.

#### 2.4.2 Simplifications of geometry

Plane strain and generalized plane strain were mainly used to analyze through-the thickness distributions in structures far from discontinuities like beginning or end of weld. In cases where the effects of discontinuities have been accounted for, full three-dimensional transient analyses have been performed [13].

### 2.5 Application to electron beam welding

The methods outlined above have been applied to arc welding, to flame cutting of plates [21] and treatment of surfaces by the means of laser beams [4]. To the best of author's knowledge, no numerical analysis of the stresses generated during the electron beam welding have been published.

The methods reviewed in Sec. 2 were considered adequate to be used at least as a first approximation in the analysis of electron beam welding. They were used to the extent supported by the available data. Some additional complications of the stress analysis procedure which have been observed are as follows:

- Range of temperatures from room temperature to about the temperature of vaporizing. The solid body mechanical and thermal laws were assumed to hold also for both molten and vaporized material. This is justified by extremely small masses of molten and vaporized metal compared to the workpiece analyzed.
- Thermal cycle is significantly faster than at other welding procedures, especially during the heating phase:
  - melting temperature is reached at about 0.05 seconds. This may cause the strain rates in order of 1/sec, which in turn raise the question of strain rate importance.
  - standing time over austenitisation temperature is less than 3 sec.
  - $\Delta t_{8/5}$  is in the order 10 seconds or less.Very fine time stepping scheme (about 80 increments for the thermal and 250 for the stress analysis) has been found to adequately address these problems.
- The thermal and microstructural effects are only noticeable at very small distances from the weld, which is caused by very large heating power of the electron beam. This required particular attention during the phase of mesh generation.

For more detailed analysis, refined experimental support is crucial.

### 3 DOUBLE WELD BETWEEN BLANKET SEGMENTS

The analysis given in this section employs a non-linear transient solution of uncoupled thermal and stress fields. The microstructural effects are only considered in a rather crude way through sudden expansion of material to simulate the transformation from austenite to martensite (see Section 3.2.2 and Fig. 3-2). Further refinements of the model used are recommended pending new data on material properties.

#### 3.1 Summary of basic assumptions and limitations

Besides the assumptions which are usual in solving thermomechanical problems by the means of finite element method, the following specific assumptions have been made:

- **The material follows the laws valid for solid material in the entire range of temperatures analyzed.** The melting/solidification and vaporization/condensation transformations are only accounted for by the appropriate latent heat values and slightly higher conductivity values.
- **The constitutive models used do not account for many effects, which may be important,** especially at larger temperatures. Such effects are, for example, strain rate dependency, dynamic recrystallisation, different behaviour in tension and compression etc. More specific data is needed to overcome this limitation.
- **The results obtained are only applicable to the sections far away from the start/end of the weld.** This assumption enabled computationally efficient two-dimensional modelling.
- **The weld is assumed to have a constant width through the entire plate thickness.** Electron beam welds actually tend to have slightly larger width at the surface closer to the electron source, which might induce some additional thermal distortion not accounted for in the analysis.
- **The microstructural behaviour of martensitic stainless steel is most probably not modelled adequately.** However, more specific data are required to overcome this situation.

#### 3.2 Geometry

##### 3.2.1 Finite element mesh

A two dimensional mesh was developed as shown in Fig. 3-1. The mesh density is considered adequate based on the comparisons described in App. B.

Weld is located in the  $y$ - $z$  plane, which is also a plane of the symmetry of the model. The solidification lines of the weld are assumed to be parallel, which is not entirely true. This might result in the fact that model neglects some weld induced rotations around the out-of-plane ( $z$ ) axis.

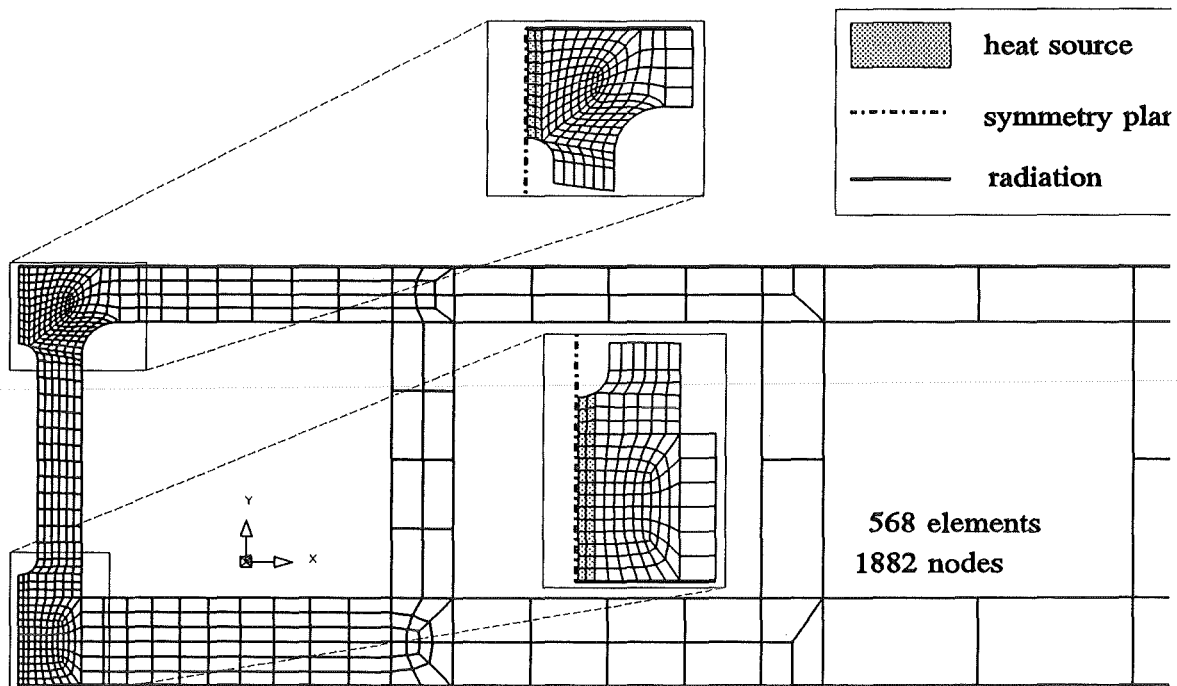


Fig. 3-1 Layout of the finite element mesh

The dimensions of the mesh contour are taken from [23]. The details which had to be assumed are as follows:

- Radius and half of the depth of leak detection slot is 1.5 mm.
- The length of the slot is 21 mm and its position is centred according to the helium cooling channel. The effective weld depths are therefore 7 and 10 mm.
- Radius in the helium cooling channel in the vicinity of weld is 3 mm.
- The wall containing the leak detection slot is 5 mm thick. This leads to the double wall thickness between two cooling channels in the order of 10 mm.

Elements used in are DC2D8 in thermal and CPGE10RH in stress analysis. Thus, generalized plane strain conditions have been assumed in the stress analysis. The thickness of the layer analyzed is 1 mm in both cases.

### 3.2.2 Loading

The only loading considered is the heat transmitted from the electron beam to the material. It was modelled as a body source with density of  $1.48 \cdot 10^{11} \text{ W/m}^3$ . The same value was used in the simulation of test welds (App. B). The volume of metal which interacts with electron beam is about 1/2 of that in the test plate, so welding requires about 1/2 of the electron beam power used for test welds. The heat source affected a 0.8 mm wide layer of elements along the weld centerline, as shown in Fig. 3-1. This width corresponds to the oscillatory motion of the electron beam during welding (see also App. B).

The heat source was suddenly turned on at the beginning of the analysis and completely turned off after 0.25 sec. This time corresponds to the time needed by electron beam with velocity of 4 mm/sec to pass the 1 mm thick layer analyzed. Thermal radiation with emissivity of 0.5 is assumed on both free surfaces.

Temperature fields obtained by thermal analysis were used to generate distributed loading for the subsequent stress analysis. The loading was in the form of thermal strains. A cut-off temperature of 1000°C was introduced, preventing thermal strains to further increase while exceeding this temperature (see Fig. 3-2). This improves convergence at higher temperatures where the stiffness of the material is vanishing. According to Näsström [27], the error in residual stresses caused by this simplification is in the order of 5%.

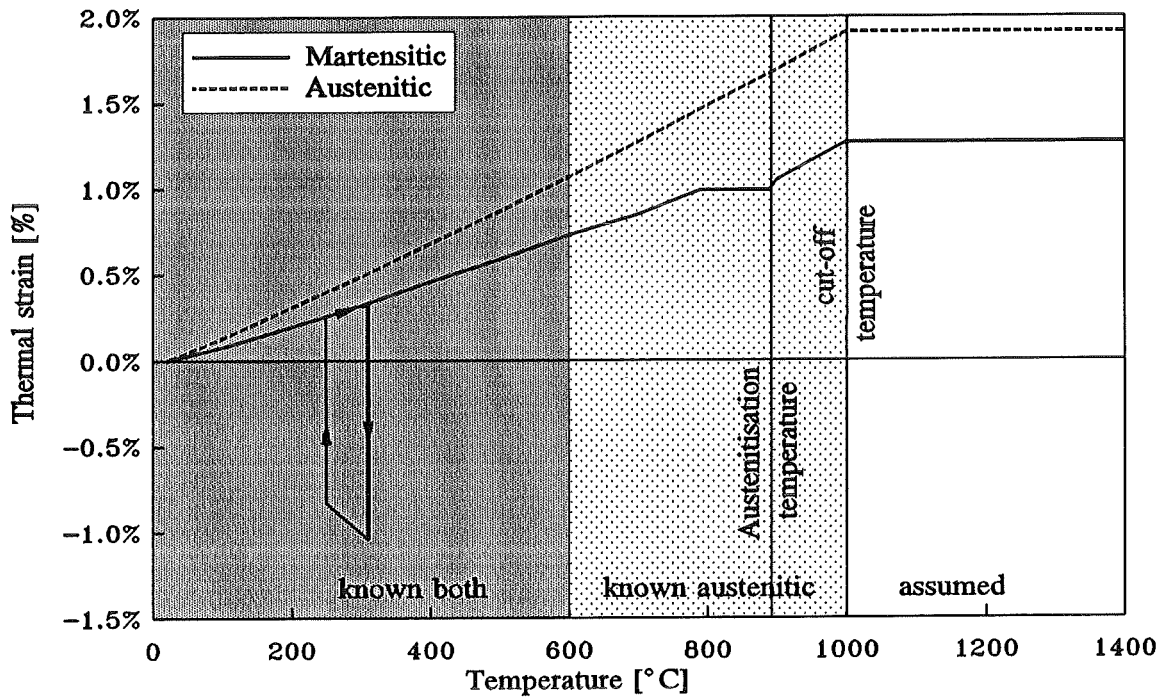


Fig. 3-2 Thermal strain as a function of temperature

The negative strain in the bold curve representing the behaviour of the martensitic steel simulates the sudden volume expansion observed during the austenite martensite transformation during **cooling**. This is a usual way of describing such transformation in the absence of appropriate material data (e.g., [18], [19]). The underlying assumptions and the appropriate values of linear expansion coefficients are given in App. A.

The thermal cycle during the heat treatment after the welding was described by an uniform temperature field. The temperature increase rate of 4°C/min was employed until 760°C was reached. A holding time of 2 hours finished with uniform cooling with the same rate.

### 3.3 Material model

Based on the detailed analysis of data available (see App. A), two different materials have been modelled. In subsequent text, they are denoted as austenitic (describing AISI 316 L) and martensitic (describing both MANET and DIN 1.4922).

The full analysis with austenitic material was only performed using the simple plate geometry (see App. B) and was not repeated for the double blanket weld. This suffices for some general conclusions which are given at the end of this chapter.

### 3.3.1 Thermal analysis

The variation of thermal conductivity and specific heat with temperature is given in Fig. 3-3. The values of densities were assumed independent of temperature and are quoted in App. 3.3.1.

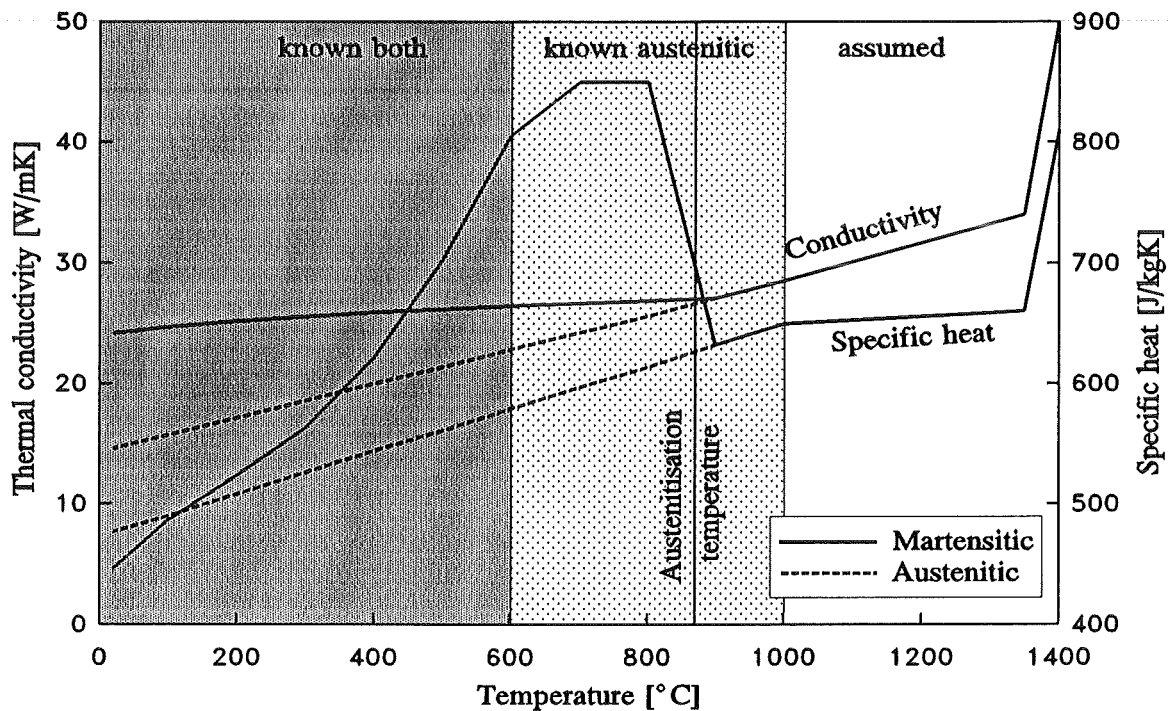


Fig. 3-3 Temperature dependence of conductivity and specific heat

In Figs. 3-2 to 3-5 the range of temperatures where the material properties are known is denoted by shadowed background. Light background therefore denotes **extrapolated** or **assumed** values.

### 3.3.2 Stress analysis

During the welding phase, time independent plasticity model with von Mises yield function, associated flow rule and isotropic hardening is assumed. The corresponding material parameters are shown in Figs. 3-4 and 3-5 (see also App. A). The selection of the material model is mainly based on the limited data available, which do not support more advanced constitutive models. However, relatively short duration of the welding phase (in the order of 10 sec) indicates possible strain rate effects which should be included in the model as soon as supported by material data.

Some processes specific to high temperatures as for example more pronounced differences in the tensile and compressive behaviour and dynamic recrystallisation are also neglected due to the lack of data. The effects of omissions on the residual stresses are however considered

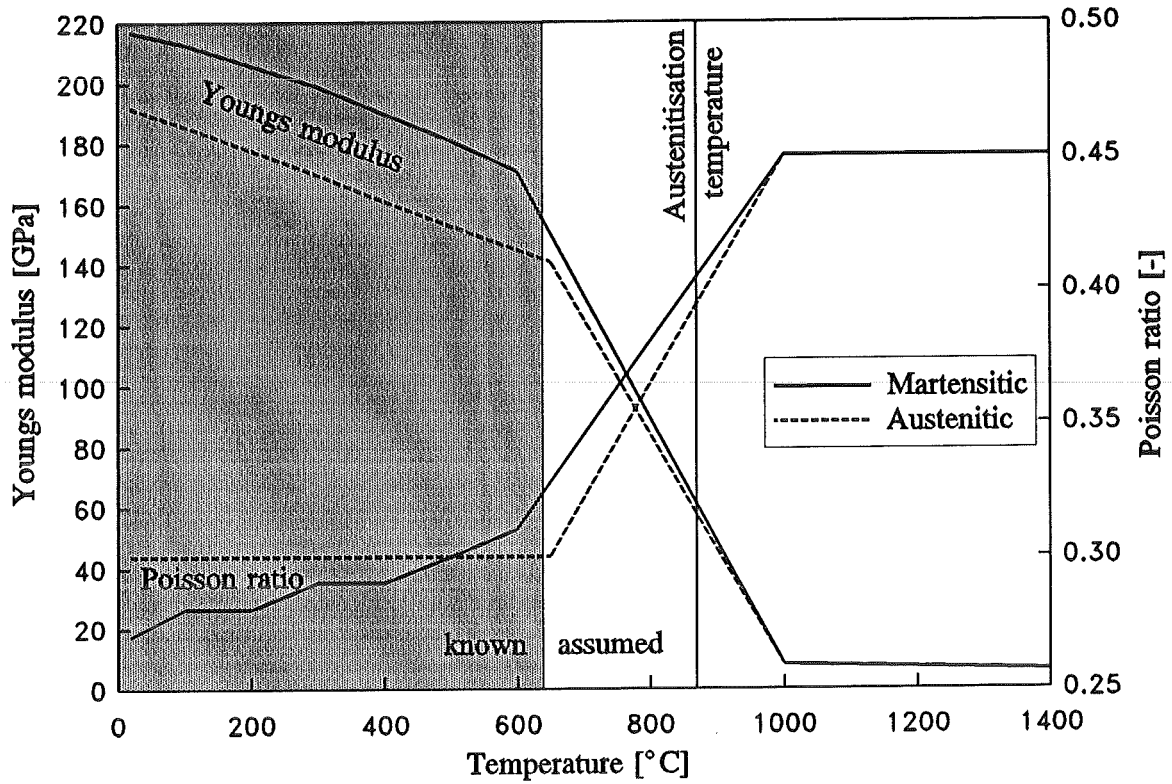


Fig. 3-4 Temperature dependence of Young modulus and Poisson ratio

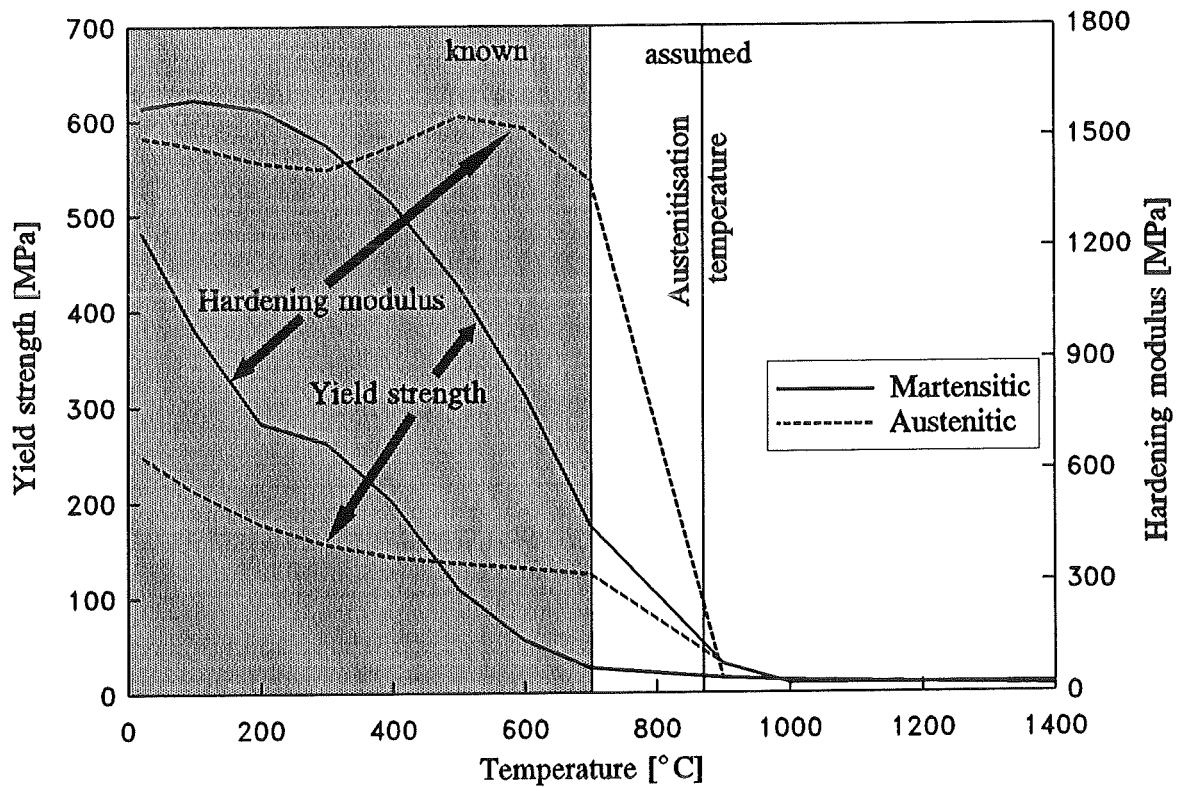


Fig. 3-5 Temperature dependence of yield strength and hardening modulus

insignificant, as the majority of the residual stresses build up at temperatures below say 700°C when the yield strength starts to increase.

During the heat treatment phase after the welding, a simple Norton creep was added to the material law described above. The material constants were assumed to be temperature dependent and are given in App. A.

### 3.4 Results of thermal analysis

Time history of the temperatures in the vicinity of the weld is given in Fig. 3-6. For the first 0.25 sec, the heat source was turned on simulating the presence of the electron beam. This causes the vaporization of the centerline of the weld. Temperatures at more distant points follow with increasing delay. After the heat source has been turned off (after 0.25 sec), a rapid decrease of temperatures close to the weld centerline is observed, while the temperature of remote points still increases because of conduction.

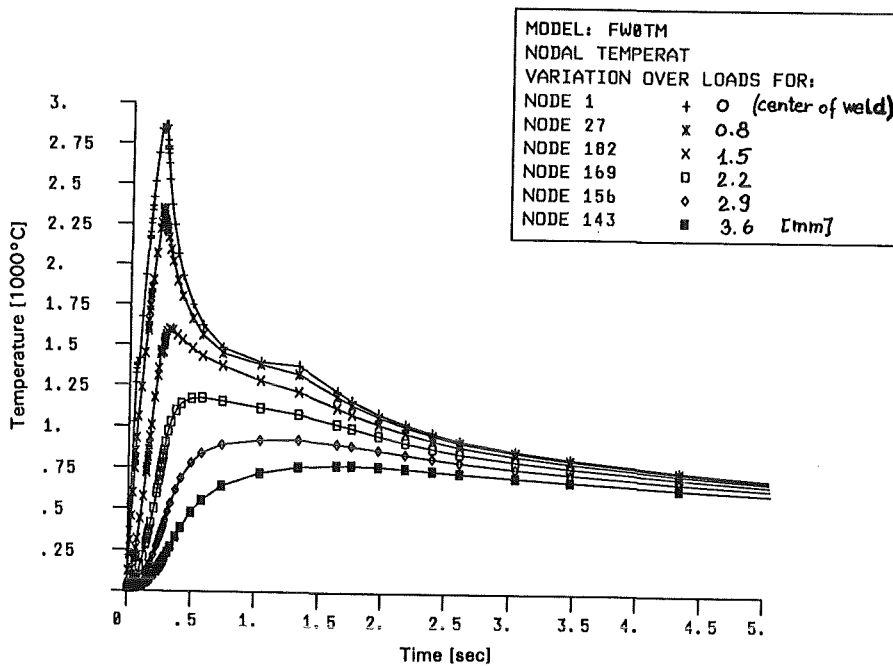


Fig. 3-6 Time history of temperatures in the vicinity of weld

Effect of the latent heat released during solidification is clearly shown as a plateau between 0.5 and 1.3 sec. After about 1.3 sec, all molten material has solidified.

It can be observed that melting temperature propagates about 2 mm out of the weld centerline, indicating about 4 mm thick weld (molten layer of material). The austenitisation temperature (870°) is reached in the 3 mm thick layer. Note that time while the points at the distance of 3 mm apart from weld centerline are overheated for an extremely short time, which may not suffice for full development of austenitic phase.

Figs. 3-7 to 3-15 represent the position at temperature fronts at selected times. The temperature scale reflects the melting (1400°C) and austenitisation (870°C) temperature. Besides, some lower temperature values are included to show rather slow propagation of the input heat.

The shape of the temperature fronts reveals a typical one-dimensional heat transfer along both surfaces (plasma and liquid metal) of the first wall. Close to the leak detection slot, typical two dimensional pattern develops, which is caused by the conduction through the wall containing the leak detection slot. This causes significantly faster cooling in the vicinity of the leak detection slot than elsewhere.

The so called *heat affected zone* in both parts of the double weld is clearly shown on Fig 3-13 (line D). However, we should mention here that the heat affected zone actually extends around more than half of the arcs of leak detection slots (compare line D on Figs. 3-11 and 3-12. Due to rather fast conduction through the wall between both parts of the weld, these small sections are cooled down extremely fast.

The cooling time between 800 and 500°C ( $t_{8/5}$ ) in the center of the weld is predicted to be:

8.2 sec	without preheating and
8.6 sec	with preheating to 100°C.

Uniform temperature field is reached in about one hour at temperature of approx 77.°C (83°C if preheated to 100°). Extremely slow cooling to room temperature through radiation follows.

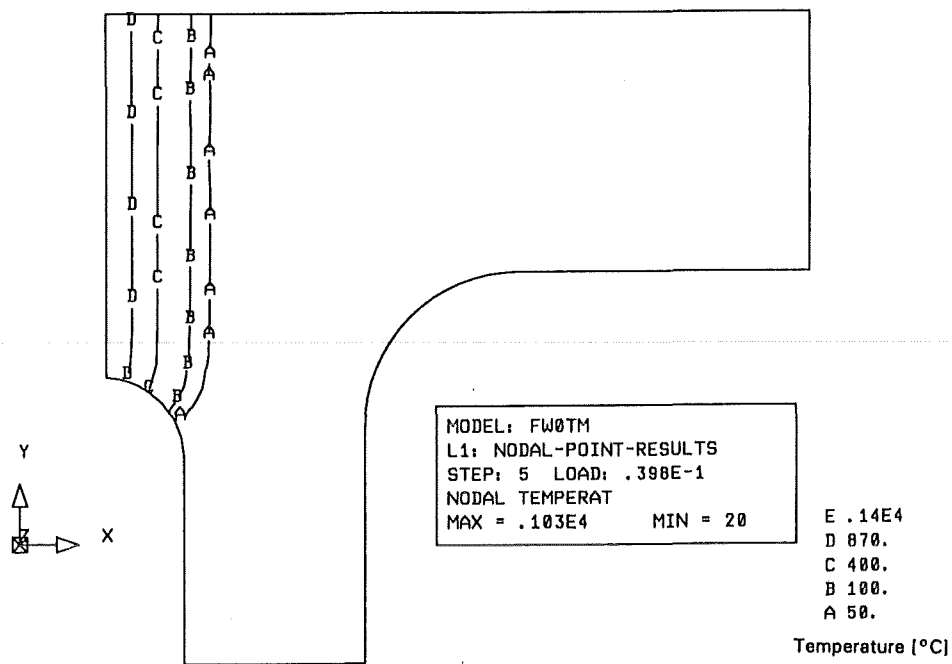


Fig. 3-7 Distribution of temperatures at 0.04 sec (plasma side weld)

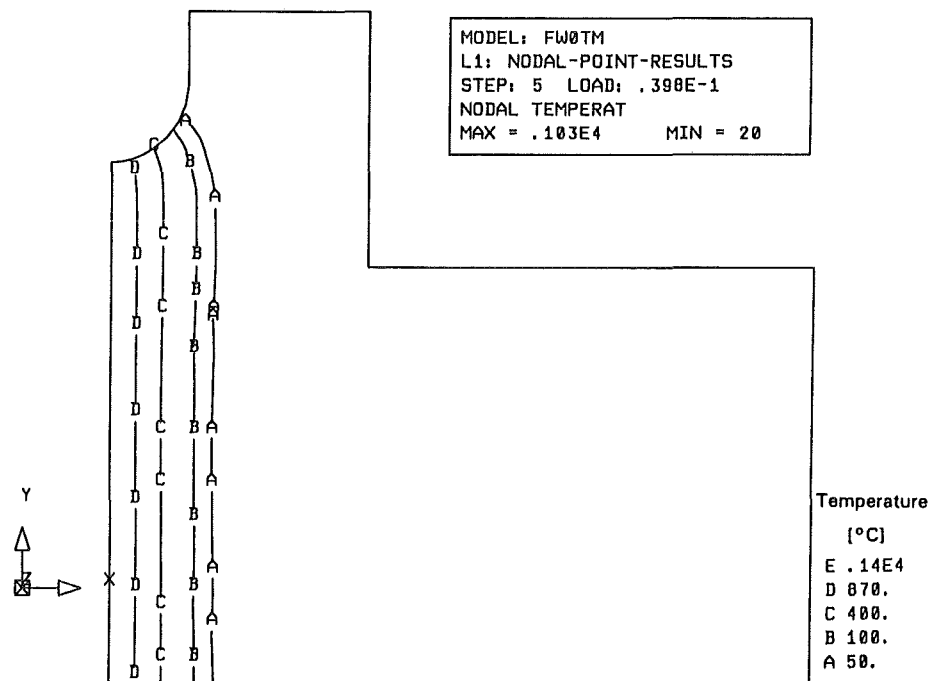


Fig. 3-8 Distribution of temperatures at 0.04 sec (liquid metal side weld)

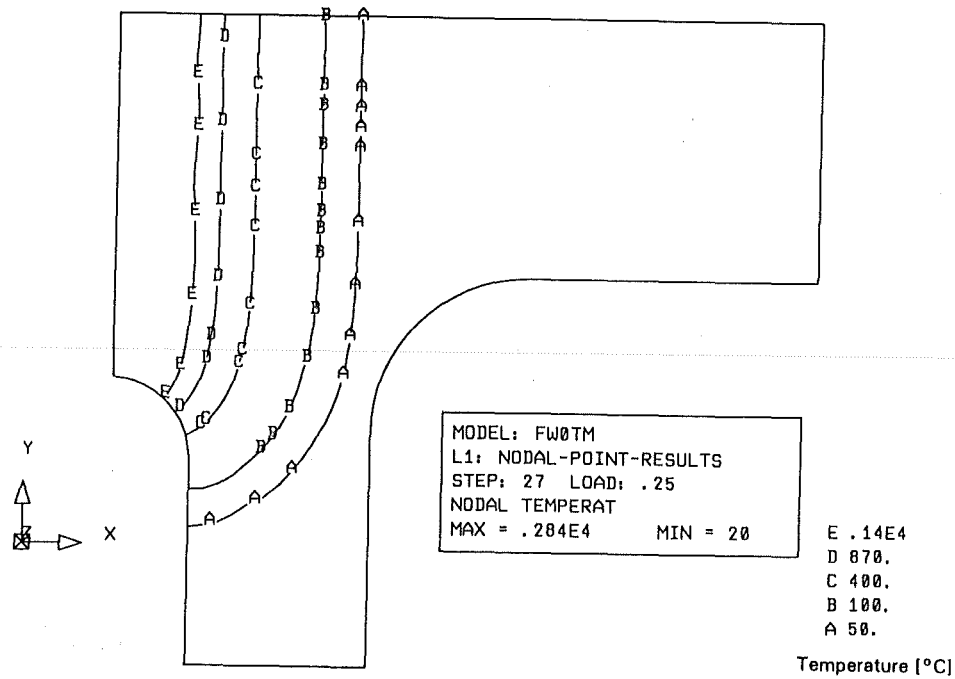


Fig. 3-9 Distribution of temperatures at 0.25 sec (plasma side weld)

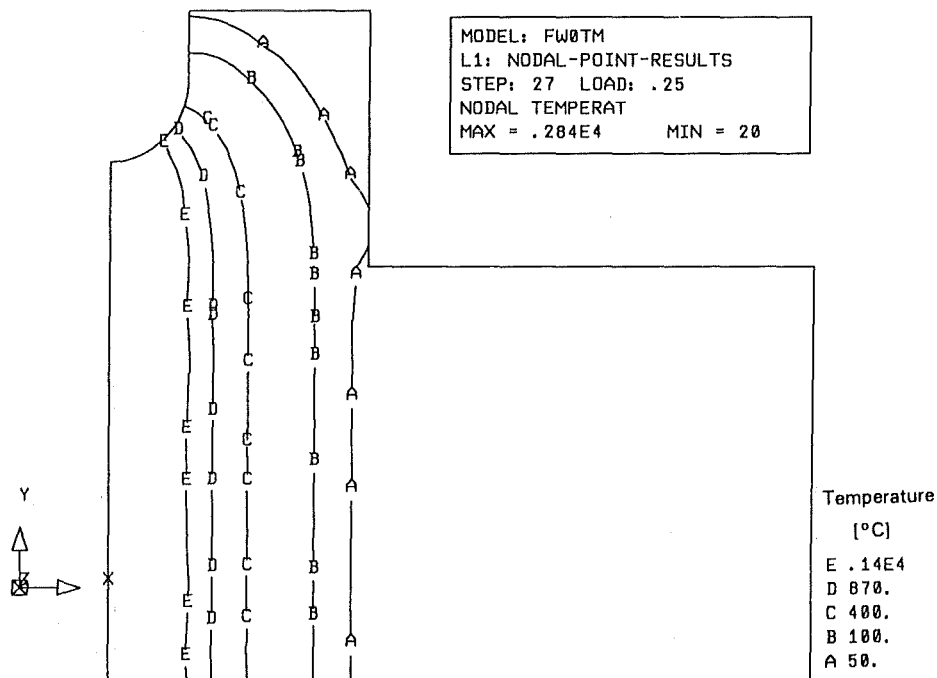


Fig. 3-10 Distribution of temperatures at 0.25 sec (liquid metal side weld)

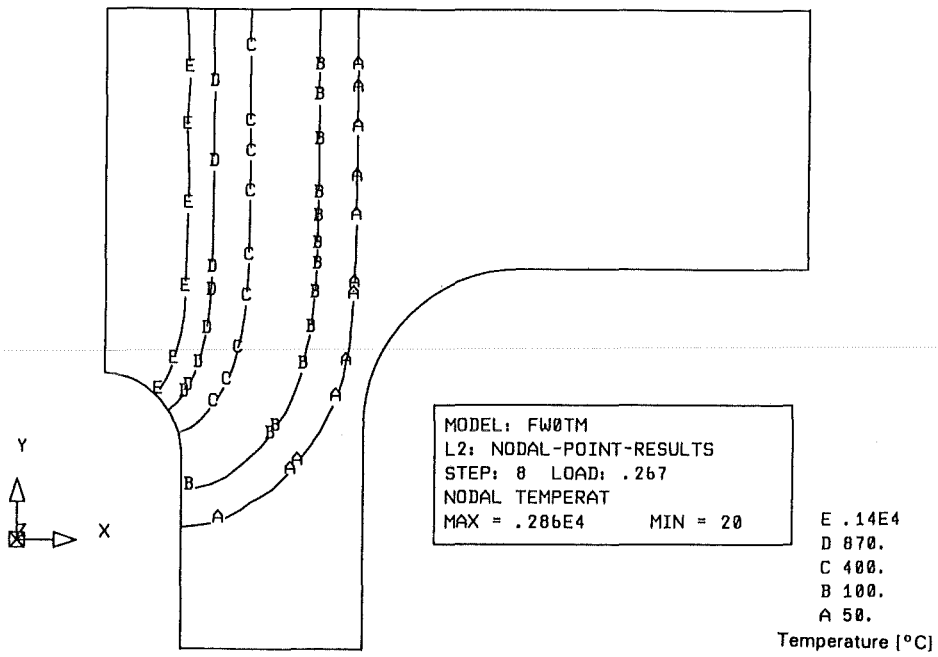


Fig. 3-11 Distribution of temperatures at 0.267 sec (plasma side weld)

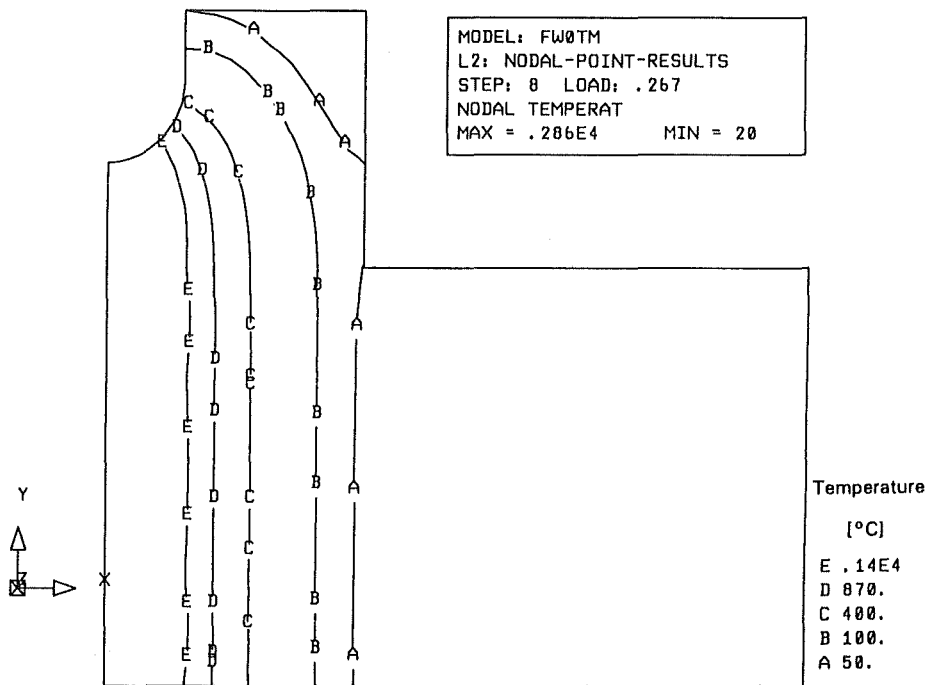


Fig. 3-12 Distribution of temperatures at 0.267 sec (liquid metal side weld)

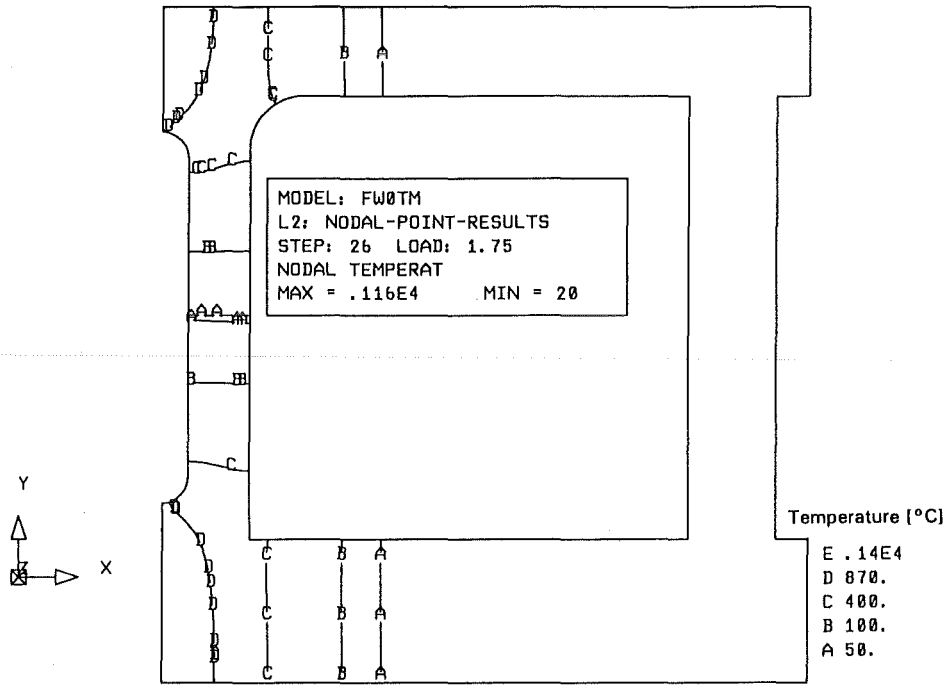


Fig. 3-13 Distribution of temperatures at 1.75 sec

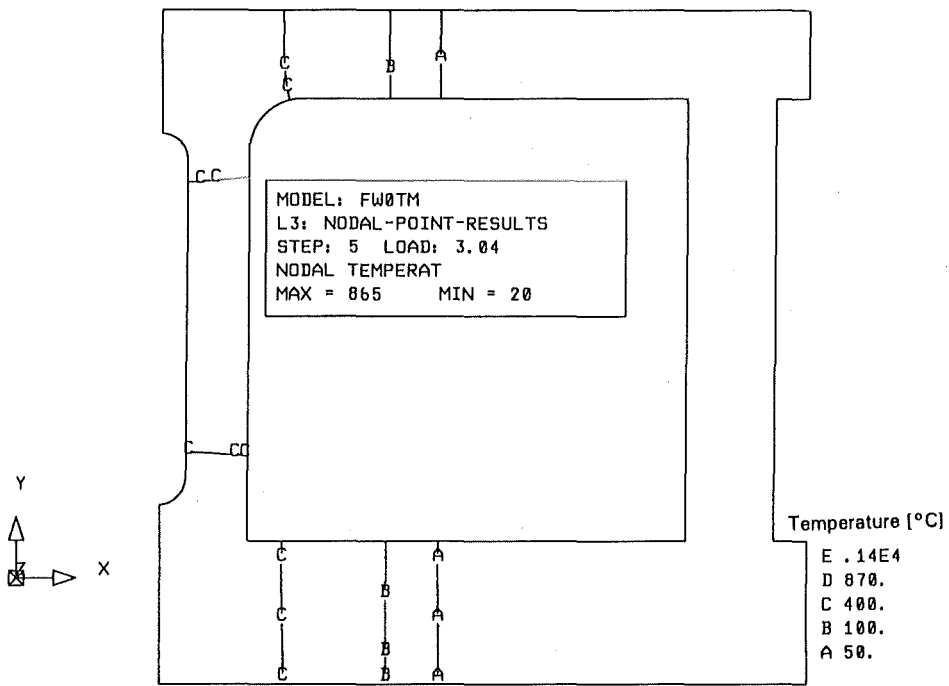


Fig. 3-14 Distribution of temperatures at 3.04 sec

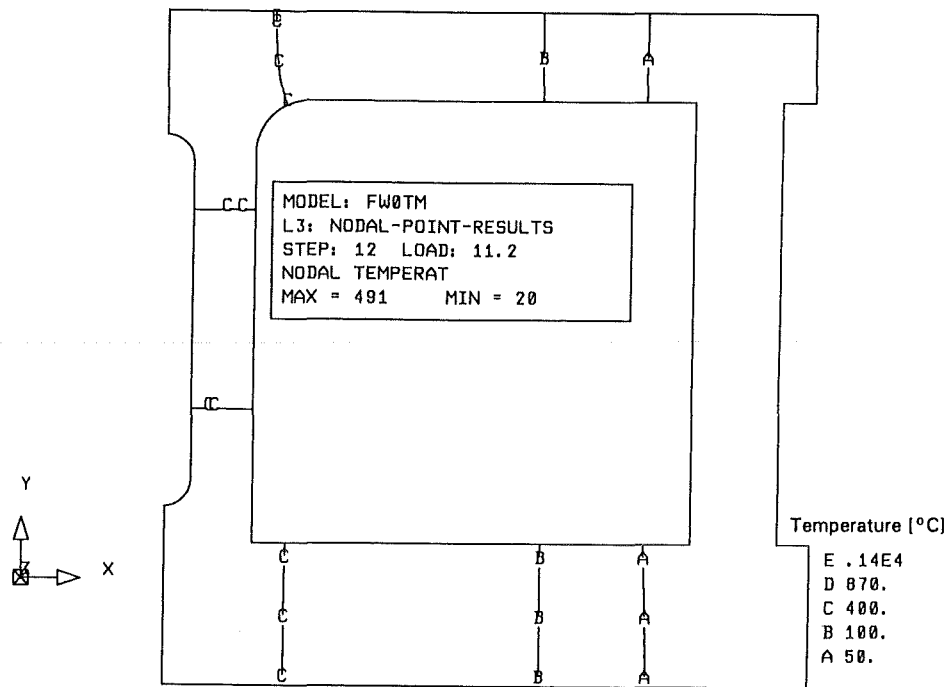


Fig. 3-15 Distribution of temperatures at 11.2 sec

### 3.5 Results of stress analysis

During welding, longitudinal (zz) stress dominates the stress field in plates completely (see App. B). This also holds for the complex shape of the blanket first wall as shown in Figs. 3-16, 3-17, 3-18 and 3-19. However, an additional effect emerges in the wall containing the leak detection slot. This are rather high bending stresses of about  $\pm 250$  MPa (Figs. 3-20 and 3-21), which is caused by the thermal expansion of welds while the base of the wall is still relatively cold and therefore also stiff. This effects becomes negligible about 1 sec later as soon the base of the wall softens enough because of heat conduction as shown in Figs. 3-22, 3-23, 3-24, 3-25 and 3-26.

#### 3.5.1 Effects of preheating

Preheating of the workpiece to  $100^{\circ}\text{C}$  prior to the welding did not have significant effects on the temperature field and residual stresses. It however significantly reduces tensile strains perpendicular to the weld (compare Figs 3-27 and 3-28) and therefore the probability of development of hot (solidification) cracks.

As this observation is made in the range of temperatures with unknown (and therefore assumed) material properties, further investigations are needed to verify this observation. Also, the extremely high values of tensile strains in the corners of the mesh (compare Figs. 3-27 and 3-28) should be at least partially attributed to the convergency problems which are caused by rather large difference in stiffness among the elements in mesh and also by highly non-linear nature of the model itself.

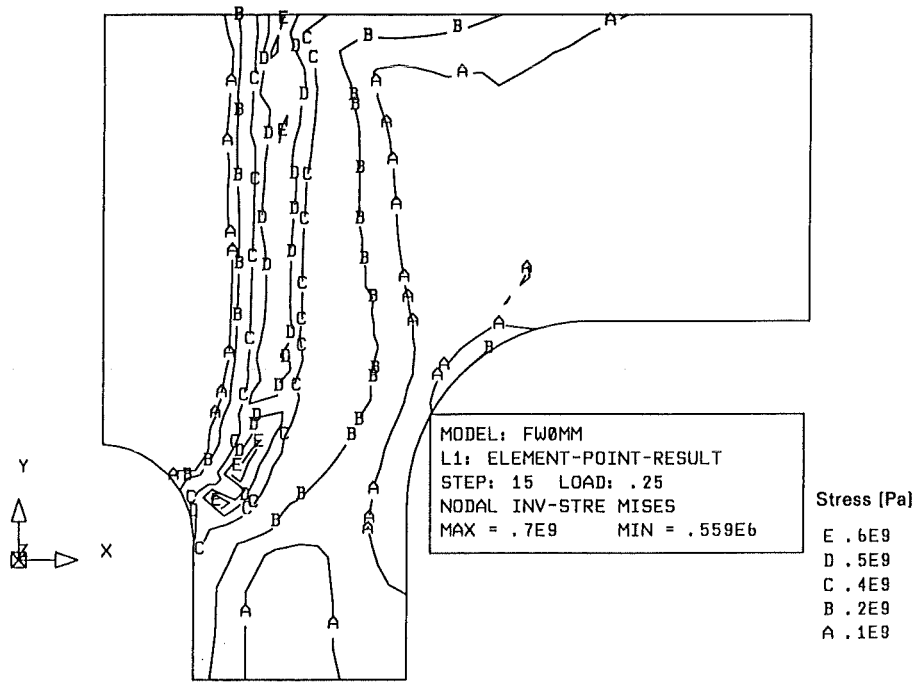


Fig. 3-16 Equivalent (von Mises) stresses during heating (plasma side weld)

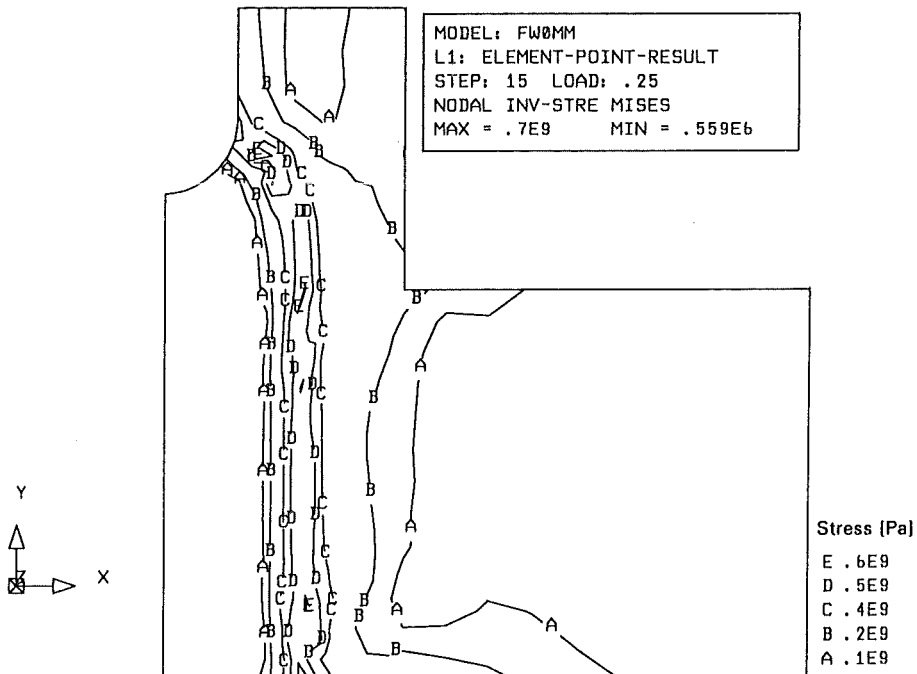


Fig. 3-17 Equivalent (von Mises) stresses during heating (liquid metal side weld)

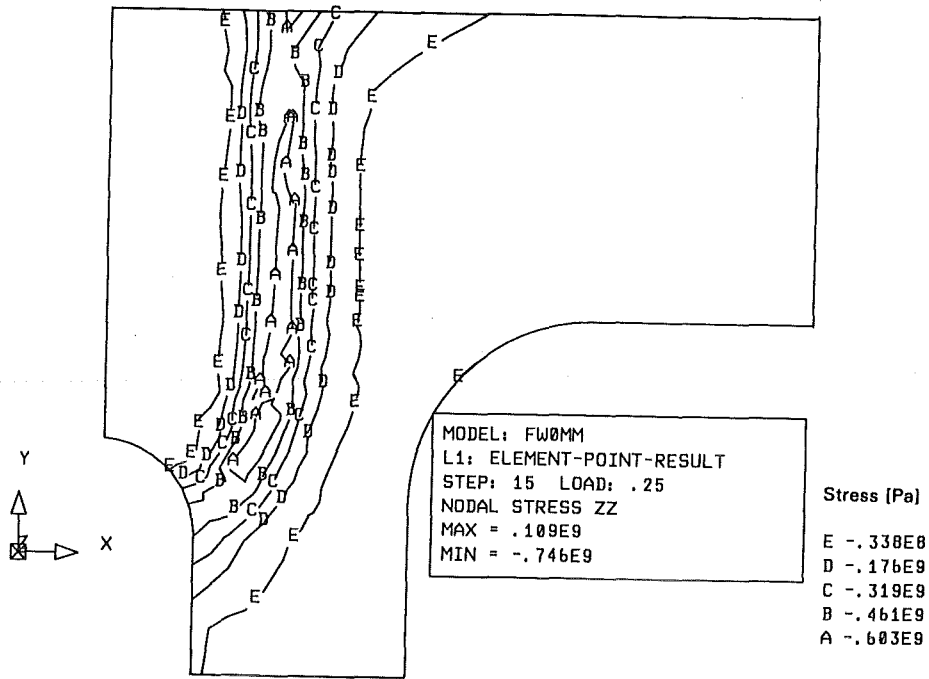


Fig. 3-18 Longitudinal stresses during heating (plasma side weld)

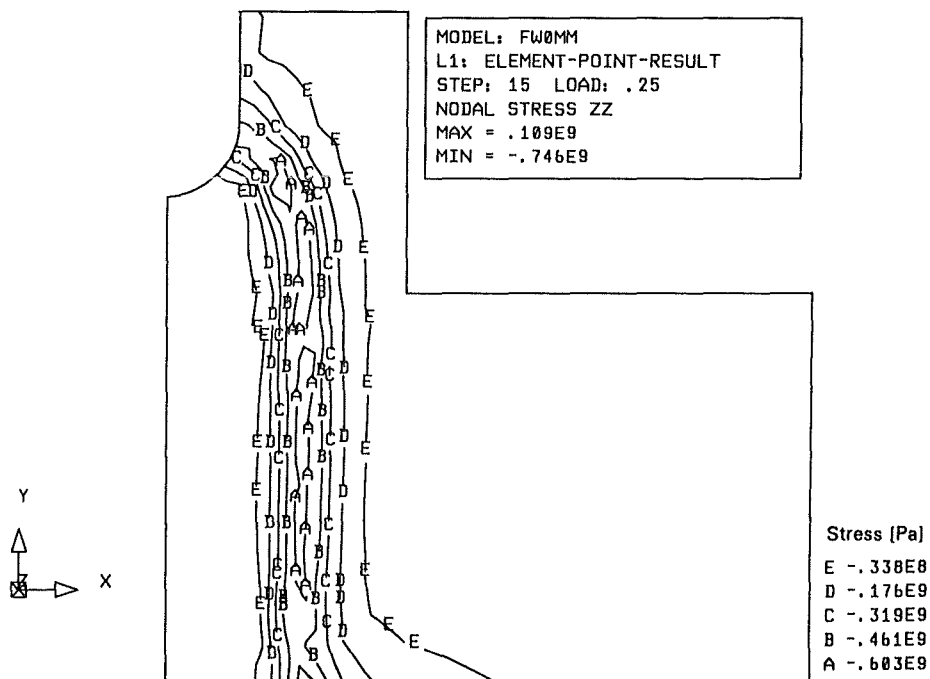


Fig. 3-19 Longitudinal stresses during heating (liquid metal side weld)

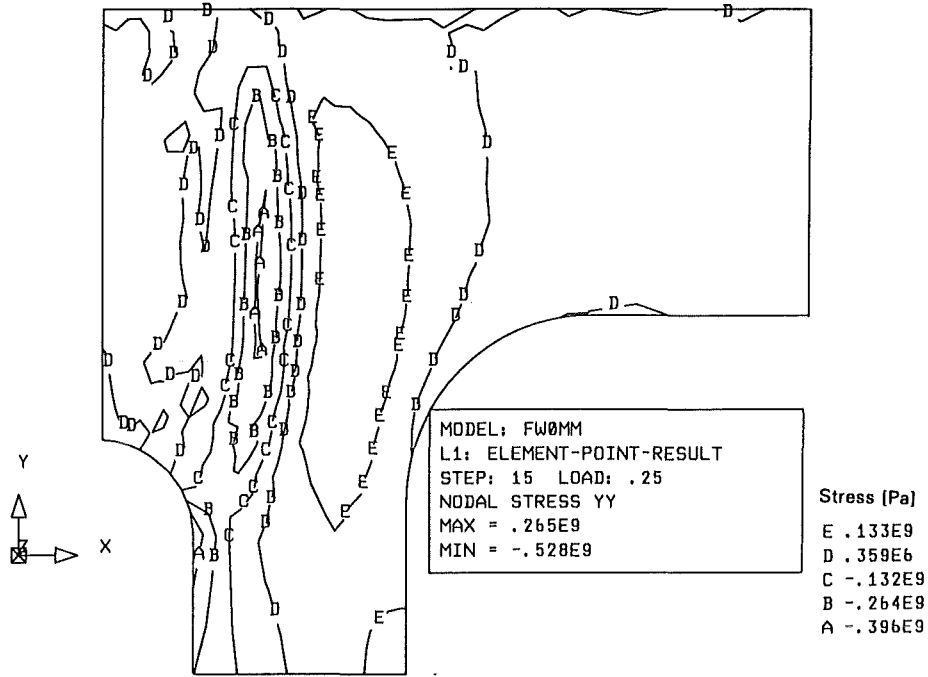


Fig. 3-20 Stresses in y direction during heating (plasma side weld)

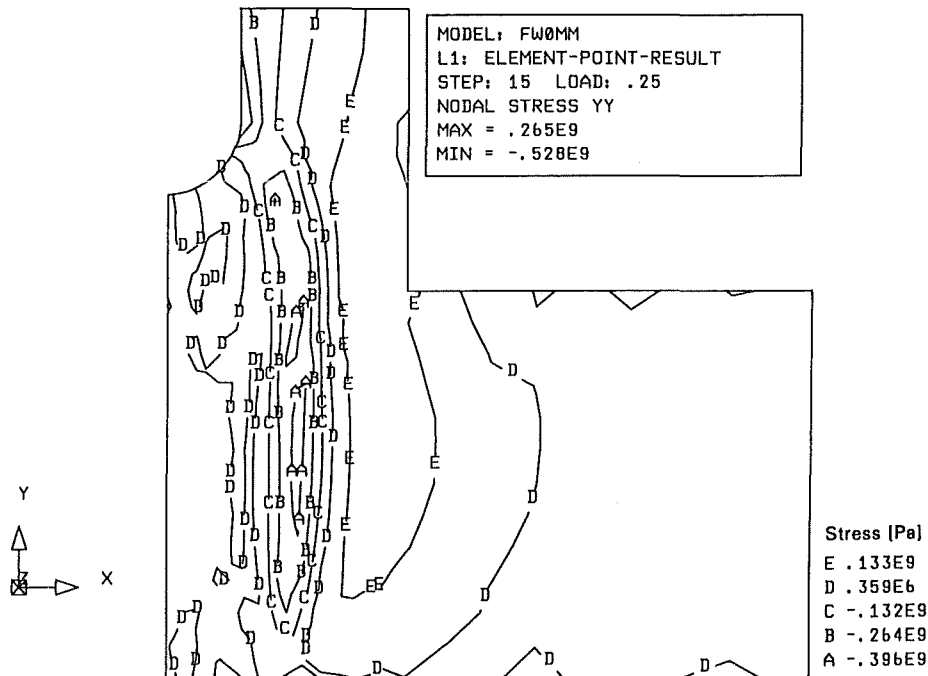


Fig. 3-21 Stresses in y direction during heating (liquid metal side weld)

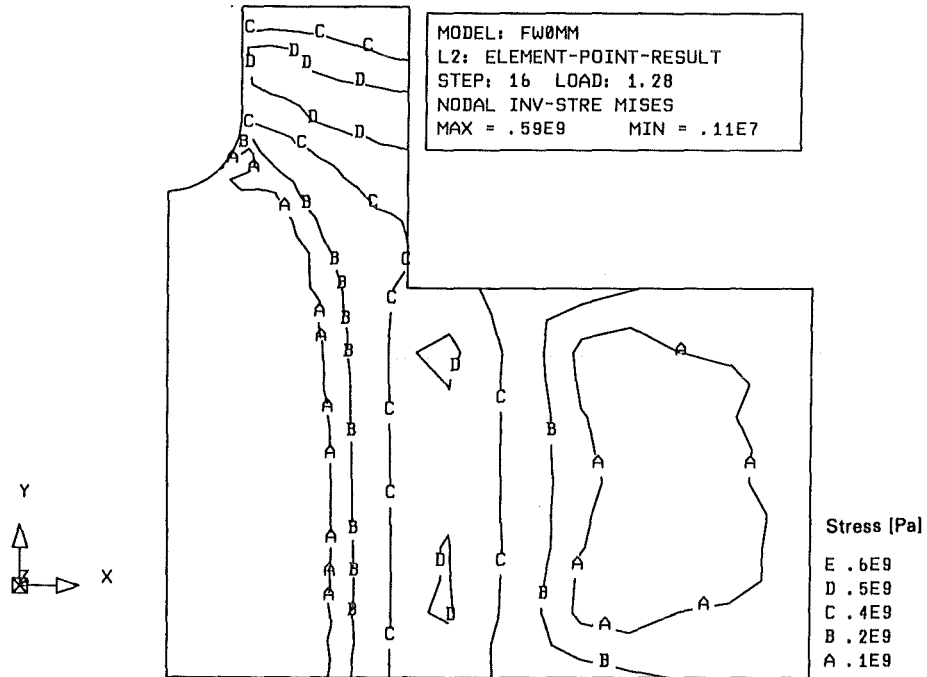


Fig. 3-22 Equivalent stresses (von Mises) during cooling (liquid metal side weld)

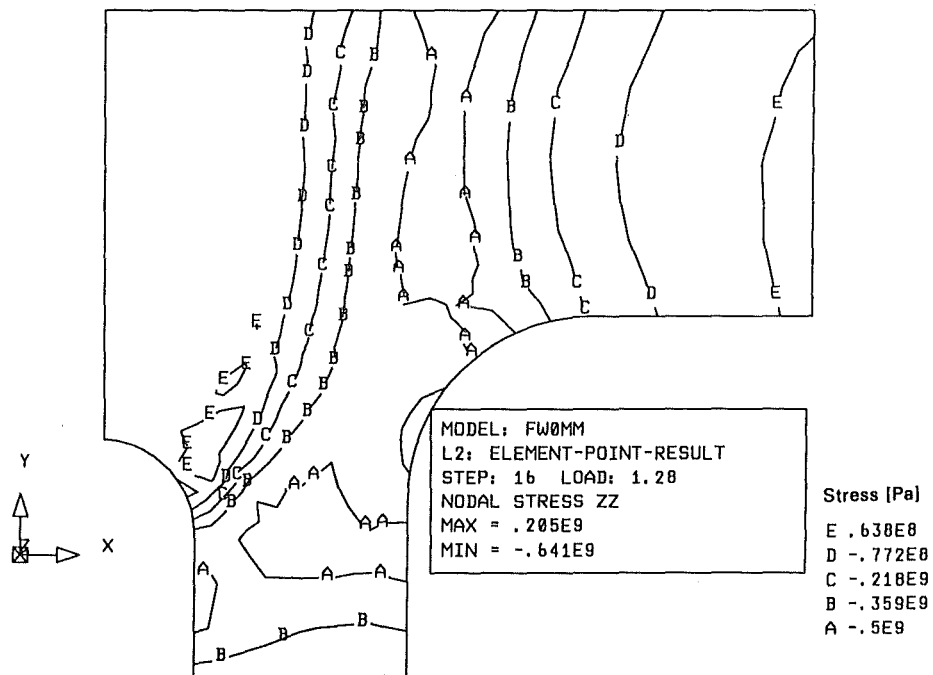


Fig. 3-23 Longitudinal stresses during cooling (plasma side weld)

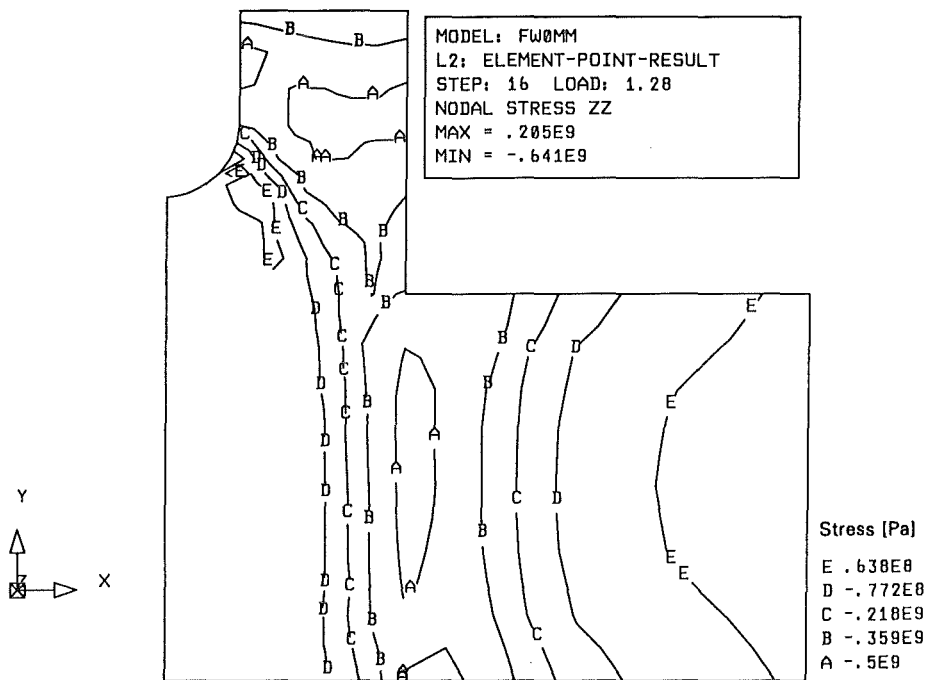


Fig. 3-24 Longitudinal stresses during cooling (liquid metal side weld)

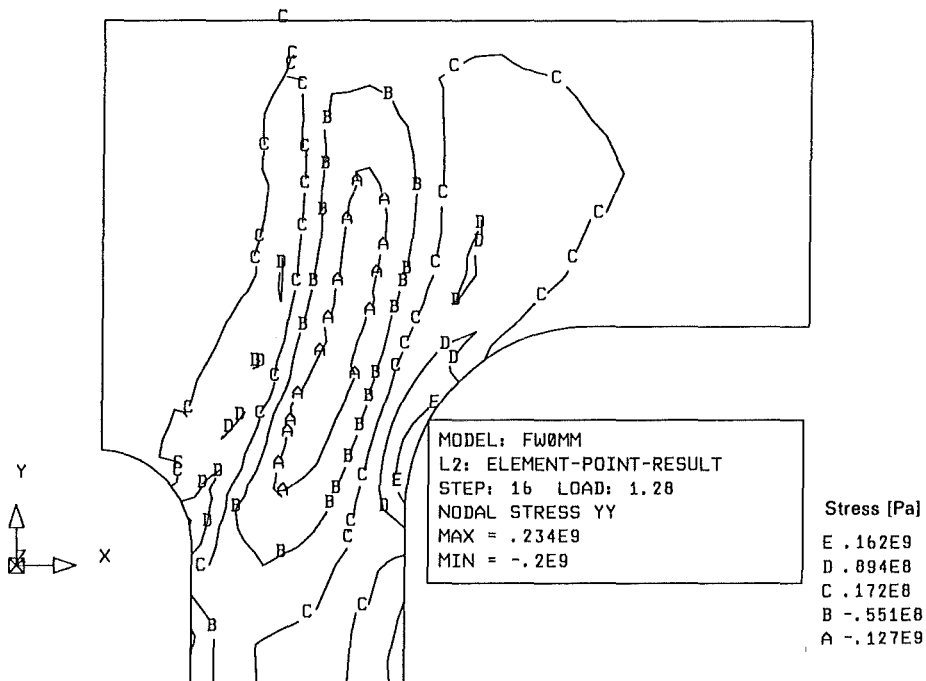


Fig. 3-25 Stresses in y direction during cooling (plasma side weld)

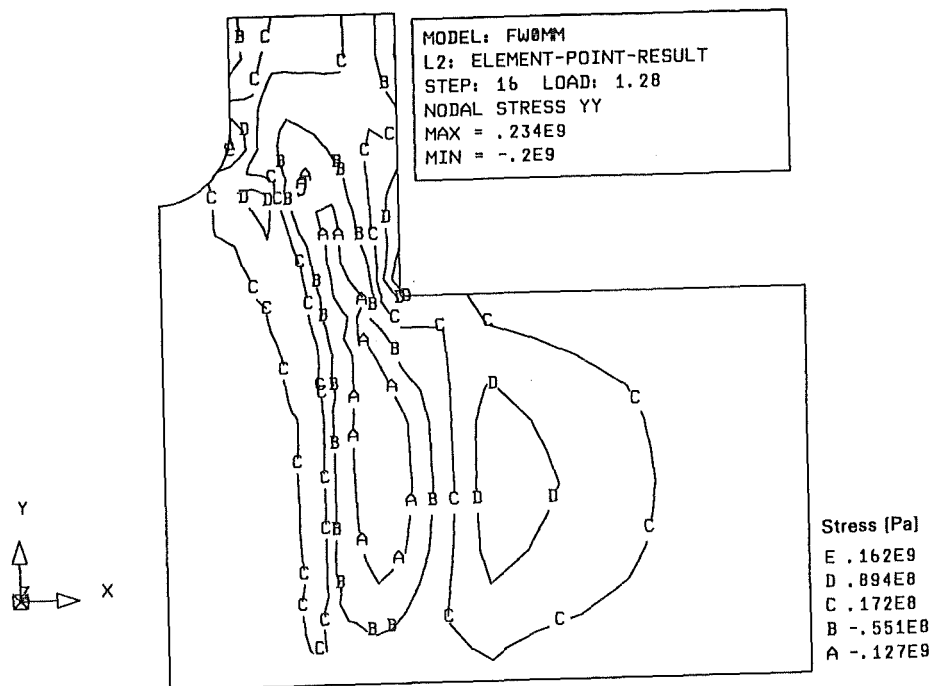


Fig. 3-26 Stresses in y direction during cooling (liquid metal side weld)

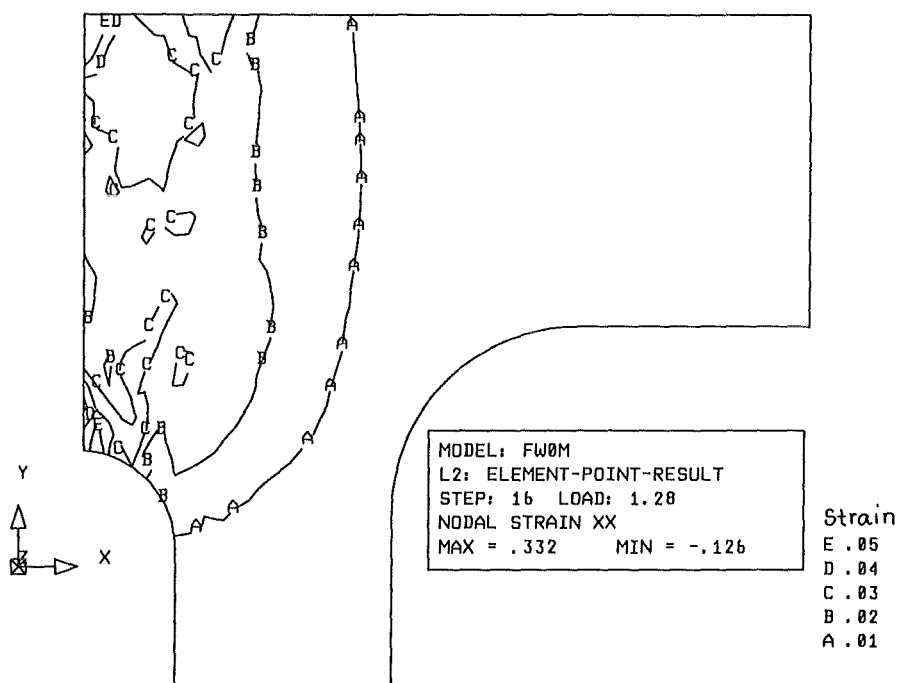
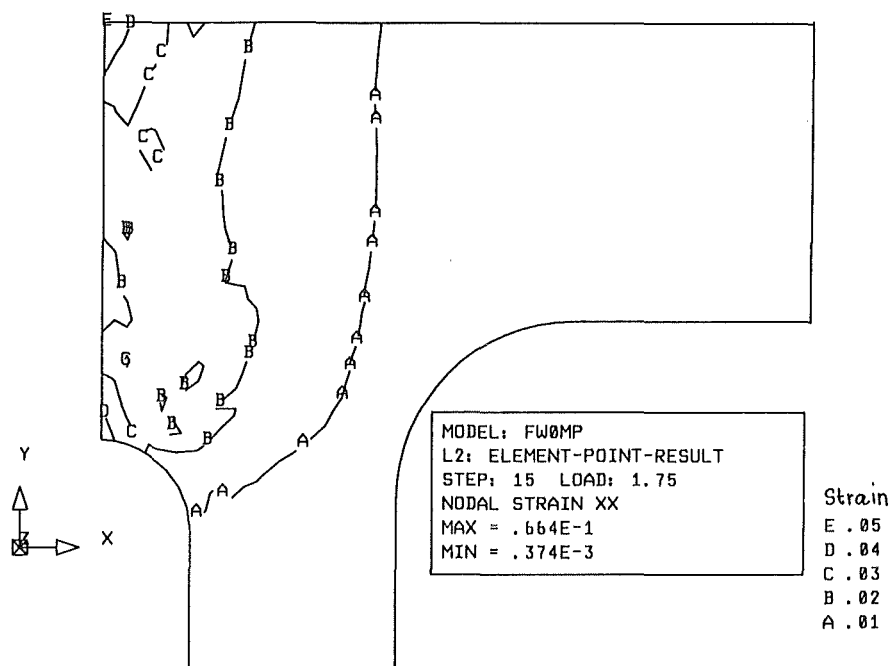


Fig. 3-27 Transverse strains in plasma side weld without preheating



**Fig. 3-28** Transverse strains in plasma side weld with preheating (100°C)

### 3.6 Residual stresses

Longitudinal stresses  $\sigma_{zz}$  are strictly compressive in the region of heat affected zone and tensile elsewhere (see Figs. 3-29 and 3-30). The range of longitudinal residual stresses is rather large (about  $\pm 1000$  MPa), which should be at least partially attributed to the rather crude simulation of volume expansion during the transformation of phases. More sophisticated model is expected to reduce those stresses.

Transverse residual stresses  $\sigma_{xx}$  are those stresses which are responsible for mode I propagation of flaws in the plane of the weld. They tend to be tensile (about 860 MPa) at the ends of both welds (both surfaces of the first wall and both arcs of the leak detection slot, Figs. 3-31 and 32). Also, compressive residual stresses (-500 MPa) are observed. More sophisticated volume expansion simulation may reduce these values. However, the qualitative distribution is judged to remain more or less the same.

A particularly important point is that high tensile residual stresses occur close to the leak detection slot, where rather rough surfaces are to be expected after welding due to difficult access. Both effects together may enhance crack initiation.

The tensile residual stresses in the y direction ( $\sigma_{yy}$ ) are important because they can affect the propagation of flaws which may be present in diffusion welds. As shown in Figs. 3-33 and 3-34, a significant part of the residual stresses is tensile with values up to 770 MPa.

Finally, Figs. 3-35 and 3-36 show the distribution of equivalent (von Mises) residual stress. This values can be used to compare the stress magnitude to the room temperature yield strength value of material concerned. It is clear that the yield strength (614 MPa) is significantly exceeded by the maximum equivalent residual stress (875 MPa). Again, we should note that residual stresses are considered overestimated because of the volume expansion model used.

### **3.6.1 Effect of phase transformations**

The effect of volume expansion during phase transformation is mainly in the fact, that it changes the signs of stresses which are obtained as pure thermal residual stresses. For example (see Figs. 3-37 and 3-38), the pure thermal transverse residual stress is compressive at the surfaces (arcs) and tensile in the middle of the weld. Also, the magnitude of stresses is rather low compared to the estimates obtained accounting for volume expansion.

The effect of phase transformations is recognized as very significant factor contributing to the residual stresses, which is in agreement with observations in literature [2, 30]. Further refinements in modelling are considered to be very important in order to get more reliable estimates of residual stresses.

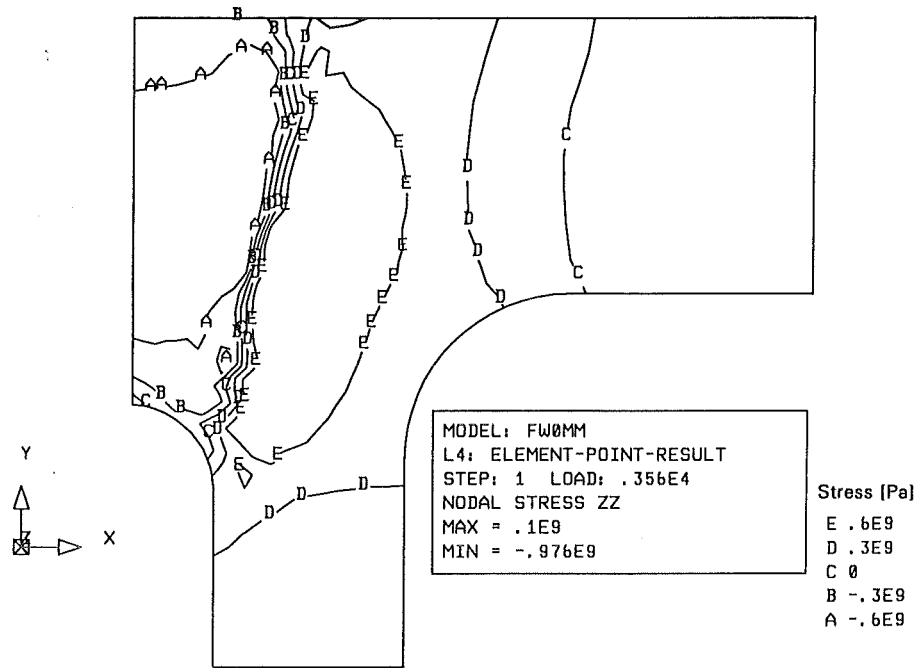


Fig. 3-29 Longitudinal (z) residual stress (plasma side weld)

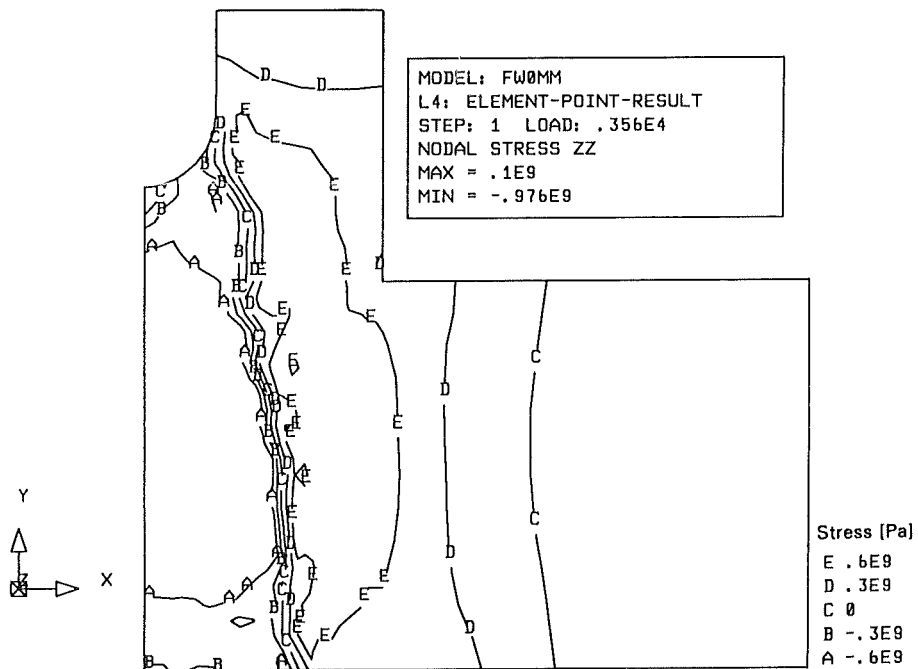


Fig. 3-30 Longitudinal (z) residual stress (liquid metal side weld)

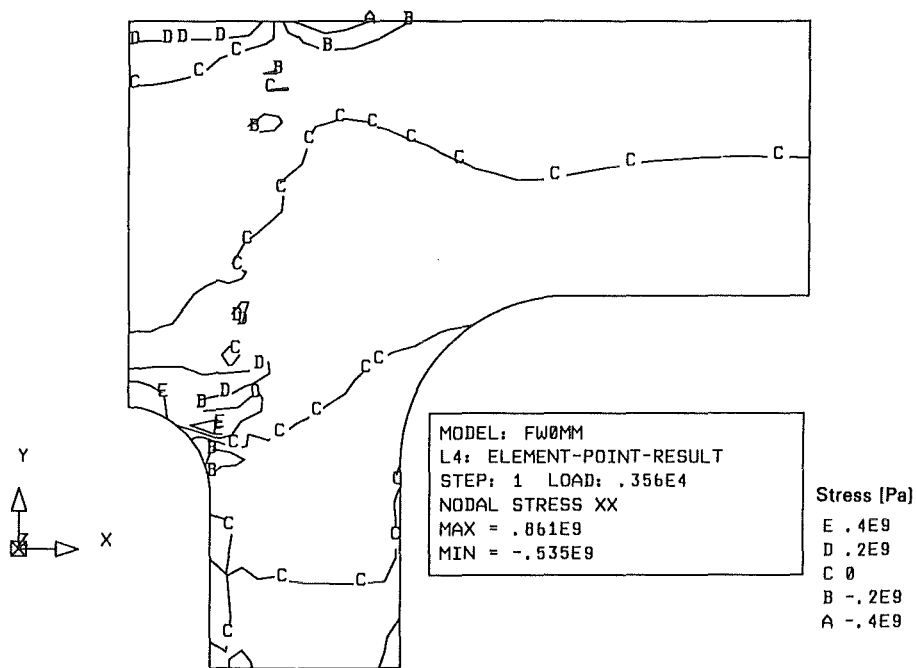


Fig. 3-31 Transverse (x) residual stress (plasma side weld)

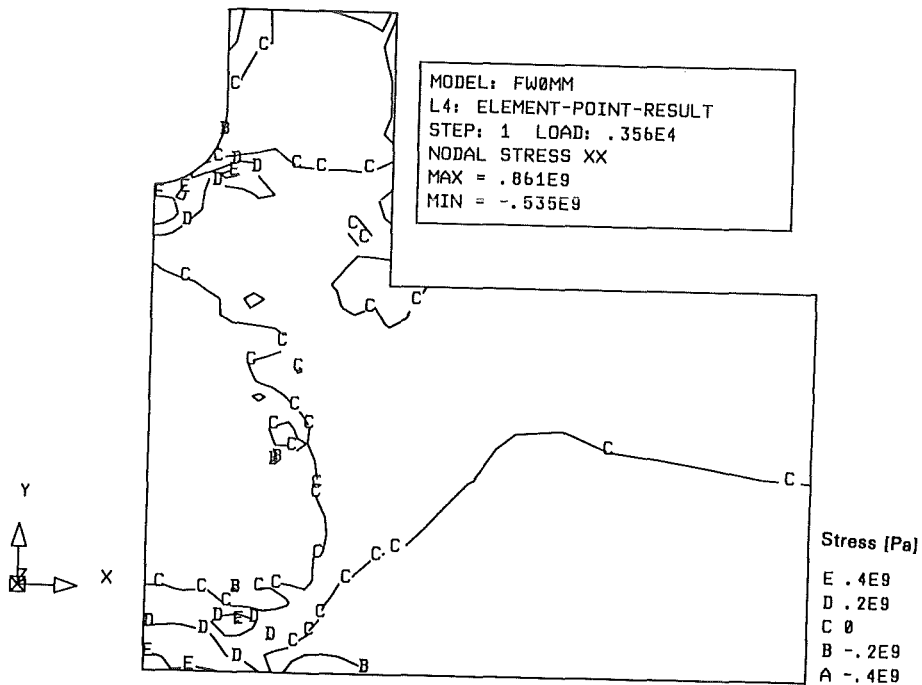


Fig. 3-32 Transverse (x) residual stress (liquid metal side weld)

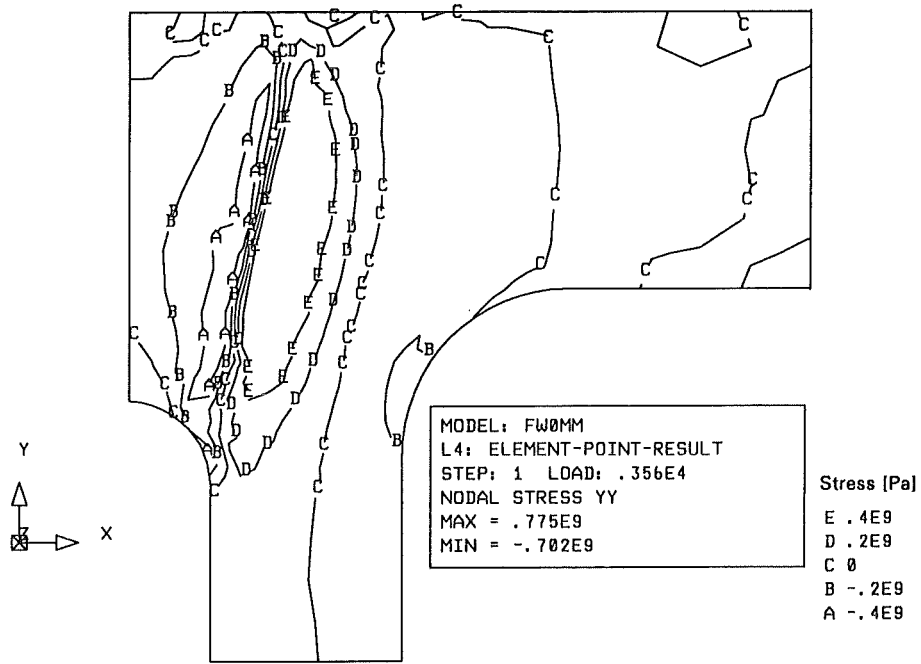


Fig. 3-33 Residual stress in y direction (plasma side weld)

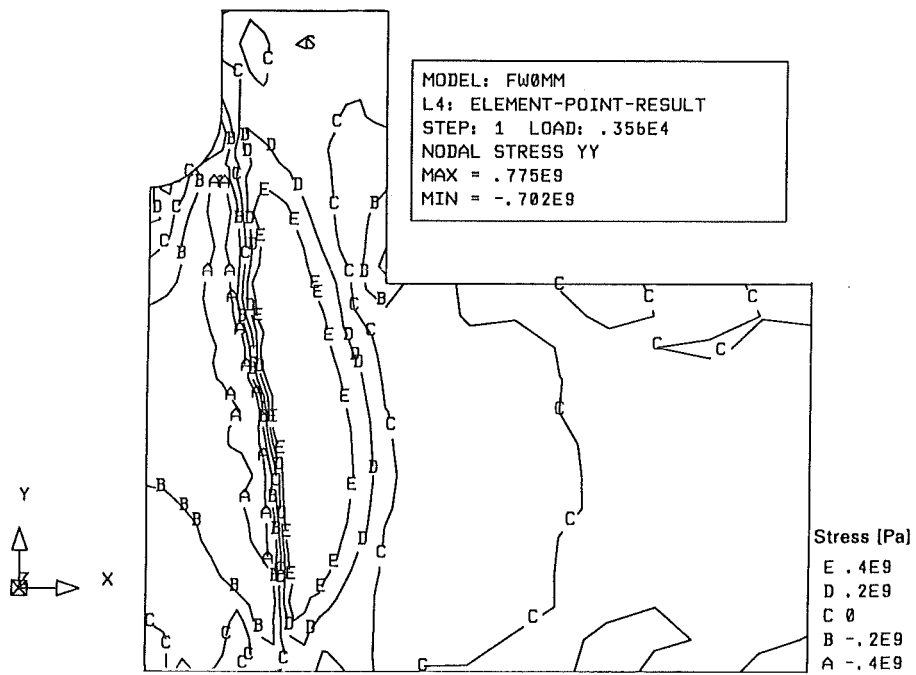


Fig. 3-34 Residual stress in y direction (liquid metal side weld)

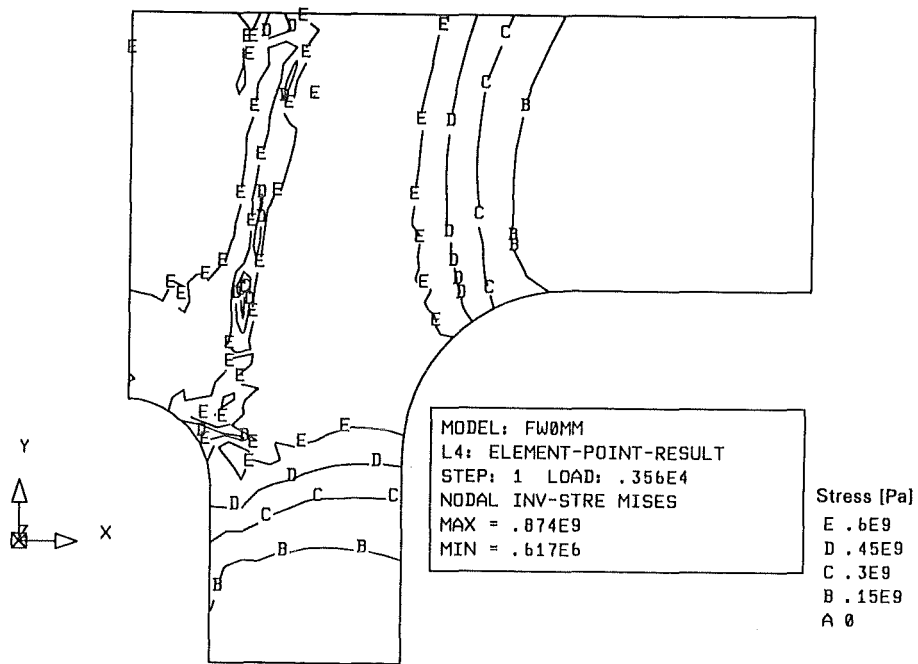


Fig. 3-35 Equivalent (von Mises) residual stress (plasma side weld)

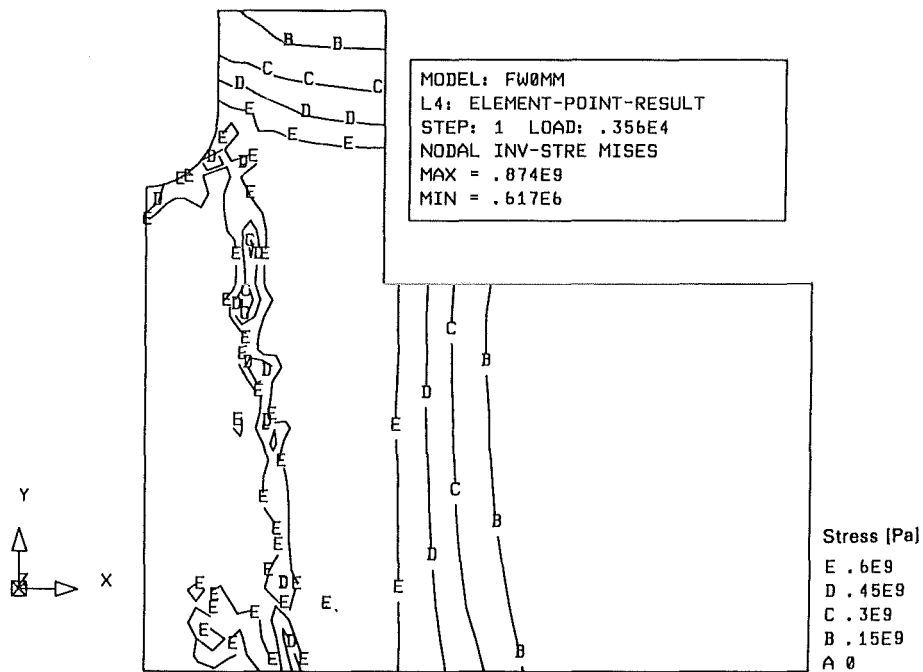


Fig. 3-36 Equivalent (von Mises) residual stress (liquid metal side weld)

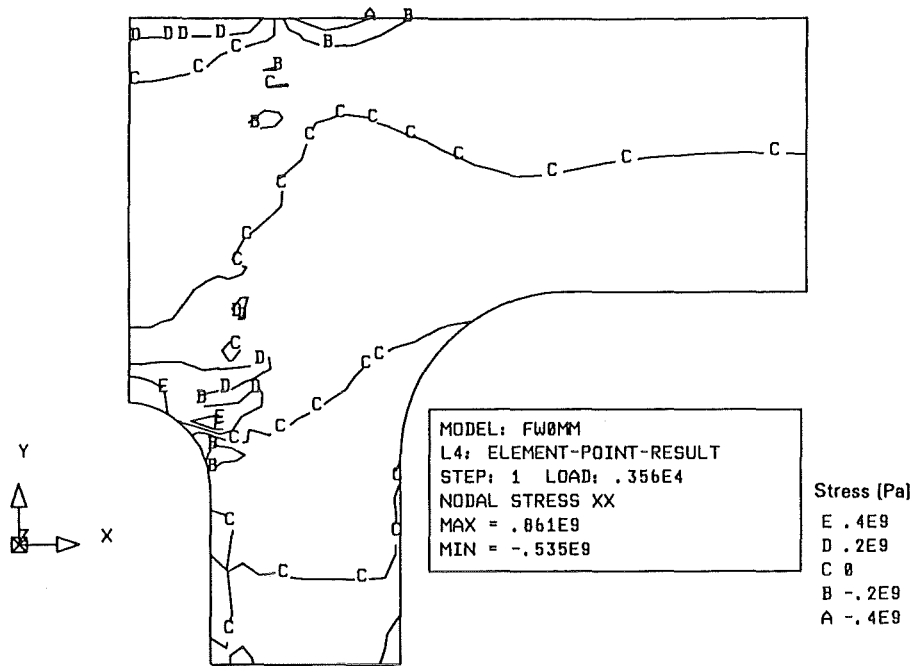


Fig. 3-37 Transverse (x) residual stress without phase transformation (plasma side weld)

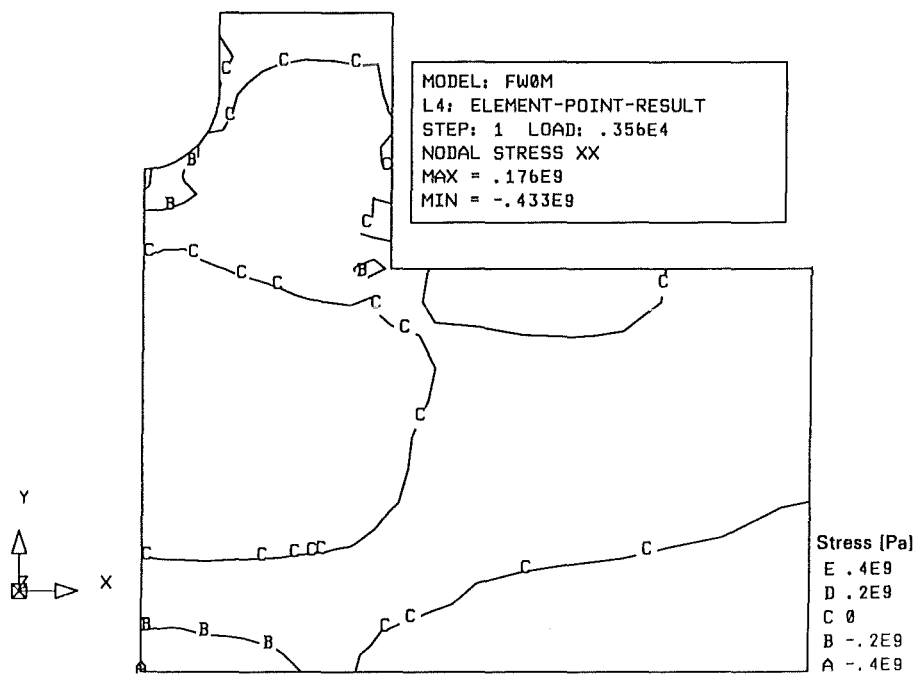


Fig. 3-38 Transverse (x) residual stress without phase transformation (liquid metal side weld)

### 3.7 Heat treatment after welding

The relaxation of the residual stress during the heatup phase of heat treatment is shown in Fig. 3-39. It is represented as a function of temperature, together with the temperature dependent yield strength. Up to about 500°C, the decrease in residual stress can be attributed to the reduction in yield strength while above 500° creep clearly dominates.

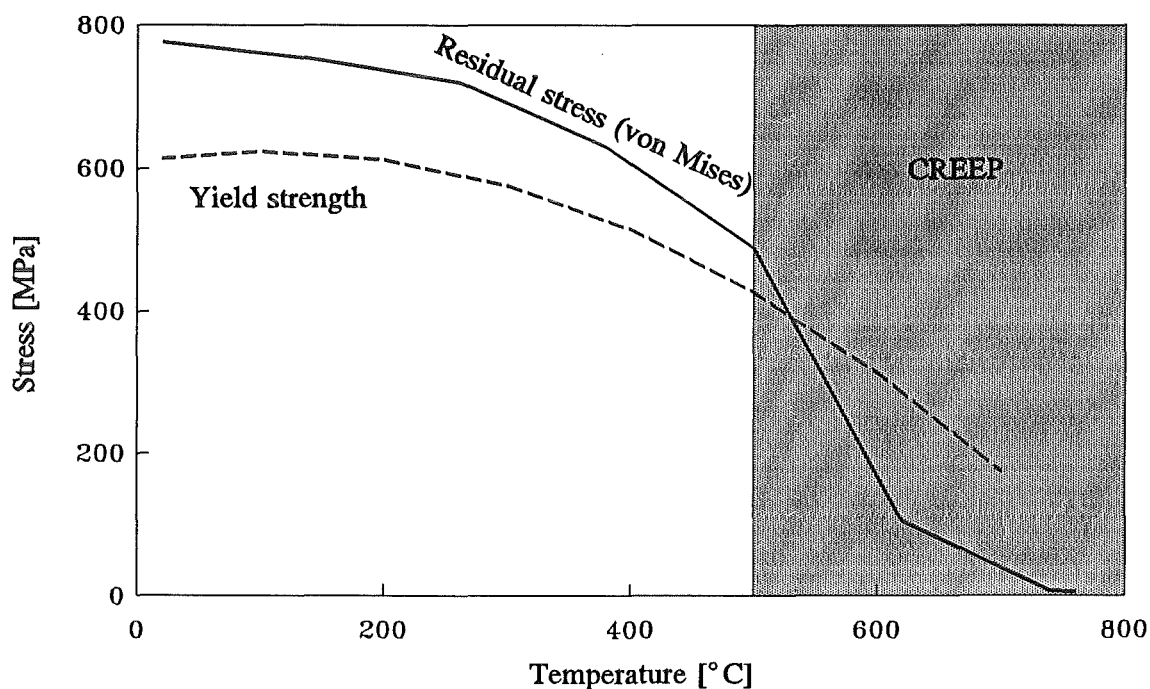


Fig. 3-39 Relaxation of residual stresses by heat treatment

The creep relaxation of residual stresses is finished already during the heating phase. What remains in the vicinity of the weld after the cooling to room temperature is in the order of 10 MPa.

### 3.8 Austenitic stainless steel

No calculations have been performed aiming to determine residual stresses in blanket made of austenitic stainless steel 316 L. However, based on results for a plate geometry given in App. B, some comments are given.

In austenitic stainless steels no phase transformation takes place during the welding. This actually causes the transverse residual stresses to be tensile in the middle of the weld and compressive at the surface. Given the geometry of the double weld analyzed, this would mean compressive residual stresses in the vicinity of the leak detection slot and therefore lower possibility of surface cracks initiating there.

Magnitude of residual stresses in the austenitic steel is significantly lower, which is actually due to lower yield strength value at room temperature.

## 3.9 Summary and possible applications of results

### 3.9.1 Thermal analysis

The temperature distributions obtained in the analysis described above can be used to predict the range of molten material and also the range of heat affected zone, where the post welding properties of the materials usually decrease. For example, using just about one half of the thickness of the wall containing the leak detection slot might cause the heat affected zone to penetrate through the entire wall.

### 3.9.2 Stress analysis

The material data available does not allow to make reliable conclusions about the stress/strain states at temperatures in excess of 700°C. However, a significant reduction in tensile strains during welding is observed during the post-solidification cooling of material when a preheating to 100°C is applied before welding. Such analysis, together with known material behaviour at higher temperatures may be of great value in preventing processes such as solidification cracking.

Residual stress patterns are considered qualitatively good and may be improved by more refined material data. The main result is that transverse residual stresses tend to be tensile on the surfaces when martensitic steel is implemented while austenitic steel generates compressive surface residual stresses. This is important distinction as the surfaces of the leak detection slot can not be improved after the welding.

Heat treatment was shown to reduce the residual stresses to a level of about 10 MPa. Therefore, it is considered as a very important part of the welding procedure.

In cases where post weld heat treatment is not feasible due to the overall dimensions of the blanket (segments), the efficiency of localized heat treatment can be also assessed using similar analyses.

### 3.9.3 Computational efforts

Typical number of increments required to obtain a solution is about 80 for thermal and 250 for stress analysis. In terms of CPU time on IBM 3090 computer, about 20 and 100 minutes are needed to finish the calculation. This includes about 20 increments (about 10 minutes) for creep based analysis of post weld heat treatment.

## 4 CONCLUSIONS

The primary task of research described in this report was to setup a model to analyze the residual stresses in an electron beam welded double weld of a dual coolant liquid metal breeder blanket.

Review of literature on computational weld mechanics showed that there are no published models of electron beam welds. Further, the analysis of models used in the analysis of arc welding processes showed, that the residual stresses in a welded joint can be only obtained by a simulation of the entire thermal cycle including metal melting/solidification (and vaporization/condensation for electron beam welds). Also, micromechanical behaviour of material is important in addition to the thermo-mechanical effects. All these topics were covered in the present analysis to the extent supported by the data available.

The main results are time dependent temperature, stress and strain fields (including residual stresses) which were obtained for a given geometry of the welded joint. Some additional welding parameters like preheating and post weld heat treatment were also addressed.

The results may be used directly to support reliability and life-time studies of blanket structures. On the other hand, they provide useful hints about the feasibility of the geometrical configurations as proposed by different design concepts.

Some possibilities to improve the accuracy of the model by more refined modelling of material behaviour are discussed.

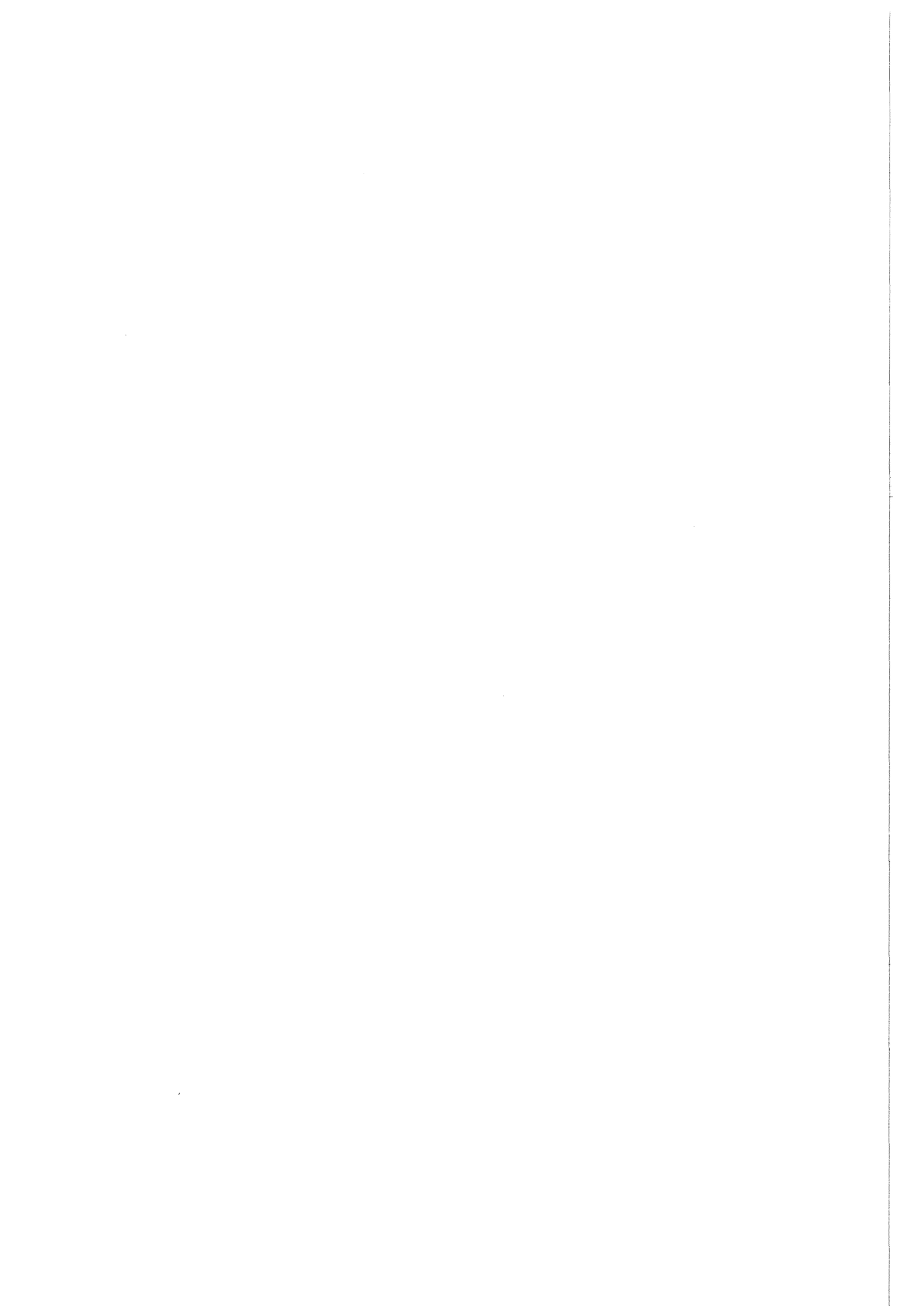
## 5 REFERENCES

- [1] **ABAQUS Users Manual**, Ver. 4.9, Hibbit, Karlsson and Sorrensen, Inc., Providence, Rhode Island, USA.
- [2] Andrieux, S., A.M.Donore, F.Waeckel, *A New Thermo-Metallurgical Model for Welding and Quenching Residual Stresses Computations*, Transactions of 12<sup>th</sup> SMiRT, Stuttgart, Germany (1993), Vol. B, p. 213-224.
- [3] Belà, T., S.Ghia, C.E.Sampietri, *Residual Stress Evaluation: RES Computing System*, Transactions of 10<sup>th</sup> SMiRT, Anaheim, Ca, USA (1989), Vol. B, p. 251-256.
- [4] Bergheau, J.M., D.Pont and J.L.Leblood, *Three-Dimensional Simulation of a Laser Surface Treatment through Steady State Computation in the Heat Source's Comoving Frame*, in L.Karlsson, L.-E.Lingren, M.Jonsson, Eds., **Mechanical Effects in Welding**, IUTAM Symposium, Luleå, Sweden, June 10-14, 1991; Springer Verlag (1992), p. 85-92.
- [5] Boehler GmbH, **Abnahmepruefzeugnis B**, No. 000.190 93.02.32 (1993).
- [6] Brown, S.B., K.Christie, *Three Dimensional Finite Element Modelling of Welded Structures*, in L.Karlsson, L.-E.Lingren, M.Jonsson, Eds., **Mechanical Effects in Welding**, IUTAM Symposium, Luleå, Sweden, June 10-14, 1991; Springer Verlag (1992), p. 181-188.
- [7] Donore, A.M., F.Waeckel, **Influence des transformations structurales dans les lois de comportement élasto-plastiques**, Report Electricite de France No. HI-74/93/024 (1993).
- [8] Easterling, K., **Introduction to the Physical Metallurgy of Welding**, Butterworths (1983).
- [9] Fischer, F.D., *Transformation Plasticity (TRIP) Under Triaxial Stress State*, in L.Karlsson, L.-E.Lingren, M.Jonsson, Eds., **Mechanical Effects in Welding**, IUTAM Symposium, Luleå, Sweden, June 10-14, 1991; Springer Verlag (1992), p. 39-48.
- [10] Fletcher, A.J., **Thermal Stress and Strain Generation in Heat Treatment**, Elsevier Science Publishers (1989).
- [11] Giancarli, L., E.Proust, J.Reimann, K.Schleisiek, Unpublished report (1993), Kernforschungszentrum Karlsruhe, Germany.
- [12] Giancarli, L., E.Proust, J.Reimann, K.Schleisiek, Unpublished report (1993), Kernforschungszentrum Karlsruhe, Germany.
- [13] Goldak, J., A.Oddy, M.Gu, W.Ma, A.Mashaie, E.Hughes, *Coupling Heat Transfer, Microstructure Evolution and Thermal Stress Analysis in Weld Mechanics*, in L.Karlsson, L.-E.Lingren, M.Jonsson, Eds., **Mechanical Effects in Welding**, IUTAM Symposium, Luleå, Sweden, June 10-14, 1991; Springer Verlag (1992), p. 1-30.
- [14] Ho, C.Y. (ed.), **Properties of Selected Ferrous Alloying Elements**, CINDAS Data Series on Material Properties, Vol. III-1 (1989).
- [15] Hwang, J.-R., M.-C.Jeng, C.-C. Wang, *Post Weld Heat Treatment Effects on Fatigue Crack Propagation in an Electron Beam Weldment*, *Fatigue and Fracture of Engineering Materials and Structures* **16** (1993), p. 941-954.
- [16] Inoue, T., *Inelastic Constitutive Relationships and Applications to Some Thermomechanical Processes Involving Phase Transformations*, in R.B.Hetnarski, ed., **Thermal Stresses Vol. 3**, North Holland (1989), p. 191-274.
- [17] John, H., S.Malang, H.Sebening, **DEMO-Relevant Test Blankets for NET/ITER**, Part 1: Self-Cooled Liquid Metal Breeder Blanket, Vol. 2, Report KfK-4908 (1991).

- [18] Karlsson, L., *Thermal Stresses in Welding*, in R.B.Hetnarski, ed., **Thermal Stresses Vol. 1**, North Holland (1986), p. 299-385.
- [19] Kussmaul, K., E.Roos, W.Guth, *A Contribution to the Numerical and Experimental Determination of Residual Stresses in Welds*, Nuclear Engineering and Design **112** (1989), p. 337-348.
- [20] Kühle, M., **Material Data Base for the NET Test Blanket Design Studies**, First Draft (unpublished), Kernforschungszentrum Karlsruhe (1988).
- [21] Lindgren, L.E., A.Carlestam, M.Jonsson, *Computational Model of Flame-Cutting*, Journal of Engineering Materials and Technology ASME **115** (1993), p.440-445.
- [22] Malang, S., J.Reimann, H.Sebening, **DEMO-Relevant Test Blankets for NET/ITER**, Part 1: Self-Cooled Liquid Metal Breeder Blanket, Vol. 1, Report KfK-4907 (1991).
- [23] Malang, S., E.Bojarsky, L.Bühler, H.Deckers, U.Fischer, P.Norajitra, H.Reiser, *Dual Coolant Liquid Metal Breeder Blanket*, in C.Ferro (ed.), **Fusion Technology 1992**, Proc. SOFT 17, Rome, Italy (1992), Vol. 2, p. 1424-1428.
- [24] Marshall, P., **Austenitic Stainless Steels, Microstructure and Mechanical Properties**, Elsevier Applied Science Publishers (1984).
- [25] Masubuchi, K., **Analysis of Welded Structures**, Pergamon Press (1980).
- [26] **Mechanische und physikalische Eigenschaften der Austenitischen Chrom-Nickel-Stähle bei hohen Temperaturen**, International Nickel Deutschland (1965), Düsseldorf, Germany.
- [27] Näsström, M., L.Wikander, L.Karlsson, L.E.Lindgren, *Combined Solid and Shell Element Modelling of Welding*, in L.Karlsson, L.-E.Lingren, M.Jonsson, Eds., **Mechanical Effects in Welding**, IUTAM Symposium, Luleå, Sweden, June 10-14, 1991; Springer Verlag (1992), p. 197-206.
- [28] Nitschke-Pagel, Th., H.Wohlfahrt, *Residual Stress Distributions after Welding as a Consequence of the Combined Effect of Physical, Metallurgical and Mechanical Sources*, in L.Karlsson, L.-E.Lingren, M.Jonsson, Eds., **Mechanical Effects in Welding**, IUTAM Symposium, Luleå, Sweden, June 10-14, 1991; Springer Verlag (1992), p. 123-132.
- [29] Parker, A.P., *Stress Intensity Factors, Crack Profiles and Fatigue Crack Growth Rates in Residual Stress Fields*, in **Residual Stress Effects in Fatigue**, ASTM STP 776, American Society for Testing and Materials (1982), p.13-31.
- [30] Poje, R., **Schweisseigenspannungen in Elektronenstrahl- und Unterpulver-Schweissverbindungen von Stählen bei verschiedenen Blechdicken**, Dissertation (1984), TH Aachen.
- [31] Quigley, M.B.C., *High Power Density Welding*, in J.F.Lancaster (ed.), **Physics of Welding**, 2<sup>nd</sup> Edition (1986), Pergamon Press.
- [32] Roman, V.G., A.E.Elwi, *Analysis of Large-Diameter Fabricated Steel Tubes under Transverse Shear*, Journal of Engineering Mechanics ASCE **115** (1989), p. 2587-2600.
- [33] Ronda, J., O.Mahrenholtz, *Thermal Problems of Welding*, in L.Karlsson, L.-E.Lingren, M.Jonsson, Eds., **Mechanical Effects in Welding**, IUTAM Symposium, Luleå, Sweden, June 10-14, 1991; Springer Verlag (1992), p. 75-84.
- [34] Rybicki, E.F., R.W.Stonesifer, *Computation of Residual Stresses due to Multipass Welds in Piping Systems*, Journal of Pressure Vessel Technology ASME **101** (1979), p.149-154.
- [35] Rybicki, E.F., D.W.Schmueser, R.W.Stonesifer, J.J.Groom, H.W.Mishler, *A Finite-Element Model for Residual Stresses and Deflections in Girth-Butt Welded Pipes*, Journal of Pressure Vessel Technology ASME **100** (1978), p. 256-262.

- [36] Schirra, M.; S.Heger, B.Ritter, M.de las Rivas, A.Chamero, **Untersuchungen zum Zeitstandfestigkeits- und Kriechverhalten am austenitischen Stahl AISI 316 - NET (Abschlußbericht)**, KfK 4861 (1991).
- [37] Schirra, M., S.Heger, H.Meinzer, B.Ritter, W.Schweiger, **Untersuchungen zum Vergütungsverhalten, Umwandlungsverhalten und der mechanischen Eigenschaften am martensitischen Stahl 1.4914 (NET-Charge MANET-1)**, KfK 4561 (1989).
- [38] Swift-Hook, D.T., A.E.F.Gick, *Penetration Welding with Lasers*, Welding Research Supplement (Nov. 1973).
- [39] Terada, H., T.Nakajima, *Analysis of Stress Intensity Factor of a Crack Approaching Welding Bead*, International Journal of Fracture 27 (1985), p. 83-90.
- [40] Tomita, Y., K.Tanabe, K.Koyama, *Improving Toughness of Electron Beam Welds of Heavy Mn-Mo-Ni Steel Plates for Pressure Vessels*, Journal of Pressure Vessel Technology ASME 115 (1993), p.242-248.
- [41] Ueda, Y., M.G.Yuan, *Prediction of Residual Stresses in Butt Welded Plates Using Inherent Strains*, Journal of Engineering Materials and Technology ASME 115 (1993), p.417-423.
- [42] Wegst, C.W., **Stahlschlüssel**, Verlag Stahlschlüssel Wegst GmbH (1986).

# APPENDIX A



## A MATERIAL PROPERTIES

### A.1 General remarks

The main structural materials foreseen to be used for blankets are austenitic stainless steel denoted by AISI 316 L (close to DIN 1.4919) and martensitic stainless steel denoted as MANET (also DIN 1.4914 or X18CrMoVNb121). The test welds described in App. B were however performed using plates made of steel DIN 1.4922 (X20CrMoV121).

#### A.1.1 Dependence on temperature

The main data sources on material properties were used were Kühle [20] for both materials, while some specific data were retrieved from [36] for AISI 316 L and from [37] for MANET. For DIN 1.4922, specification of the manufacturer [5] and Stahlschlüssel 1986 [42] were consulted. These data sources contain data specific for the steels analyzed. However, the range of temperatures reported is essentially limited between 20 and 600°C (in some cases 20 and 1000°C). Extrapolations of material properties at higher temperatures together with underlying assumptions are explained and justified in the subsections below.

In the tables below, the specific data [5, 20 and 42] is highlighted by the shadowed background. Assumed values are printed in *italic*.

The temperatures in excess of austenitisation temperature (about 870°C for MANET [37]) are delineated by a thick line in all subsequent tables. In this range, identical behaviour of all three steels is assumed as they have all reached a similar austenitic structure.

#### A.1.2 Dependence on microstructure

The only information on the transformation behaviour of the martensitic MANET steel are the transformation temperatures and CCT diagram given in [37]. Fortunately, the development of martensitic structure is not very sensitive to the cooling rates, so that a first approximation analysis can be performed (see Sec. A.4.5).

### A.2 Summary of basic constitutive assumptions

The heat transfer in the liquid and vaporized metal is assumed to follow the laws valid for the solid material. From the viewpoint of the stress analysis, it is also assumed that the metal is solid through the entire range of temperatures analyzed.

Further, the material properties depend only on the temperature and **not** on the development of the microstructure. This is due to the limited data presently available.

#### A.2.1 Welding

During the simulation of the welding procedure, a time-independent elastic-plastic material is assumed. This decision was mainly based on the limitations of the data base presented below (Sections A.3, A.4 and A.5). Further, some rather arbitrary extrapolations of the material properties were required to satisfy the requirements of relatively simple time-

independent plasticity models used. Similar simplifications were also made in some recent reports treating arc welding [18, 19, 27].

To incorporate more sophisticated but also more realistic material behaviour through some of the available visco-plastic models [13, 16], additional specific data on material behaviour is required, especially at temperatures exceeding 700°C.

### A.2.2 Heat treatment (annealing)

Two causes for the stress relaxation during the heat treatment are considered in the analysis. First, the stresses redistribute because of decreased yield strength. Second, creep effects become important at temperatures above 600°C.

The time dependent behaviour has been incorporated as Norton's creep law according to the possibilities of ABAQUS code (option CREEP [1]). The available data base is further explained in Section A.5.

## A.3 Mechanical properties

### A.3.1 Chemical composition

Chemical composition is besides thermal and mechanical histories the most important factor which determines the microstructural state of the steel. The chemical composition of steels analyzed is given in Table A.I. In Table A.II, Ni and Cr equivalents calculated from the chemical compositions following empirical relations given in [8] and [24] are given. The Ni and Cr equivalents can be used to determine the volume fractions of the phases which remain in the stainless steel after cooling to ambient temperature. Using Schaeffler diagram [8], the austenitic phase is predicted for AISI 316L steel, while the MANET and 1.4922 steels exhibit martensitic phase.

### A.3.2 Youngs modulus

The specific data for AISI 316 L and MANET is given for temperatures up to 650 and 600°C, respectively (see Table A.III).

In the available literature, no specific data on Youngs modulus exists for steel 1.4922. Therefore, a similar behaviour of martensitic MANET and 1.4922 was assumed. This was based on considerations given in Fletcher [10]: *"Neither the composition nor structure of the low alloy steels has a significant effect on this property except than the austenitic phase possesses a slightly lower value than that of the other structures of the same composition at the same temperature."* This seems to hold also for **high alloy** austenitic 316 L and martensitic MANET (Table A.III) with significantly different chemical compositions.

Another consideration is the extrapolation of the Youngs modulus to higher temperatures. In analyses of welding stresses reviewed by Karlsson [18], its value is assumed to decrease from about 180 GPa at 400°C to about 8 GPa at 1000°C. At temperatures above 1000°C Youngs modulus is assumed to slowly decrease and vanishes above 1600°. In our analysis the vanishing temperature has been set above 4000°C. This was necessary to assure a non-zero

**Table A.I** Chemical composition of steels analyzed

Element	Composition in weight %		
	316 L from [20]	MANET from [20]	DIN 1.4922 from [5]
C	≤ 0.03	0.13	0.23
Si	≤ 0.5	0.37	0.29
Mn	1.6 - 2.0	0.82	0.62
P	≤ 0.035	0.005	0.019
S	≤ 0.025	0.004	0.002
Co	≤ 0.25	0.01	-
Cr	17.0 - 18.0	10.6	11.22
Mo	2.3 - 2.7	0.77	0.91
Ni	12.0 - 12.5	0.87	0.63
V	-	0.22	0.25
Al	-	0.054	-
Cu	≤ 1.0	0.015	-
Nb	-	0.16	-
B	≤ 0.0025	0.0085	-
Zr	-	0.053	-
N	0.06 - 0.08	0.003	≤ 0.035[42]

**Table A.II** Equivalent Ni and Cr contents of steels analyzed

Element equivalent [%]		316 L	MANET	DIN 1.4922
After [8]	Cr equivalent	20.8	11.9	12.6
	Ni equivalent	14.1	5.2	7.8
After [24]	Cr equivalent	22.3	14.2	14.4
	Ni equivalent	16.4	5.3	8.7
Solid state phase at 20°C		Austenite	Martensite	Martensite

**Table A.III** Youngs modulus and Poisson ratio

<i>T</i> Temperature [°C]	<i>E</i> Youngs modulus [GPa]			$\nu$ Poisson ratio [-]		
	316 L	MANET	1.4922	316 L	MANET	1.4922
20	192	217	217	0.3	0.27	0.27
100	186	213	213	0.3	0.28	0.28
200	178	206	206	0.3	0.28	0.28
300	170	199	199	0.3	0.29	0.29
400	161	190	190	0.3	0.29	0.29
500	153	181	181	0.3	0.3	0.3
600	145	171	171	0.3	0.31	0.31
650	141	-	-	0.3	-	-
1000	8			0.45		
1400	4			0.45		
4000	0.01			0.45		

value over the entire range of temperatures (over vaporization temperature) involved in E-beam welding.

### A.3.3 Poisson ratio

The Poisson ratio is given as temperature independent value for 316 L ([20], Table A.III). It is therefore assumed to be constant between 20 and 650°C. The temperature dependency is however known for MANET [20].

Again, no specific data is available for 1.4922. As in case of Youngs modulus the behaviour of MANET is assumed to be fully representative.

Extrapolation to higher temperatures is performed according to the data reported by Karlsson [18], where Poisson ratio tends to 0.5 at melting temperature. Finally, its high temperature value was set to 0.45 which enabled relatively fast convergence of the ABAQUS non-linear algorithms.

### A.3.4 Yield strength

Rather complete data sets are available for all three steels considered up to about 700°C (Table A.IV). However, the actual room temperature yield strength of DIN 1.4922 plates used in the test welding (see [5]) was closer to the value of MANET than to the Stahlschlüssel minimum requirements. Again, no difference between MANET and 1.4922 was assumed.

Extrapolation to the temperatures above was made considering similar behaviour of all three steels and values given by Karlsson [18].

**Table A.IV** Yield strength and hardening coefficient

<i>T</i> Temperature [°C]	$\sigma_y$ Yield strength [MPa]			<i>H</i> Strain hardening coefficient [MPa]		
	316 L	MANET	1.4922	316 L	MANET	1.4922
20	249	614	614	1498	1242	1242
100	212	623	623	1474	980	980
200	178	612	612	1429	727	727
300	156	575	575	1410	675	675
400	143	513	513	1474	515	515
500	136	426	426	1555	279	279
600	131	313	313	1523	142	142
700	124	175	175	1381	67	67
900	30			40		
1000	10			33		
1400	10			20		
4000	1			0		

### A.3.5 Strain hardening coefficient

The strain hardening *H* coefficient was obtained from the yield  $\sigma_y$  (Table A.IV) and ultimate tensile strength  $\sigma_M$  (Table A.V) following the relation:

$$H = \frac{\sigma_M - \sigma_Y}{\epsilon_M} \quad (\text{A-8})$$

where  $\epsilon_M$  represents the *strain at ultimate tensile strength*. The pure elastic strain was considered insignificant.

The ultimate tensile stress and strain are not given for the 1.4922 steel, so the strain temperature dependent hardening coefficient of MANET is assumed to be fully representative.

High temperature values of *H* are assumed following Karlsson [18]. The values tend to vanish for all three steels at temperatures exceeding 900°C.

**Table A.V** Ultimate tensile strength and strain

<i>T</i> Temperature [°C]	$\sigma_M$ Ultimate tensile strength [MPa]			$\epsilon_M$ Rupture strain [%]*		
	316 L	MANET	1.4922	316 L	MANET	1.4922
20	863	773	801	41.00%	12.80%	22.00%
100	713	767	767	34.00%	14.70%	14.70%
200	621	737	737	31.00%	17.20%	17.20%
300	593	681	681	31.00%	15.70%	15.70%
400	600	600	600	31.00%	16.90%	16.90%
500	618	494	494	31.00%	24.40%	24.40%
600	603	362	362	31.00%	34.40%	34.40%
700	483	205	205	26.00%	45.00%	45.00%
900	36			15.00%		
1000	15			15.00%		
1400	13			15.00%		
4000	1			15.00%		

\* no strain hardening for strains exceeding this value. **Rupture is NOT modelled!**

Rupture strain of 15% at high temperature is interpreted in the finite element analysis as maximum strain at which strain hardening occurs. At strain values exceeding this limit, an ideally plastic material is assumed.

## A.4 Physical properties

### A.4.1 Density

The room temperature density reported for AISI 316L is 7963 kg/m<sup>3</sup> [20]. A slight temperature dependence of density observed for MANET [20] has been assumed insignificant. The room temperature value of 7750 kg/m<sup>3</sup> is assumed through the entire temperature range.

### A.4.2 Phase transformations

Generally, the effects of phase transformations in the view of thermal analysis are as follows:

- Latent heat is used (or generated) during phase transformations. This effect is accounted only for the solidus-liquidus transition in this analysis and data are further explained below.

- Volume expansion/shrinking effects are observed. This is accounted for in a rather crude way by the appropriate settings of linear thermal expansion coefficient (see Section A.4.5).
- The material properties are actually a strong function of the microstructural state. This dependence is neglected in this analysis due to the lack of data.

### **AISI 316 L**

There are no solid state phase transformations. The melting temperature is reported to be between 1370 and 1400°C [20]. The latent heat (fusion heat) necessary for the melting is not given. The estimate of 271.6 kJ/kg reported by Ronda and Mahrenholtz [33] is taken as representative. This is in good agreement with the value of 268 kJ/kg obtained by weighted averaging of latent heats of the three main constitutive elements (approx. 70% Fe, 18% Cr and 12% Ni [20] with 247.2, 325.6 and 297.6 kJ/kg, respectively [14]).

Heat of vaporization is approximated by 6.3 MJ/kg which is obtained using weighted averaging of the vaporization heats of main constitutive elements.

### **MANET and DIN 1.4922**

Martensitic structure is dominant at room temperature. During heating, the transformation to austenite is reported to occur between 790 and 870°C [37] (unknown for DIN 1.4922). The latent heat for the solid state transformation is in the order of 80 kJ/kg [7]. During cooling, the austenite to martensite transformation occurs at 310°C for a rather large range of cooling rates [37] (unknown for DIN 1.4922). DIN 1.4922 is assumed to behave in the same manner, pending further data refinements.

Fusion and vaporization heats of AISI 316 L are used for both martensitic steels as a first approximation.

#### **A.4.3 Thermal conductivity**

A complete set of data is available up to 1000°C for 316 L and 600°C for MANET and 1.4922 steels (see Table A-VI). Based on the data available, MANET and 1.4922 are assumed to have identical thermal conductivity.

The values of austenitic 316 L at 900 and 1000°C are slightly lower than those of pure  $\gamma$  iron (28.6 and 31.4 W/mK, respectively [14]) but show similar tendency. The value at 1350°C is therefore set to 34 W/m K as opposed to 36.8 of pure  $\delta$  iron. Somewhat higher conductivity of 50 W/m K for molten steel is assumed to simulate enhanced heat transfer due to the moving particles.

The values averaged over temperatures between 20 and 1400°C are 24.8 and 28.1 W/m<sup>2</sup> K for AISI 316 L and MANET, respectively.

#### **A.4.4 Specific heat**

A complete set of data is available up to 1000°C for 316 L and 600°C for MANET steels (see Table A-VI). Based on the practically identical behaviour of conductivity and thermal expansion (see Table A.VII), MANET and 1.4922 are assumed to have identical thermal conductivity.

**Table A.VI** Thermal conductivity and specific heat

<i>T</i> Temperature [°C]	$\alpha$ Conductivity [W/mK]			$c_p$ Specific heat [J/kg K]		
	316 L	MANET	1.4922	316 L	MANET	1.4922
20	14.57	24.21	24	476.39	446	446
100	15.71	24.68	25	490.55	486	486
200	17.13	25.16	25	508.24	523	523
300	18.56	25.56	26	525.92	563	563
400	19.98	25.9	26	543.61	621	621
500	21.4	26.18	26	561.3	702	702
600	22.83	26.44	27	578.99	805	805
700	24.25	-	-	596.68	850	850
800	25.63	-	-	614.37	850	850
900	27.1	27.1		632.06	632.06	
1000	28.52	28.52		649.75	649.75	
1350	34			660		
1400	50			809		
4000	50			809		

A peak value of 850 J/kg K is assumed for MANET and 1.4922 at intermediate temperatures (700-800°C).

Again, the transformation to austenite is assumed to unify the behaviour of all three steels considered. For the austenitic phase just before melting (1350°C) a value of 660 J/kg K is assumed. For the molten metal, a weighted average of molten Fe, Cr and Ni (316 composition) specific heats taken from [14] is assumed to be representative.

The values averaged over temperatures between 20 and 1400°C are 593 and 663 J/kg K for AISI 316 L and MANET, respectively.

#### A.4.5 Thermal expansion

Complete data sets on linear coefficient of thermal expansion exist for MANET and 1.4922 in the range 20-600°C and for 316 between 20 and 1000°C (see Table A-VII).

AISI 316 L has an austenitic structure regardless of the temperature inside the range analyzed. Both martensitic steels however exhibit at least transformation from martensitic to austenitic structure during heating (volume shrinking) and a reverse transformation during cooling (volume expansion).

**Table A.VII** Thermal expansion coefficient and thermal strain

Temperature [°C]	$\alpha$ Thermal expansion coefficient [ $10^{-6}K^{-1}$ ]			$\epsilon_T$ Thermal strain [%]		
	316 L	MANET	1.4922	316 L	MANET	1.4922
20	16.16	10.11	10.11	0.00%	0.00%	0.00%
100	16.64	10.46	10.50	0.13%	0.08%	0.08%
200	17.09	10.95	11.00	0.31%	0.20%	0.20%
300	17.47	11.45	11.50	0.49%	0.32%	0.32%
400	17.81	11.90	12.00	0.68%	0.45%	0.46%
500	18.13	12.24	12.30	0.87%	0.59%	0.59%
600	18.43	12.40	12.50	1.07%	0.72%	0.73%
700	18.72	12.48	12.48	1.27%	0.85%	0.85%
790		12.83	12.83		0.99%	0.99%
800	18.99	12.70	12.70	1.48%	0.99%	0.99%
870		11.62	11.62		0.99%	0.99%
900	19.25	11.96	11.96	1.69%	1.05%	1.05%
1000	19.51	12.96	12.96	1.91%	1.27%	1.27%
1100	17.70	11.76		1.91%	1.27%	
1200	16.20	10.76		1.91%	1.27%	
1500	12.92	8.58		1.91%	1.27%	
2000	9.66	6.14		1.91%	1.27%	
3000	6.42	4.26		1.91%	1.27%	
4000	4.80	3.19		1.91%	1.27%	

### Heating

The linear thermal expansion coefficient below the austenitisation temperature follows the data for MANET. During the austenitisation (between 790 and 870°C), the thermal strain is kept constant. At temperatures exceeding 870°C, the values of the austenitic 316 assumed to be representative, after appropriate shifting as shown in equations below:

where:

$$\alpha_{\text{MANET}}^*(T) = \frac{\alpha_{316}(T)}{1 + \frac{\Delta\epsilon}{\epsilon_T - \Delta\epsilon}} ; T \geq 870^\circ\text{C} \quad (\text{A-9})$$

$$\epsilon_T = \alpha_{316}(T) \cdot (T - T_0) \quad (\text{A-10})$$

and

$$\Delta\epsilon = (\alpha_{316} - \alpha_{\text{MANET}})_{870^\circ\text{C}} \cdot (870 - 20)^\circ\text{C} \quad (\text{A-11})$$

We should note here that this transformation is not essential for the development of residual stresses, as the yield strength levels are low and no stresses of significant magnitude can develop.

### Cooling

The reverse phase transformation usually takes place at lower temperatures, where the yield strength values are close to the room temperature values. The local volume expansion is therefore obstructed by the adjacent non-expanding material, which causes stresses in the order of yield strength.

The austenite to martensite transformation in stainless steels is observed as volume expansion of about 4% (1.4% uniaxial) [24]. As the first approximation in absence of detailed , several authors used a very simple model. For a certain temperature interval, say 50°C, around the temperature of martensite formation, the linear heat expansion coefficient has been set to a constant value of about  $-7 \cdot 10^{-5} \text{ K}^{-1}$  (for example, [19]) in the case of low alloy steel. This however corresponds to a uniaxial strain of 2.4% which is much more than 1.4% reported by Easterling [8] or about 0.9% for stainless steels reported by Marshall [24]. A fixed value of  $3.6 \cdot 10^{-5} \text{ K}^{-1}$  was therefore assumed in the temperature range between 250 and 310°C which corresponds to the transformation temperatures reported in [37].

In the analysis of welds, the thermal strain is usually assumed to be constant above certain cut-off temperature. Näsström [27] reports the 5% difference in residual stresses obtained by setting cut-off at 900 and 1200°C in case of Inconel-600 (no solid state phase changes!). The values of thermal expansion coefficients above 1000°C (below the thick line in Table A-VII) are therefore adjusted appropriately to yield constant thermal strain which is also given in Table A-VII.

## A.5 Creep properties

Simple Norton creep was assumed as the creep loading is only considered during the post weld heat treatment phase, where the creep time is limited to about 3-4 hours. Norton's law is also supported by the available creep data on steels AISI 316 L and MANET ([36] and [37], respectively). Again, the MANET properties are assumed to be representative also for DIN 1.4922. The material constant for the Norton's strain rate law are given in Tab. A.?, VIII.

For the very limited creep times analyzed, the creep rates at temperatures lower than 600°C can be neglected as they do not contribute to significantly to the stress relaxation. Even for stresses of the yield strength magnitude, the creep rates obtained are in the order of 10<sup>-5</sup>/hour or less.

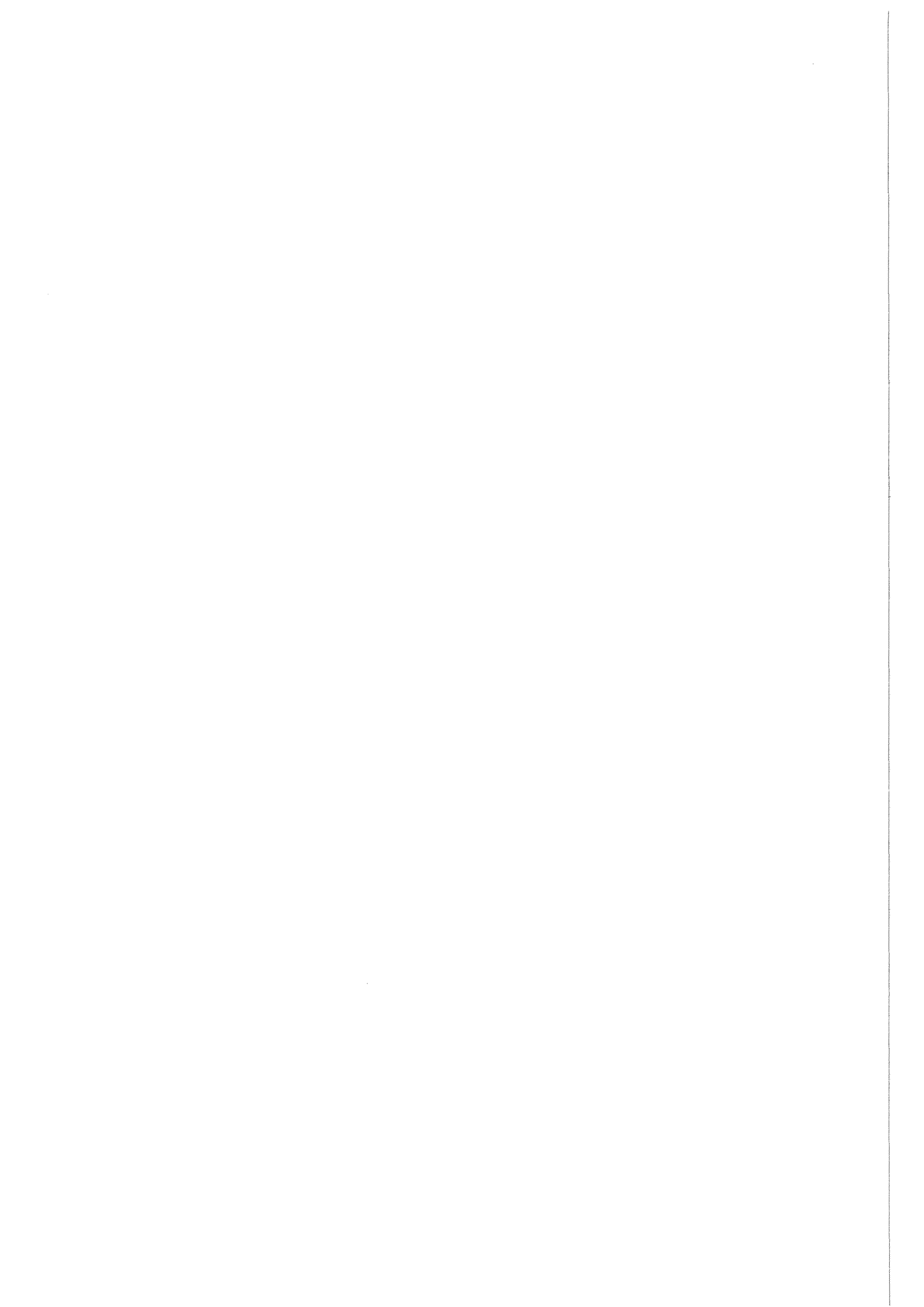
Constants for MANET at 750°C were extrapolated base on the stress-creep strain rate expressions valid at 650 and 700°C. This does not significantly affect the resulting stress field as the majority of stress relaxation takes place before the temperature of 750°C is reached.

**Table A.VIII** Creep properties

Temperature [°C]	Norton's constant		Nortons's exponent	
	316 L	MANET	316 L	MANET
600	$1.4 \cdot 10^{-91}$	$1.0 \cdot 10^{-47}$	10.3	5.1
650	$6.0 \cdot 10^{-83}$	$3.0 \cdot 10^{-42}$	9.5	4.8
700	$1.6 \cdot 10^{-67}$	$2.0 \cdot 10^{-33}$	7.8	3.8
750	$1.0 \cdot 10^{-59}$	$1.6 \cdot 10^{-21}$	7.0	2.4

**Note:** Stress in [Pa], strain rate in [1/h]

# APPENDIX B



## B TEST WELDS IN PLATES

The following reasons lead us to analyze a simple plate geometry before actually start the analysis of the complex geometry of the first wall:

- Two test welds in a plate have been performed by SIEMENS/KWU during the course of this analysis. Although they were not intended to serve as experimental verification of the numerical model, some information obtained can be compared with the numerical predictions.
- Geometrical simplicity of a butt weld in a plate allows for relatively straightforward interpretation of results.
- There is only one report about the residual stresses in electron beam welds considering only butt welded plates [30]. The material used in the experimental analysis (22 MnMoNi 5 5 with yield strength of 460 MPa) is unfortunately considerably different than stainless steels used for blankets. However, due to the similarity of phenomena leading to residual stresses, the experimental results in [30] can be used for qualitative comparisons with predictions of our model.

### B.1 Test procedure

A layout of the test specimen is given in Fig. B-1. It is made of DIN 1.4922 steel (X20 CrMoV 12 1). The properties of this steel are in broad agreement with martensitic MANET (see App. A).

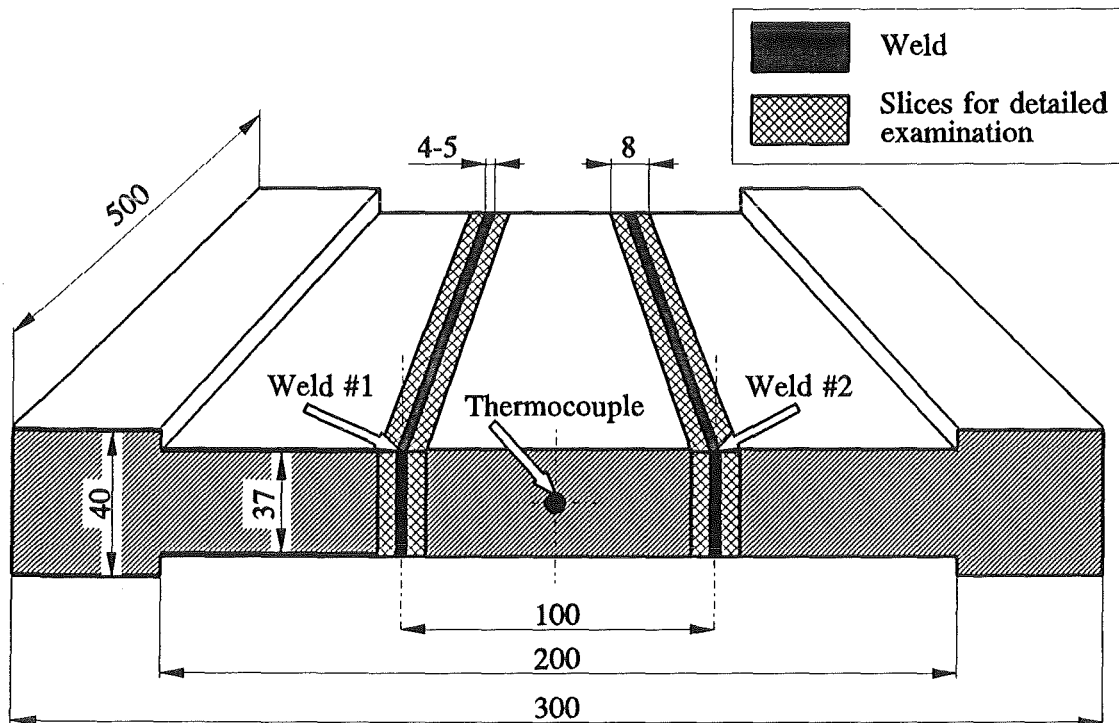


Fig. B-1 Layout of test welds

A plate with thickness of 40 mm has been thinned to 38 mm to obtain appropriate quality of the surface in the vicinity of the welds. A thermocouple has been placed between welds to provide the information about the specimen temperature. Then, two parallel welds have been produced in the plate. The parameters of the welding were as follows:

- Beam current: 130 mA
- Beam voltage: 150 kV
- Beam velocity: 4 mm/sec
- Beam amplitude: 0.8 mm (amplitude of beam oscillatory motion along the weld)

The width of the welds obtained was between 4 and 5 mm with nearly parallel fusion lines.

The temperature history as obtained from the thermocouple is shown in Fig. B-2 together with the heat treatment cycle performed. The welding part of the thermal cycle consisted of welding weld #1 (between 0 and 2 minutes) and weld #2 (between 12 and 14 minutes). So weld #2 was performed in a workpiece preheated to approx. 90°C.

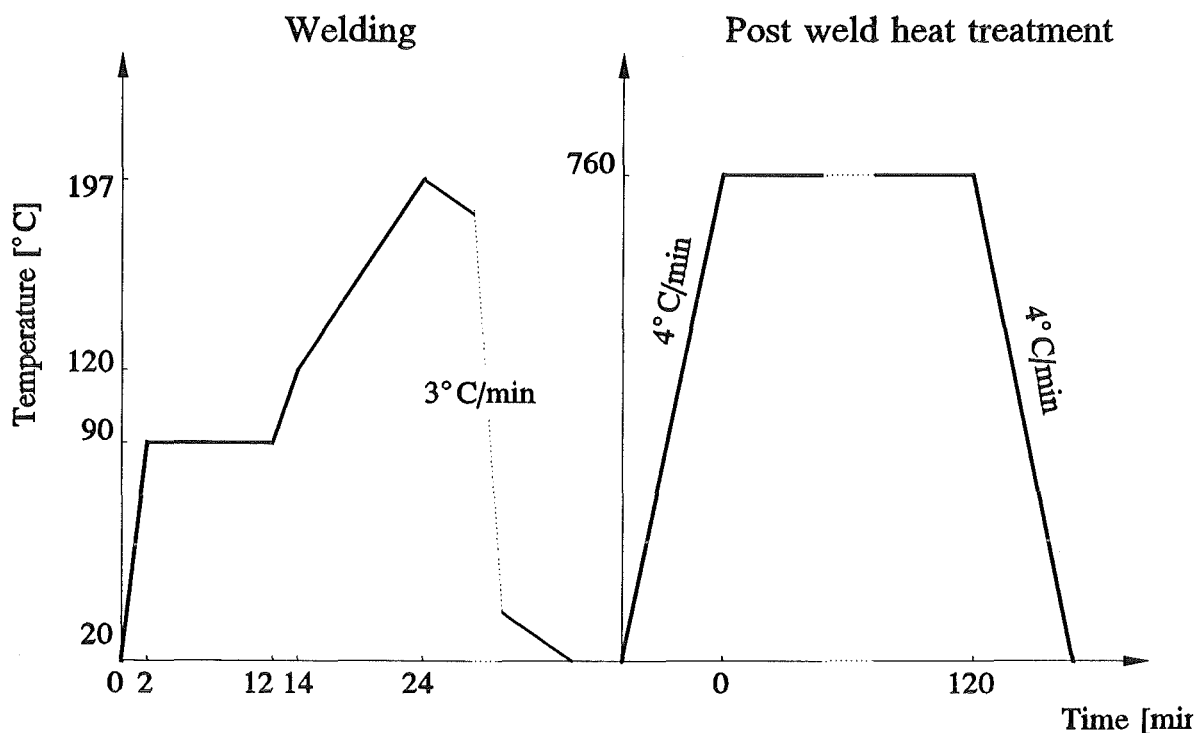


**Fig. B-2** Temperatures during welding and heat treatment as recorded by the thermocouple

After the heat treatment, both welds were cut out of the plate (see Fig. B-1) in the slices of 8 mm in thickness. Ultrasonic and X-ray inspection revealed significant number of small indications in weld #1, while no indications were discovered in weld #2. Indications were not confirmed by a destructive examination which followed.

## B.2 Modelling

### B.2.1 Basic assumptions

The assumptions given in Sect. 3.1 are also applicable here.

### B.2.2 Finite element meshes

Finite element meshes used in the analysis are given in Figs. B-3 and B-4. Two symmetry planes are employed in both meshes. The first is defined by the plane of the weld while the second assumes identical heat transfer on both plate surfaces.

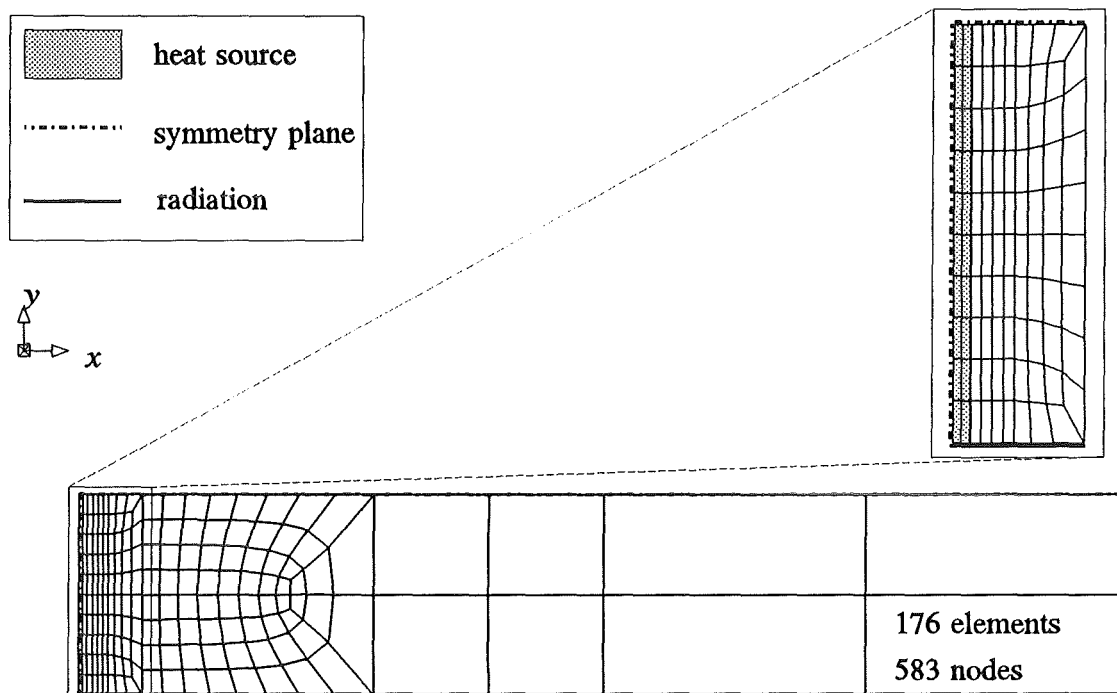


Fig. B-3 Coarse finite element model of the test weld in a plate

Elements used are DC2D8 in thermal and CPGE10RH in stress analysis. Thus, generalized plane strain conditions have been assumed in the stress analysis. The thickness of the layer analyzed is 1 mm in both cases. A 20 cm wide section of plate is analyzed (10 cm remain in the model due to a symmetry over the plane of weld).

Boundary condition assumed during the thermal analysis is heat radiation (emissivity of 0.5).

### B.2.3 Thermal loading

The volume affected by the electron beam is assumed to be defined by the plate thickness, two electron beam oscillation amplitudes and the thickness of the layer analyzed (1 mm). Then, the beam power is assumed to be 19 kW, which is obtained from the product of its current and voltage. Further, 95% of the beam energy is assumed to be transferred to the metal.

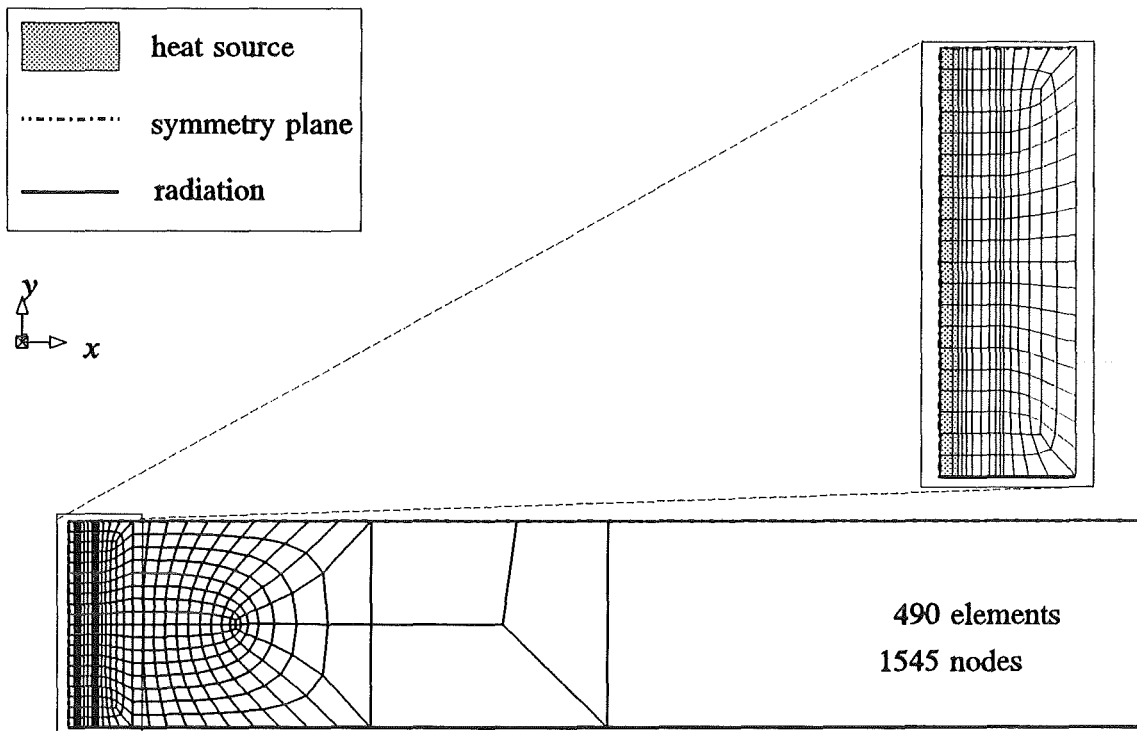


**Fig. B-4** Fine finite element model of the test weld in a plate

Such assumptions would lead to the body heat sources with the density of  $2.96 \cdot 10^{11} \text{ W/m}^3$  which caused excessive widths of the weld. It turned out that about half of this power density produces the expected melting width of about 4 mm, so the power density used in the model was set to  $1.48 \cdot 10^{11} \text{ W/m}^3$  yielding expected weld width.

This can be to some extent explained by the application of Swift-Hook's [38] formulas (eqs. (5) and (6)) which leads to the following (averaged material properties needed are given in App. A):

- normalized melting width (left side of eq. (5)) equals 2.94;
- normalized input power (right side of eq. (5)) equals 12.04;
- ratio between them which represents the fraction of total beam power used for melting equals 0.244 (theoretical maximum is 0.48).

This indicates, that the welding procedure with given parameters operates at about half of its maximum possible efficiency. Also, it is not clear how efficient is the energy transfer from the electron beam to the workpiece. Swift-Hook [38] indeed reports of efficiencies in excess of 85%, but majority of data points considered were obtained at melting ratios significantly higher than 24% and no comment is made about the difference between straight and oscillating movement of electron beam.

The calculations were therefore performed using the power density of  $1.48 \cdot 10^{11} \text{ W/m}^3$ , which assumes that efficiency of the heat transfer between electron beam and the workpiece is about 50%. Using larger power densities would result in larger weld widths and longer cooling times (e.g.,  $t_{8/5}$  would increase) and also in smaller temperature gradients during the cooling of the weld. So the stresses obtained are considered conservative. However, possible future

implementations of time-dependent plasticity models would require more accurate estimates of times in the temperature fields than achieved by this analysis.

Heat source was turned on for the 0.25 sec at the beginning of the analysis. This corresponds to the time needed by electron beam travelling by 4 mm/s to pass a 1 mm thick layer of material.

#### **B.2.4 Material model**

Material models and data used are explained in Section 3.3 and App. A. Both austenitic and martensitic materials were considered in the analysis of the plate.

### **B.3 Results of thermal analysis**

Time histories of temperatures in the vicinity of the weld are given in Figs. B-5 and B-6 for martensitic steel and in Fig. B-7 for austenitic steel. The action of the heat source during the first 0.25 sec is clearly seen on all figures. The qualitative development of the temperatures during the cooling is identical with clear plateau of temperatures during solidification.

The austenitic material has lower thermal conductivity, which is causing slightly slower cooling of the workpiece (Fig. B-7).

Both meshes with martensitic material yielded practically identical temperature fields (difference is less than 1%). Only the results of the coarse mesh are therefore presented below.

The melting temperature reaches the distance of about 2 mm in both materials. This yields the total width of the weld of 4 mm, which was set as a target value.

The cooling times from 800 to 500°C are predicted as follows:

9.2 sec for martensitic material (comparable to 8.7 reported by Poje [30] for a plate with thickness of 40 mm )  
11 sec for austenitic steel.

Uniform temperature field is reached in about 1 hour at 84°C for austenitic steel (lower specific heat), 93°C for martensitic steel without preheating and 135°C for martensitic steel preheated to 90°C.

#### **B.3.1 Comparison with measured temperatures**

The measurements recorded by a thermocouple are shown in Fig. B-2. The workpiece without preheating reached temperature of 90° during the first 2 minutes (88° predicted by the model) and remained constant during the 10 minutes long break between two welds (98° predicted by the model). Then, the second weld was made rising the temperature to 120° during the welding period of 2 minutes (135°C predicted). 10 minutes after the welding was finished, the recorded temperature was 197°C (predicted 160°C).

A statement about the accuracy of the measurements is not available, so the agreement is considered satisfactory. It can be however improved by refining data on boundary condition, which should take place when experimental data with known accuracy is available.

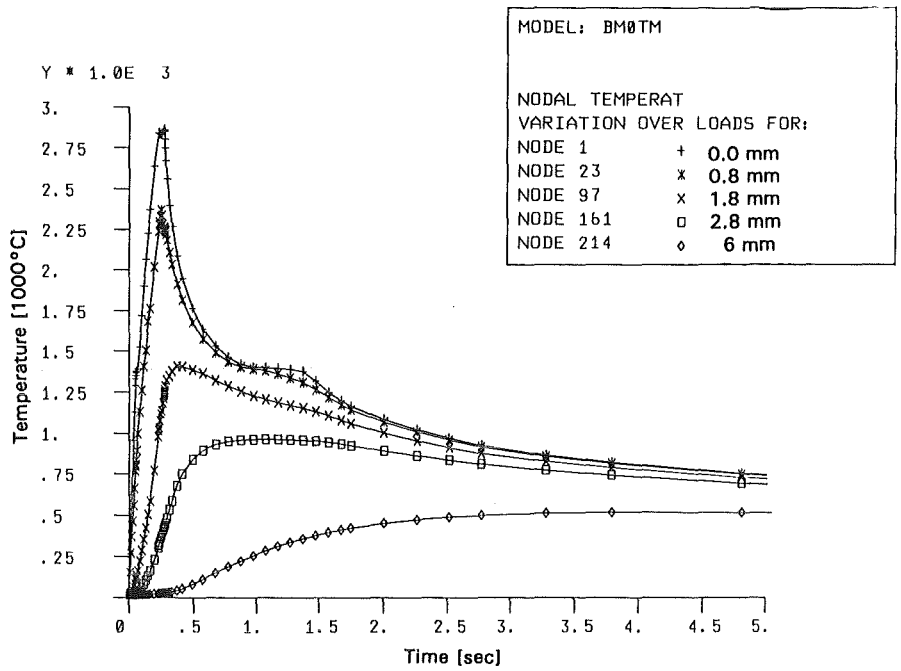


Fig. B-5 Time history of temperatures in the vicinity of weld (martensitic, coarse mesh)

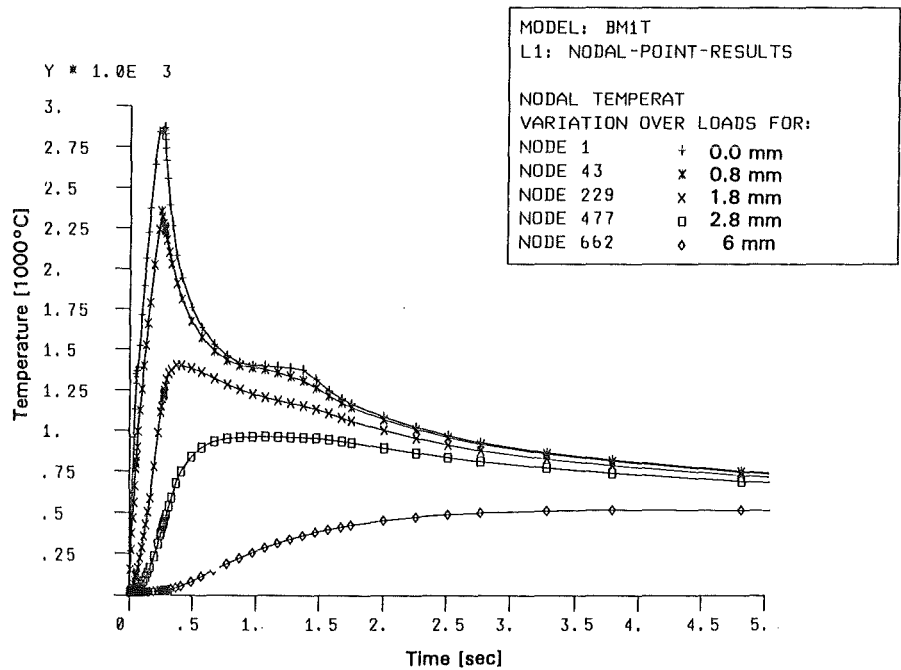


Fig. B-6 Time history of temperatures in the vicinity of weld (martensitic, fine mesh)

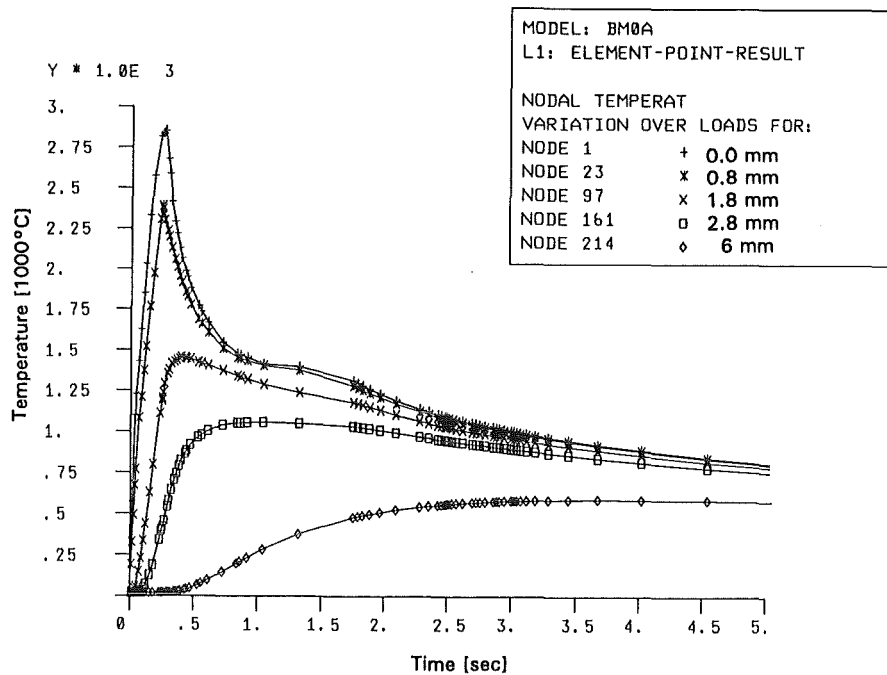


Fig. B-7 Time history of temperatures in the vicinity of weld (austenitic, coarse mesh)

#### B.4 Results of stress analysis

The development of stresses during the welding process is represented in Figs. B-8, B-9, B-10 and B-11. The phase transformations are neglected here to enable direct comparison between austenitic and martensitic steel. During the heating period ( $< 0.25$  sec) a typical observation is that there is actually no stress in the vicinity of the weld. This range has a typical width of 2-3 mm, regardless of the material. During the cooling period, the stresses tend to increase and the differences in material and location become more pronounced. At the residual stress level, this leads to two general conclusions: (1) residual stresses are larger in the middle plane of the plate, which can be attributed to more severe restraints than on the surface, and (2) residual stresses in austenitic material are about half of what is found in martensitic steels.

Residual stresses seem to be the most severe stress level obtained during the welding heat cycle.

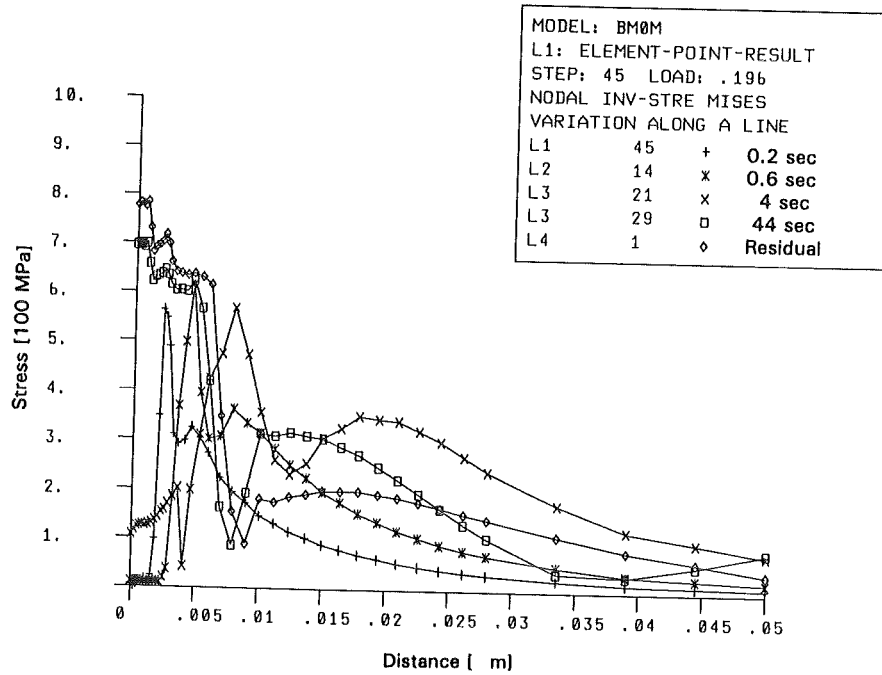


Fig. B-8 Development of equivalent (von Mises) stress (martensitic material, middle plane)

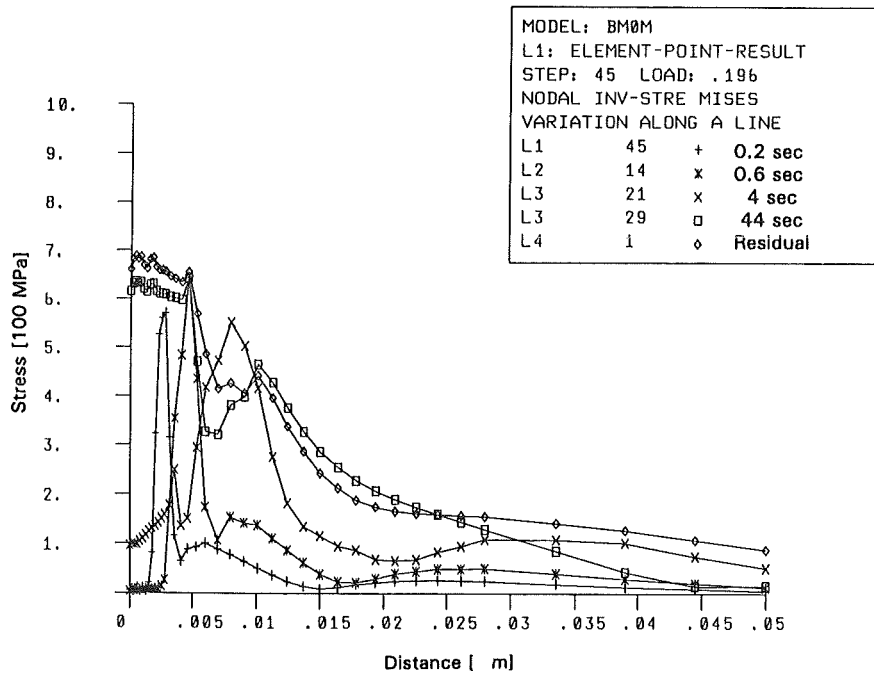


Fig. B-9 Development of equivalent (von Mises) stress (martensitic material, surface)

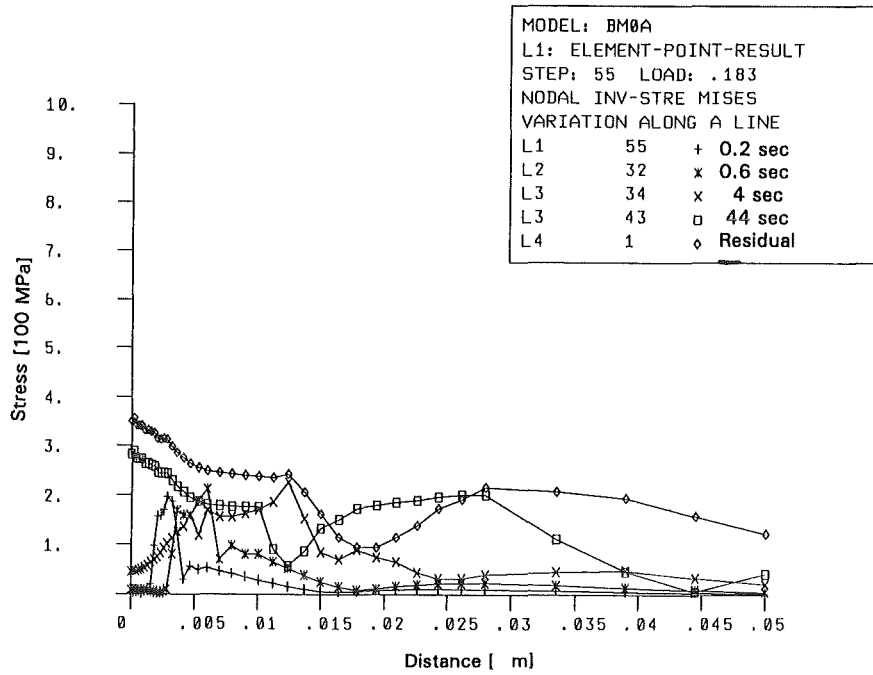


Fig. B-10 Development of equivalent (von Mises) stress (austenitic material, middle plane)

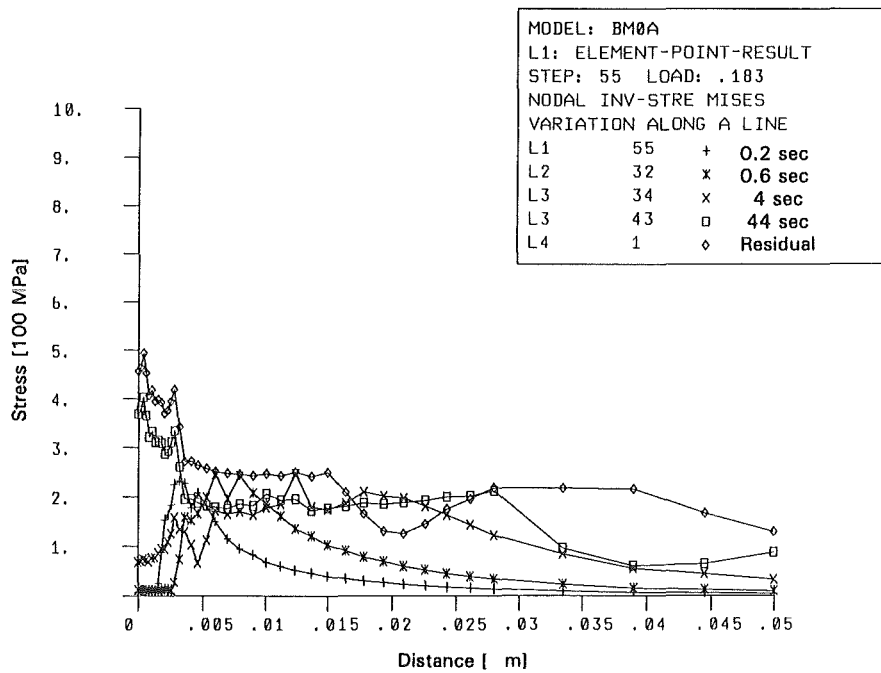


Fig. B-11 Development of equivalent (von Mises) stress (austenitic material, surface)

#### **B.4.1 Residual stresses**

Residual stresses in the austenitic steel have pure thermal origin. The transverse and longitudinal residual stresses are shown in Figs. B-12, B-13, B-14 and B-15. The transverse residual stress in the vicinity of the weld changes the sign from tensile in the middle of the plate (Fig. B-12) to compressive at the surface (Fig. B-13). Longitudinal residual stress does not change the sign, but considerably decreases its magnitude while approaching the plate surface (compare Figs. B-14 and B-15).

In the martensitic plate, essentially identical distributions of residual stresses develop but at significant higher magnitude (Figs. B-16, B-17, B-18 and B-19). The gain in magnitude can be attributed to the significantly higher yield stress value at room temperature, which is exhibited by martensitic steel. The only qualitative difference is that longitudinal distribution at the surface of a martensitic plate tends to vanish (Fig. B-19) which is not the case in the austenitic plate (Fig. B-15).

Martensitic plate with austenite to martensite phase transformation accounted for exhibits totally different residual stress distributions (Figs. B-20, B-21, B-22 and B-23). The most severe consequence induced by the volume expansion is that the transverse residual stresses at the plate surface becomes highly tensile (compare Figs. B-21 and B-17).

Significant volume expansion which takes place in the vicinity of the weld, tends to reduce longitudinal residual stresses inside the heat affected zone. The oscillations in the stresses are due to a rather crude way of modelling the volume expansion which inserts a sudden discontinuity at the border of the heat affected zone (say 4 mm from the weld center line). However, typical W and M shapes of the residual stress distributions as reported by Poje [30] can be recognized.

Based on above results, the results of the model are considered qualitatively adequate. A quantitative comparison is unfortunately not possible due to lack of data on both experimentally determined residual stresses and material behaviour at higher temperatures.

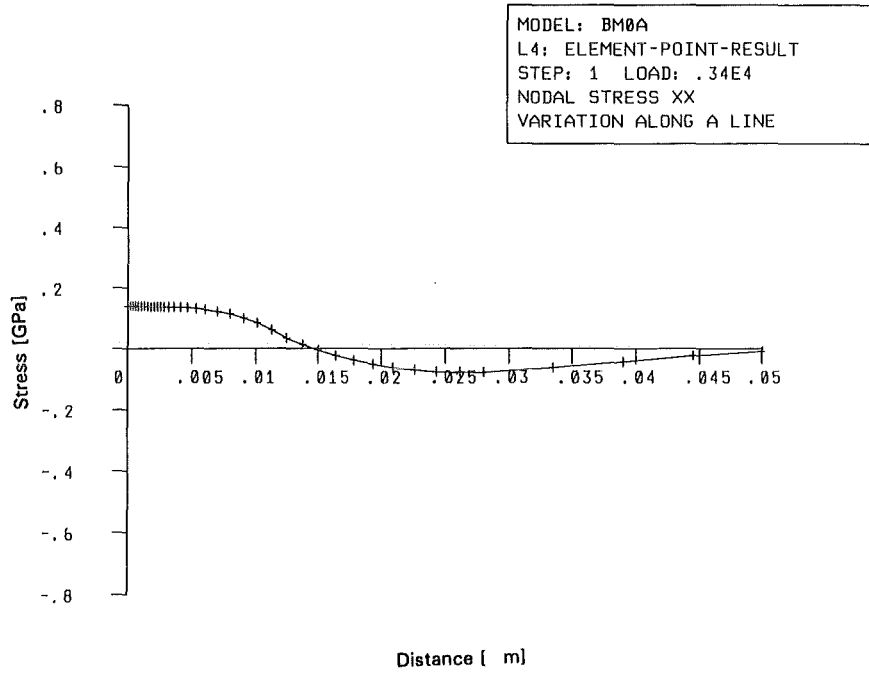


Fig. B-12 Transverse residual stresses ( $\sigma_{xx}$ ) in austenitic plate (middle plane)

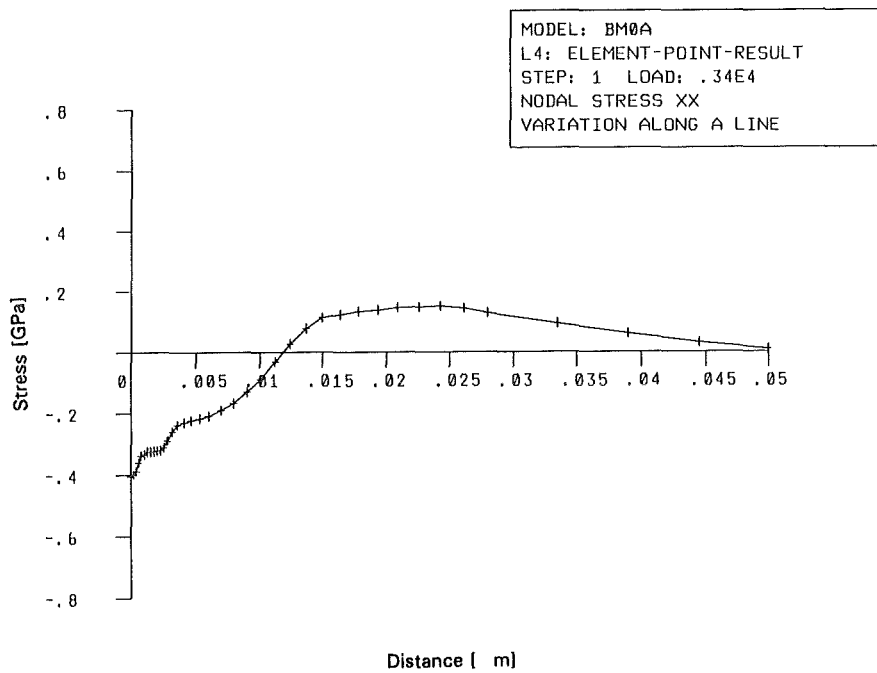


Fig. B-13 Transverse residual stresses ( $\sigma_{xx}$ ) in austenitic plate (surface)

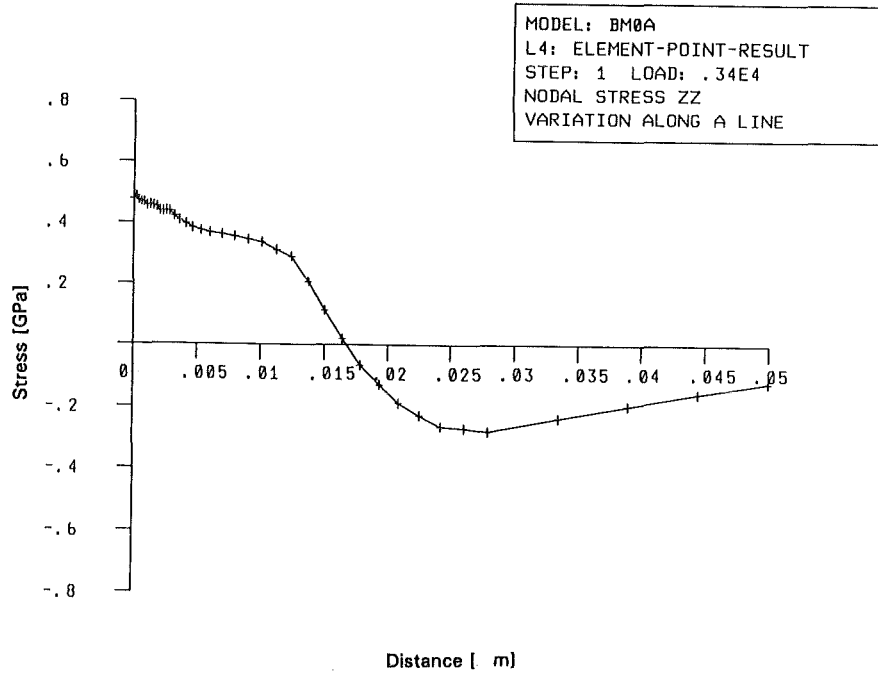


Fig. B-14 Longitudinal residual stresses ( $\sigma_{zz}$ ) in austenitic plate (middle plane)

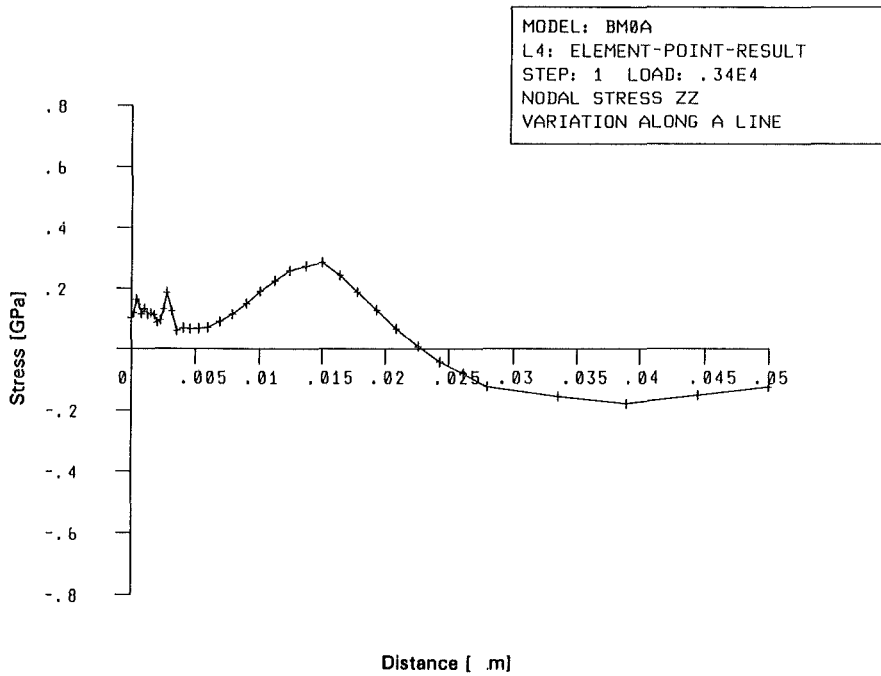
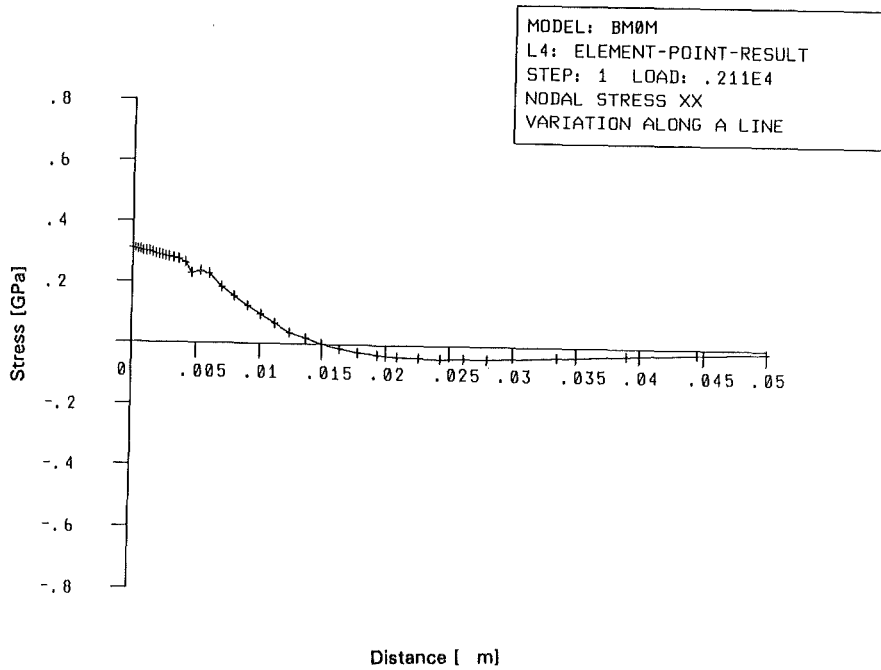
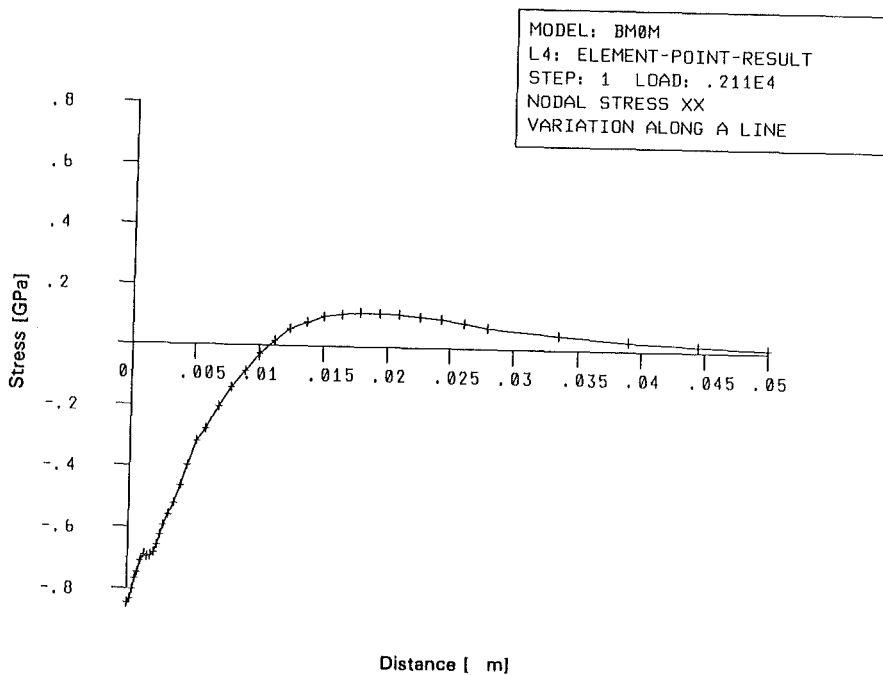


Fig. B-15 Longitudinal residual stresses ( $\sigma_{zz}$ ) in austenitic plate (surface)



**Fig. B-16** Transverse residual stresses ( $\sigma_{xx}$ ) in martensitic plate (middle plane, without phase transformations)



**Fig. B-17** Transverse residual stresses ( $\sigma_{xx}$ ) in martensitic plate (surface, without phase transformations)

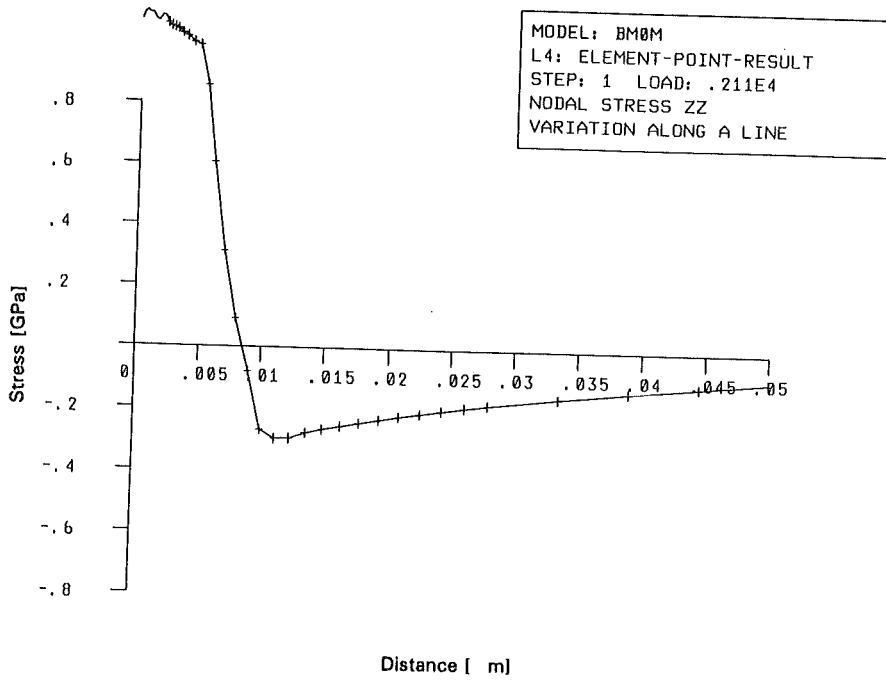


**Fig. B-18** Longitudinal residual stresses ( $\sigma_{zz}$ ) in martensitic plate (middle plane, without phase transformations)

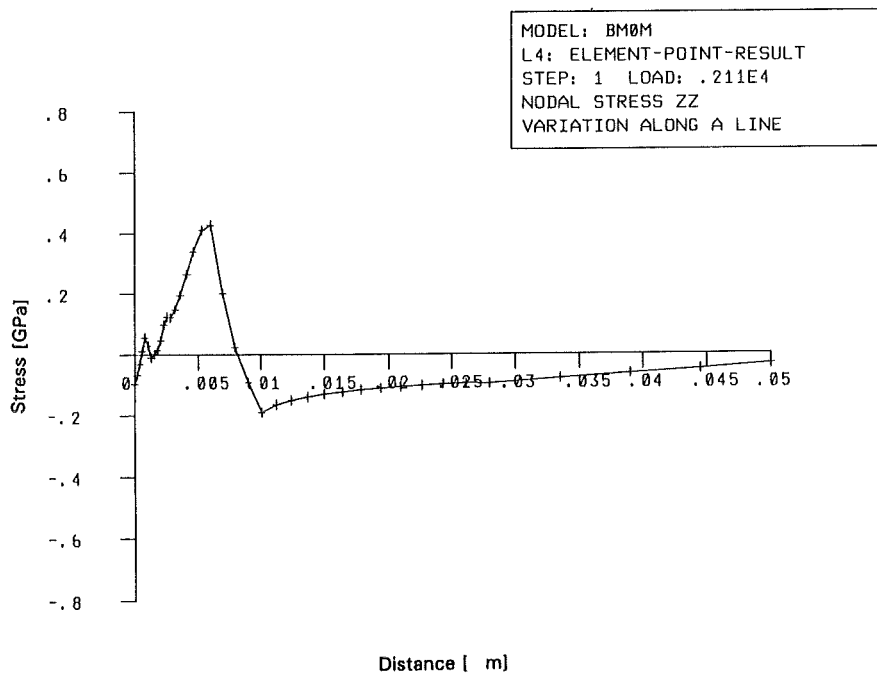


**Fig. B-19** Longitudinal residual stresses ( $\sigma_{zz}$ ) in martensitic plate (surface, without phase transformations)

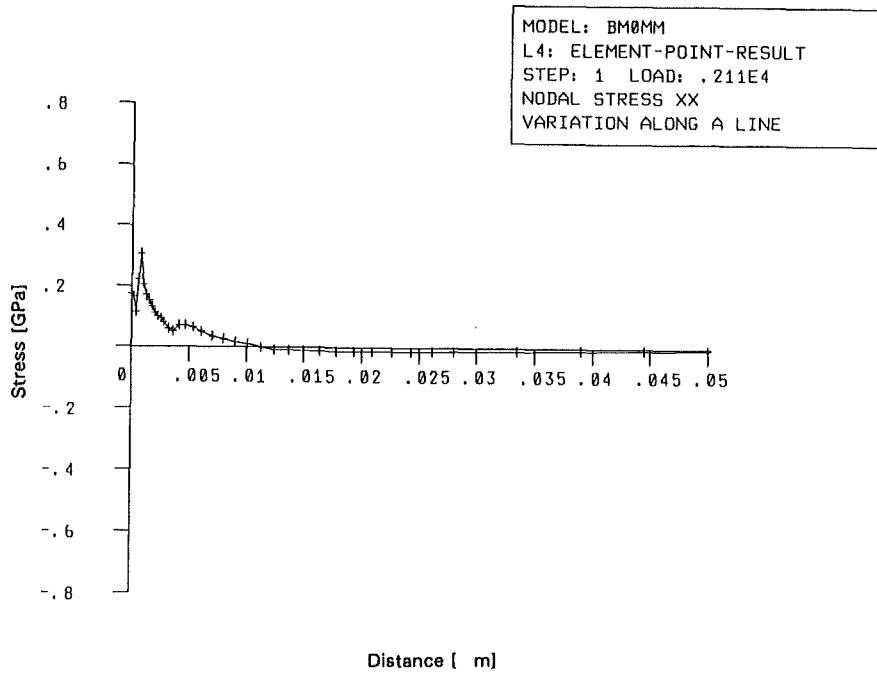


**Fig. B-20** Transverse residual stresses ( $\sigma_{xx}$ ) in martensitic plate (middle plane, with phase transformations)

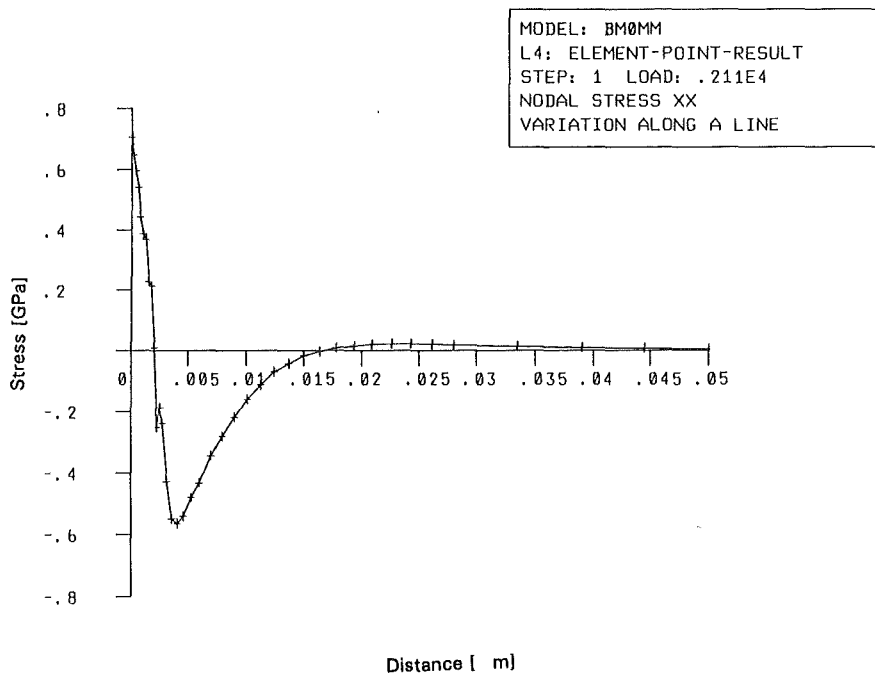


**Fig. B-21** Transverse residual stresses ( $\sigma_{xx}$ ) in martensitic plate (surface, with phase transformations)

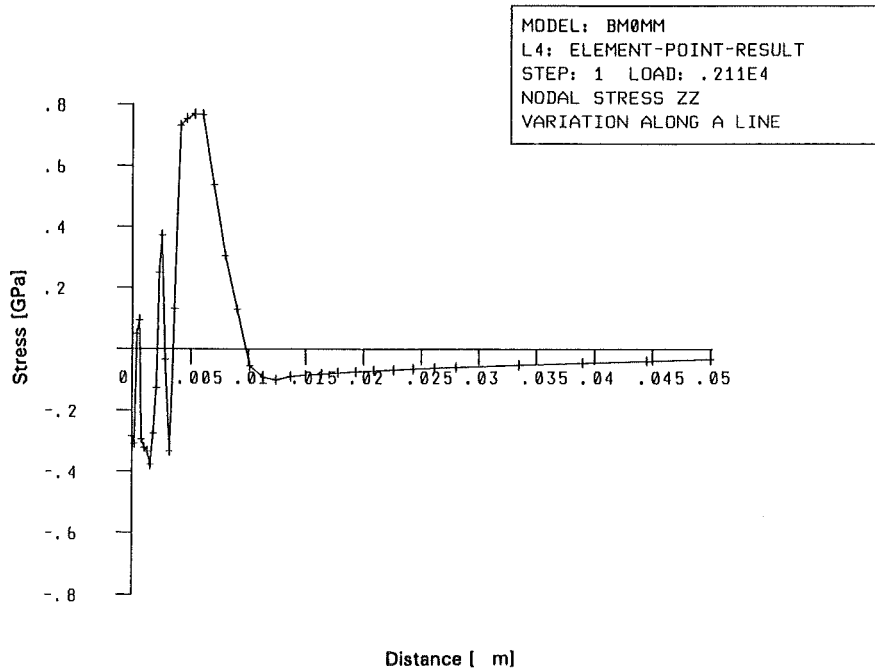


**Fig. B-22** Longitudinal residual stresses ( $\sigma_{zz}$ ) in martensitic plate (middle plane, with phase transformations)

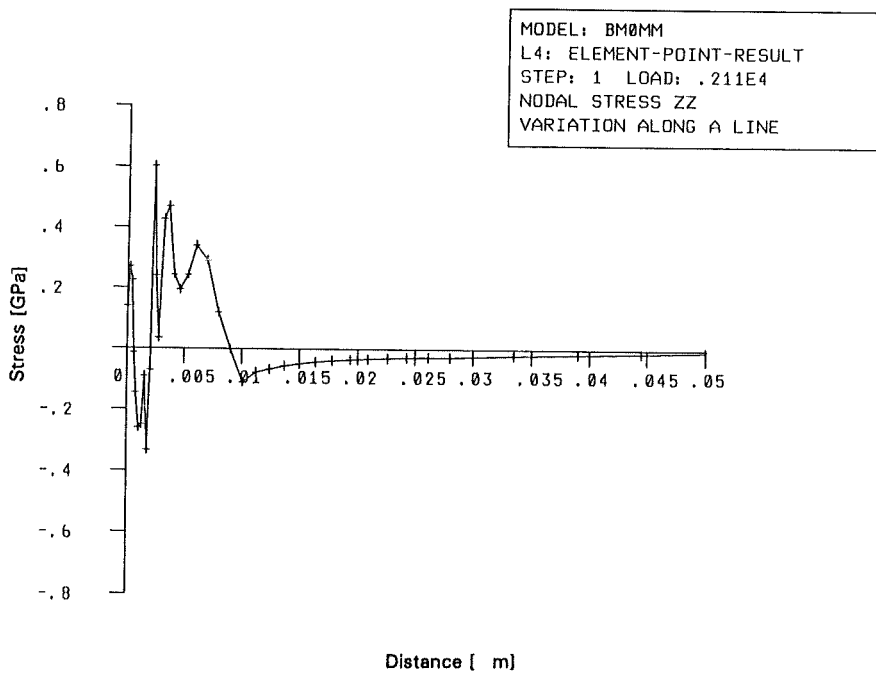


**Fig. B-23** Longitudinal residual stresses ( $\sigma_{zz}$ ) in martensitic plate (surface, with phase transformations)

#### **B.4.2 Effects of heat treatment**

The effects of heat treatment comply with findings reported in Sec. 3.7 for both materials analyzed and does not seem to depend on geometry.